Laser-tip interactions in the laser-assisted atom probe tomography technique: the case of III-V semiconductors

Auteur : Hanus, Romain
Promoteur(s) : Vanderheyden, Benoit
Faculté : Faculté des Sciences appliquées
Diplôme : Master en ingénieur civil physicien, à finalité approfondie
Année académique : 2017-2018
URI/URL : http://hdl.handle.net/2268.2/5523

University of Liege

Master Thesis

Laser-tip interactions in the laser-assisted atom probe tomography technique: the case of III-V semiconductors

Authors:
Romain Hanus

Advisors:
Benoît VANDERHEYDEN
Janusz BOGDANOWICZ

Academic Year: 2017-2018

Acknowledgements

I would like to sincerely thank my supervisor from *Imec*, Janusz Bogdanowicz, whose continuous help, support and patience during this project have kept me on the right track. I have learned a lot from him as a person and I will always remember: "Focus! And keep it simple!".

I would like to thank you Ramya Cuduvally, who was always there to provides some unexpected experimental results.

I would also like to sincerely thank Benoit Vanderheyden, my promoter at the University of Liege, for his precious advice throughout this work and for its support and its guidance.

Contents

Chapter 1

Introduction

The recent innovation in the MosFET industry has seen the use of new III-V semiconductor materials such as InGaAs due to the limitation of silicon and the down-scaling of transistors. The novelty of these materials in transistors, associated with the nanometric scale of the devices, has opened new problems such as the reliability and performance of the device. Information of the internal structure is then highly important.

The atom probe tomography (APT) is an atomic-resolution microscopy technique, which provides a unique insight into the atomic structures and chemical compounds of small volume materials.

1.1 III-V semiconductors FinFET

For the past 50 years, silicon has been the premier choice for electronics material especially MOSFET because of its material properties (SiO_2, Si/SiO_2 interface), cheapness and the constant improvement in performance that could have been made. But with the continuous down-scaling of electronics devices (Moore's law), the power dissipated by unit area is further increased and silicon does not meet the requirements imposed by the down-scaling. One solution to reduce the dissipated power is to use alternative channel materials with a higher intrinsic carrier mobility for which an increase in drive current is expected and lower voltages could potentially be used. Promising material are the family of III-V semiconductors particularly GaAs, AlAs, InAs, InP and their ternary and Quaternary alloys such as $Ga_xIn_{1-x}As$, which has an electron mobility 10 times higher than that of silicon as shown in Figure 1.1. They also exhibit out-standing frequency responses.

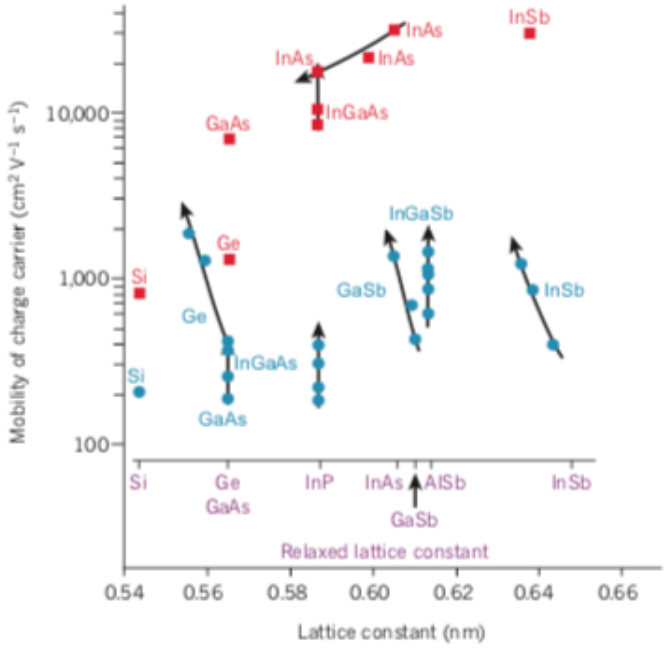

Figure 1.1: Electron and hole mobility of group III–V compound semiconductors at room temperature. Electrons mobility (red) and holes mobility (blue). Reproduced from [16]

Parallelly, the traditional planar complementary metal-oxide- semiconductor (CMOS) transistor is being progressively replaced by a 3D fin geometry (FinFet) (Figure 1.2), where the gate wrap the channel on 3 side, providing much greater electrostatic control over the carriers within it. *Imec* was the world's first lab center to demonstrate a III-V FinFET device monolithically integrated on a 300mm silicon wafer in November 2013. This breakthrough makes it possible to continue the down-scaling the CMOS down to 7nm. But many challenges are still to be faced. Working with 3D heterogeneous sub-nanometric material requires a good comprehension of the internal structure to ensure performance and reliability of the future devices, which cannot be done by conventional microscopy technique such as Scanning electron microscope (SEM) giving information about the surface geometry of the device.

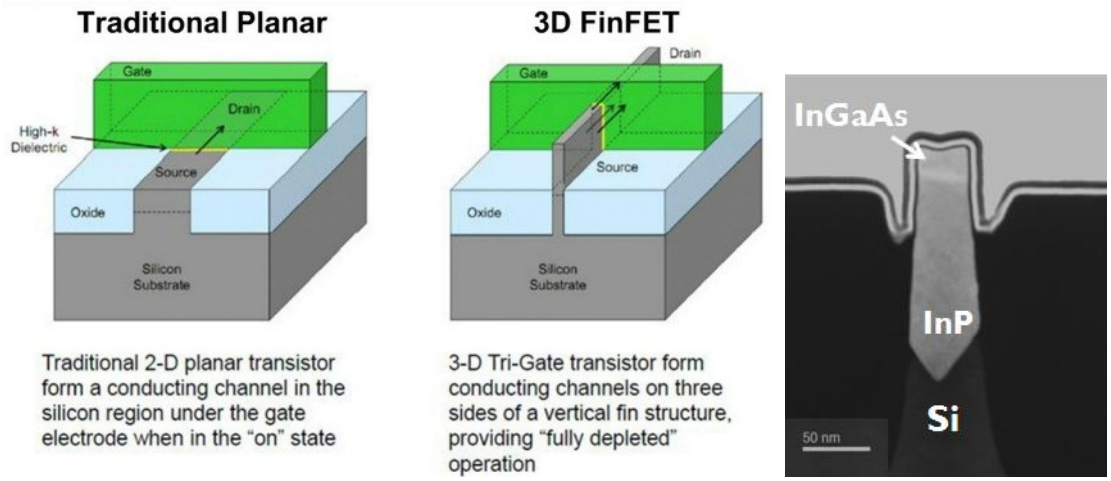

(a) (b)

Figure 1.2: (a) Comparison of 2D and 3D transistor geometry. (b) Cross section of an actual FinFet transistor with an InGaAs channel.

1.2 Atom probe tomography

Atom probe tomography (APT) is an atomic-resolution microscopy technique, which provides unique insight into the atomic positions and chemical composition of small volume materials. The technique is based on the emission of ionized species from a needle shaped specimen (apex radius ∼100nm) (Figure 1.3a) by a process called field evaporation. The surface of the sample is subjected to a high DC electric field (Figure 1.3b) which modifies the potential barrier of the surface atom, thereby enabling its ionization and subsequent evaporation. The emitted ions follow well-defined trajectories based on the electric field lines and can be detected by a position-sensitive detector at a given macroscopic distance from the tip, resulting in a magnified projected image of the tip surface with almost atomic spatial resolution (∼0.2-0.3nm).

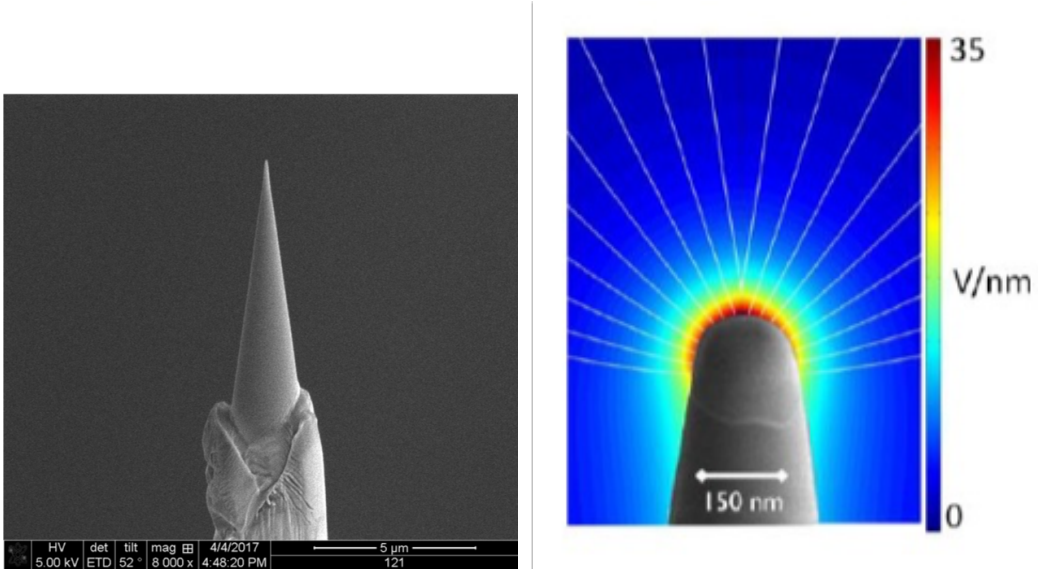

(a) (b)

Figure 1.3: (a) SEM image of an InGaAs tip used in APT from *Imec*. (b) Intensity of the electric field generated by a typical sharp needle shaped specimen under a DC voltage. Electric field lines are represented as well.

In actual atom probe, field evaporation is triggered by a combination of a DC electric field and voltage pulses or focused laser pulses. The time of flight of ions can then be computed as the time between the emission of the pulse and the detection of the ions, allowing the determination of the ions' chemical species by mass spectroscopy (Figure 1.4a). By evaporating layer by layer, the sample can be reconstructed back thus allowing a full 3-dimensional characterization of the sample as shown with some example in Figure 1.4b. Since APT has the potential to provide localized information at the sub-nm scale, it finds diverse applications in the semiconductors industry such as extraction of composition, doping levels, layer thicknesses, dopant distribution.

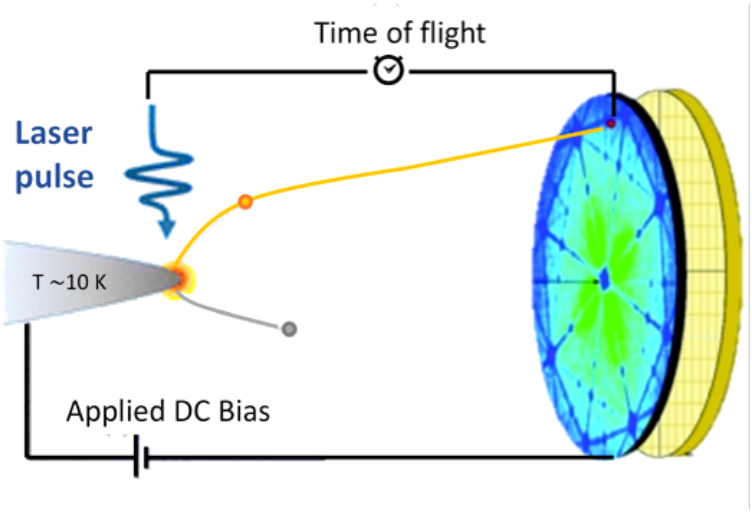

(a)

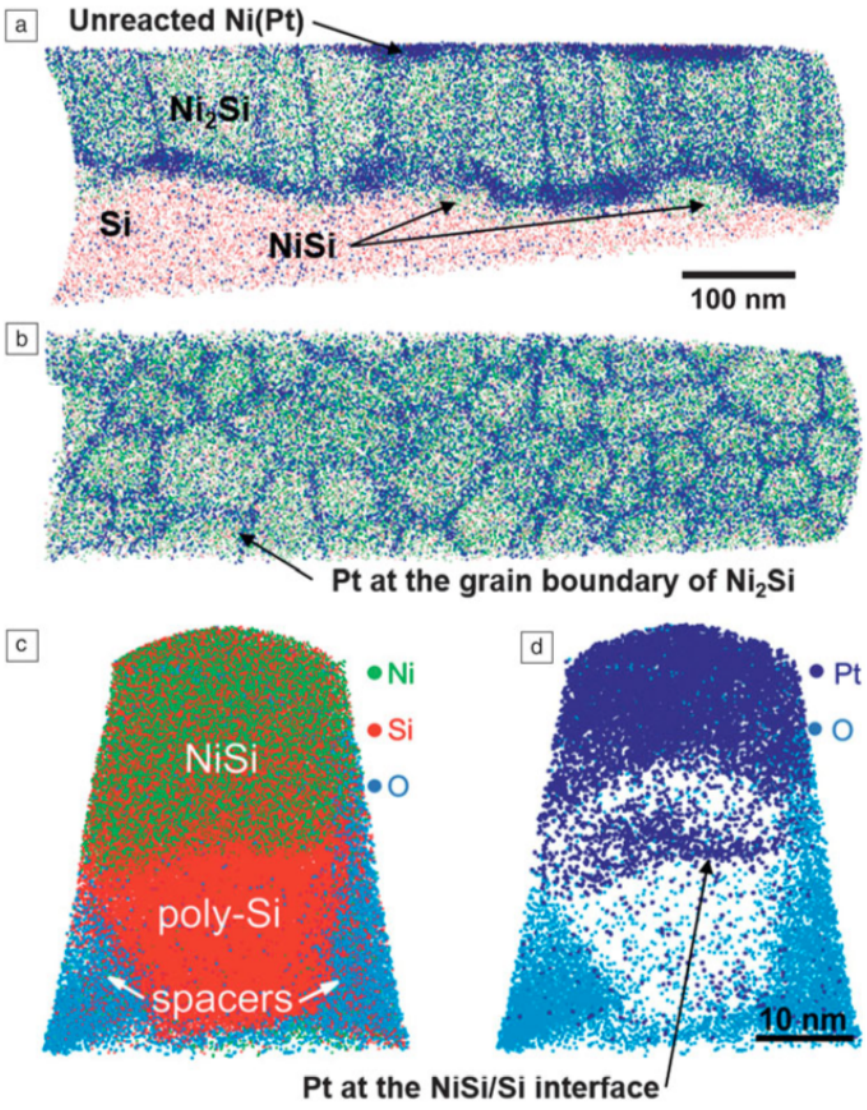

(b)

Figure 1.4: (a) Schematic representation of the atom probe principle. A laser pulse triggers the emission of ion which are then detected. (b) 3D reconstruction of different tips using atom probe. Reproduces from [17]

From the pulse laser interaction with the sample to the mass spectra, the underlying mechanisms involved in Laser atom probe are numerous and complex. La-ATP has been extensively studied on non-metallic tip such as silicon tip and simple to complex models have often been able to explain the different observations made on silicon tip. The recent use of InGaAs for electronic material leads to new questions to answer. The different optical and thermal InGaAs properties, as compared to those of silicon are expected to influence the experimental data. How does the optical properties of InGas influence the interaction between the laser and the sample? It has already been shown that the laser interaction can be viewed as thermal pulse for the sample and that evaporation of an ion can be explained by a thermal activation for the silicon [6], but how accurately does the analytical model match the experimental data for InGaAs?

In this thesis, the objectives are to try to understand the optical interaction between an InGaAs tip and the laser beam to explain the experimental data, and understand the time of flight spectra with an analytic model. A better understanding of InGaAs atom probe should help the interpretation of the output data and improve the accuracy of the atom probe technique.

Outline

In the second chapter, the working principles of laser atom probe will be explained, such as field evaporation. Laser interaction with a semiconductor and mass spectroscopy as well as hit maps will also be explained.

In the third chapter, experimental results obtained for silicon tips and for InGaAs tips with the laser assisted atom probe technique are compared.

In the fourth chapter, light interaction with InGaAs conical tip is analysed using numerical tools and the link with experimental results is made. Models are proposed to explain the numerical results.

In the fifth chapter, the temperature evolution of the tip apex is evaluated based on thermal model developed for silicon tips. Finally, the last chapter conclude on the progress made in the understanding with InGaAs of laser assisted atom probe and the remaining unsolved problems.

Chapter 2

LA-Atom probe: Working principles

The successive steps involved in laser assisted atom probe experiment are presented in Figure 2.1.

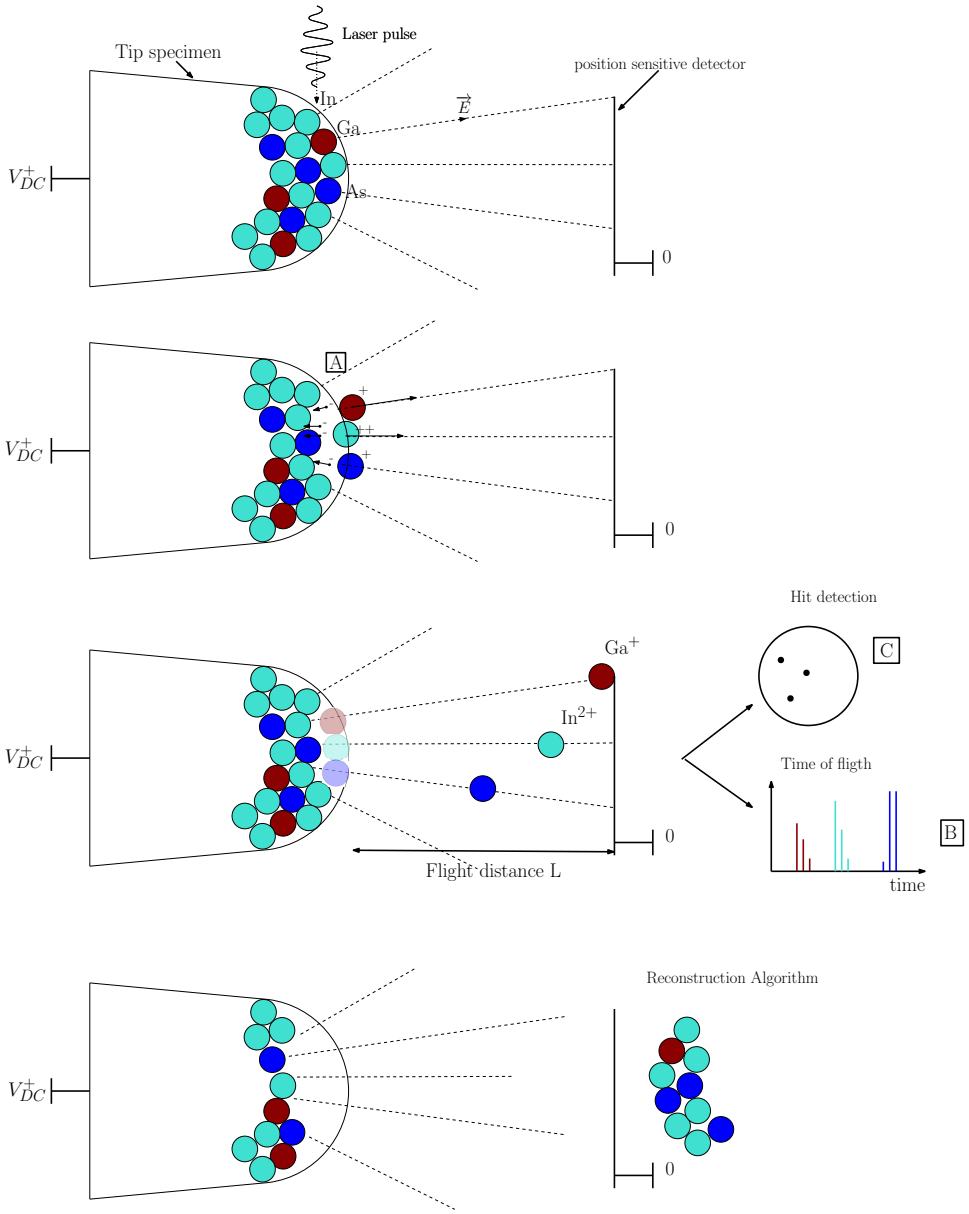

Figure 2.1: Successive step involved in laser atom probe. A pulse laser shines the tip under a electric field, inducing field evaporation. The emitted ions are detected and their time of flight recorded. The tip's internal structure can then be reconstructed back.

In this chapter, we first describe the physics principle of field evaporation and laser pulse field evaporation (Step A in Figure 2.1), and the way laser pulse can be used to induce field evaporation. We then briefly talk about mass spectra (step B) and the link between the cooling time and the time of flight mass spectra. Finally, hit detection is discussed (step C).

2.1 Field evaporation

Field evaporation is the field-induced removal of a surface atom, whereby it is ionized and then accelerated away from the surface of the material following trajectories defined by the electric field lines. This evaporation process follows immediately after the ionization. The electric field causes the polarization of the surface atom which can be repelled from the surface while one of its electrons is drained into the surface (ionization). Even though the mechanisms of this process are not exactly understood, simple models using thermodynamic considerations have often been used.

In the absence of an electric field, in order for an atom to be removed from the surface, it has to overcome a potential barrier as shown in Figure 2.2b. Since field evaporation involves the formation of an ion, energy has to be provided to the atom for ionization. Considering both these constraints, the potential barrier for an atom to be field evaporated is Q_o as shown in Figure 2.2c.

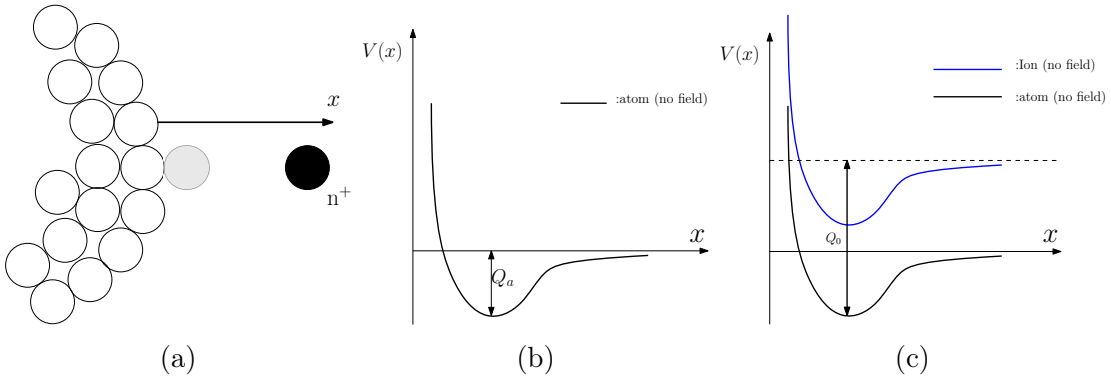

Figure 2.2: (a) Ionized atom (black) leaving the surface (grey). (b) Potential curve of a bounded atom with no applied field. (c) Potential curve of a bounded atom ion (green) with no applied field. Q_o is the potential barrier to have a free ion.

When an electric field is applied, the ionic potential curve is modified as shown in Figure 2.3. However, the transition from atom to ion is not clear and the exact mechanism of departure and the nature of the particle that leaves the surface is still a subject of debates. Some models have been proposed [12] and are summarized below.

Müller [33] proposed that the atom becomes fully ionized at a critical distance from the surface before leaving it. Thus, the process is viewed as the thermal activation of an ion. Gomer [21] on the other hand proposed that the atom is progressively ionized while escaping the surface in a mechanism called *charge draining*. This model views field evaporation as a continuous process on a same ground state with a potential barrier $Q(E)$ as shown in Figure 2.3. In this situation, an atom bound to the surface can be field-evaporated if the thermal agitation is sufficient enough to overcome the potential barrier $Q(E)$ rather than Q_o. Tunneling of ions is also possible if the potential curve is strongly modified by the electric field. It should be clear that these are only models, the distinction between ions and atoms being not perfectly strict since the atoms are highly polarized in the intense electric field.

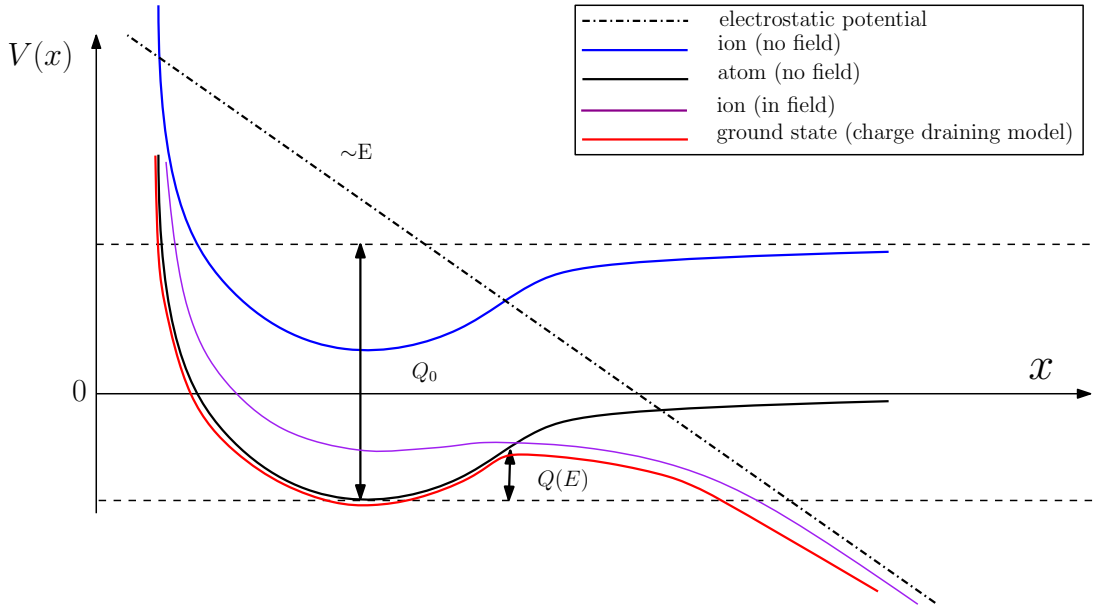

Figure 2.3: Schematic representation of field evaporation showing the potential well and barrier. In the *charge draining* model, a unique ground state (red curve) with potential barrier $Q(F)$ represents the transition from atom to ion.

For electric fields close to the evaporation field E_{evap}(the electric field at which the barrier $Q(E)$ becomes zero), one has the following approximation [12] for the field-dependent barrier height

$$Q(E) \simeq Q_o \left(1 - \frac{E}{E_{evap}}\right). \tag{2.1}$$

2.1.1 Evaporation probability

In order for an atom to be field evaporated, it needs to cross a potential barrier. It is usually assumed that this is a thermally assisted process. The probability for an atom to escape from the surface is then given by the Maxwell-Boltzmann distribution,

$$P_{evap} \propto \exp\left(\frac{-Q(E)}{k_b T}\right), \tag{2.2}$$

where k_b is the Boltzmann constant, $Q(E)$ is the field-dependent barrier height and T the absolute temperature.

2.1.2 Generation of the Electrostatic Field

Since the atom probe technique relies on field evaporation, a strong electric field must be generated at the surface of the sample. This is achieved thanks to a very sharp needle shape of the sample and a high positive voltage. As it will be explained later, the preparation of such a specimen is often approximated by a truncated cone with a hemispherical cap as shown in Figure 2.4. The electric field E, generated at the apex of the cone can be approximated based on the expression for a charged sphere. Taking into account the deviation of the cone from a sphere, this gives

$$E = \frac{V}{k_f R}, \tag{2.3}$$

where R is the curvature radius , V the applied voltage and k_f is the *field factor*, that accounts for the tip shape and its electrostatic environment [12]. Its values are in between 2 and 8. For

example, in the case of a smaller shank angle, the electric field line density is higher at the tip apex and k_f is then lower. The field factor is also reduced if the counter-electrode is closer to the tip apex, because the electric field line density will also be higher as shown in [38].

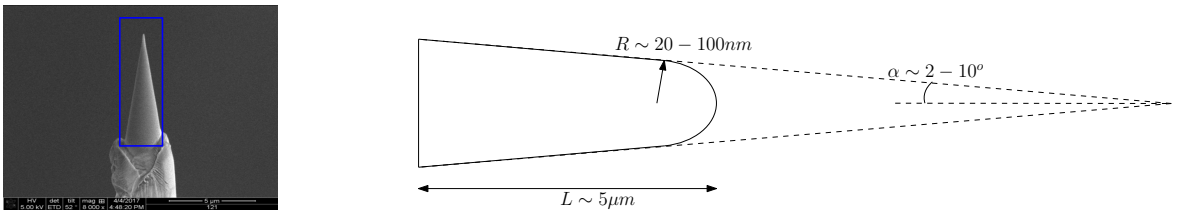

Figure 2.4: The sample tip used in the atom probe is represented by a cone with an hemispherical cap. L is the length of the cone, R the curvature radius of the apex and α is the shank angle.

2.1.3 Pulsed Field Evaporation

The relation (2.2) shows that there are two mechanisms that can trigger the field evaporation. Either the barrier $Q(E)$ is lowered (field effect) or either the thermal agitation (thermal effect) is increased with a larger temperature T. When an atom is vibrating at the surface, it will test the barrier at each oscillation. It can then be understood that the evaporation rate or evaporation flux is proportional to both the frequency of vibration ν_o and the probability of evaporation,

$$\phi_{evap} = \nu_o \exp\left(\frac{-Q(E)}{k_b T}\right) = \nu_o \exp\left(\frac{-Q_o\left(1 - E/E_{evap}\right)}{k_b T}\right), \tag{2.4}$$

which is an Arrhenius law.

When a constant evaporation flux is considered, eq. (2.4) leads to a linear relation between the temperature and the field.This gives a convenient way of interpreting the thermal and field effect as seen in Figure 2.5. Field evaporation can be controlled either by increasing the electric field at a constant temperature or by varying temperature at constant DC field. If we consider a situation where the sample is under a constant DC field and constant base temperature, voltages or thermal pulses can be used to induce field evaporation.

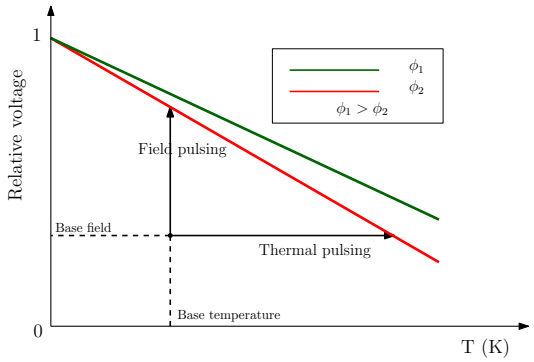

Figure 2.5: Constant flux line in a Voltage-Temperature plane and the 2 possibilities to control field evaporation.

HV-pulsing

In this type of pulsed field evaporation, fast voltage pulses of a few nanoseconds are used to produce field evaporation. The pulse V_p superimposes with the DC voltage V_{DC}, which lowers the barrier and triggers the emission of ions during the time of the pulse. These ions are then accelerated by the combination of the DC field and pulse field.

However, HV-pulsing can only be used for materials with good electrical conductivities. This pulse cannot be transmitted properly, as a result of the low pass-filter effect of poorly conductive material. Voltage pulses have a rise time in the range of the nanosecond, and it is generally found that these signals cannot be transmitted for resistivity in the above 10–10^2 Ωcm [9]. This limits the use of HV-pulsing to materials with good electrical conductivity.

Laser-pulsing

In this method, the sample is subject to a DC field at a constant base temperature and a laser pulse is used to field evaporate the atom at the apex. This allows one to overcome the limitations associated with HV-pulsing and nonmetallic materials such as semiconductor can be used. Furthermore, shorter laser pulse (down to femto-second) than HV-pulse (down to the nano-second) can be used, which increases mass resolution because it reduces the time windows for field evaporation. Another drawback associated with the HV-pulsing is the electrostatic pressure linked to the high field involved. This is not the case with laser pulsing atom probe, because the DC field used is lower than the one in HV-pulsing atom probe.

The physical mechanisms that lead to field evaporation with laser-pulse atom probe has been a subject of debate since it has first been used by Tsong and Kellogg [29]. It can be understood that many processes between the interaction of an electromagnetic wave and a sample tip smaller than the wavelength will be involved. For example, field evaporation might be a combination of thermal and field pulsing as shown in Figure 2.6, simply because a electromagnetic wave carries both energy that could heat up the sample and an intrinsic electric field.

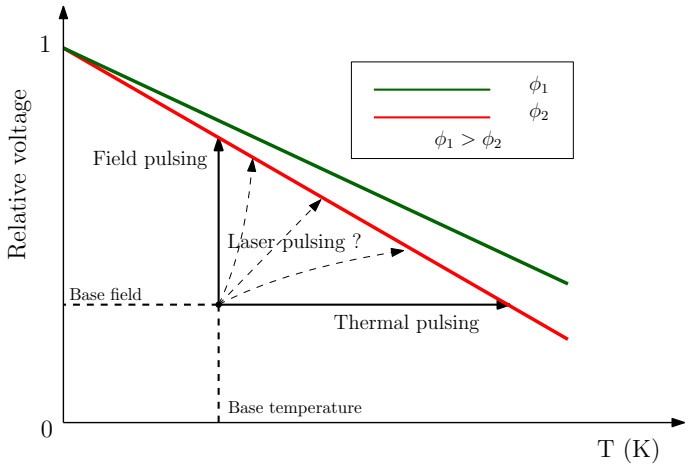

Figure 2.6: Different possible influences of the laser pulse.

To try to understand what triggers evaporation when using a laser pulse, we can consider the different effects, thermal and athermal, that could exist. It should be noted that in the case of an athermal process, evaporation is induced by the pulse energy without any change in the specimen temperature. This increase in evaporation rate should only occur during the laser pulse by definition. As discussed by Kelly et al. [40], for very short pulse (<10 ps), if laser pulses trigger evaporation athermally, then the mass resolution power should be very high.With today best atom probe instrumentation, the timing resolution is about 80 ps, the peak would then

appear as Gaussian in shape with a width of about 80ps. However, the width of most peaks is closer to 200 to 500 ps. As remarked by Kelly et al., it is then difficult to demonstrate that field evaporation is triggered by an athermal process. Some authors have proposed different possible mechanisms that could lead to an athermal field evaporation as discussed below.

It can be shown that the intrinsic electric field for short laser pulses (e.g femto second pulses) is of the order of a few 10 V/nm, which is the order of magnitude required for field evaporation in the atom probe tomography Provided that some *field enhancement* [11] is possible at the tip apex, the intrinsic electric field of the laser could possibly trigger field evaporation. However, this mechanism has been ruled out by the fact that the oscillation of the enhanced electric field is too fast compared to the oscillation of the atoms at the surface of the apex [14][12]. The potential barrier is raised and lowered at the frequency of the laser, too fast for an atom to field evaporate.

For a pulse laser (IR) of maximal 22000μW (highest power use in this thesis) with a duration pulse of 500 fs, a repetition of 100kHz and a spot size of about 20μm, the resulting maximal peak Intensity is roughly 350 TW/m^2(see Appendix B). Working at high laser intensity, non-linear effects are enhanced. A model based on optical rectification was proposed by A. Vella et al. [5]. Optical rectification is a non-linear effect where a DC-electric field is generated at the surface during the laser pulse. This DC electric field can possibly lower the potential barrier and atoms can field evaporate. However, the emission of ions has been shown to occur over period much larger than the period of the laser pulse [27].

As explained by Kelly et al.[40], photoionization should not happen for metals. Indeed, for metals, the lifetime of an ion on the surface is about 30 fs, which, even under 10V/nm, represents only a movement of about 0.0001 nm.

From the previous remarks, it can be concluded that the field evaporation with laser pulsing is mainly due to a thermal pulse. The energy of the laser pulse is absorbed and converted into heat that raises the temperature of the tip apex, which increases the probability of escaping by an atom from the surface by virtue of (2.2). The successive increase and decrease in temperature is viewed as thermal pulsing.

2.1.4 Laser absorption and heating mechanisms

As explained before, laser induce field evaporation by thermal pulses. The mechanisms in which energy is deposit on the specimen is discussed in the following section. The apex temperature evolution plays an important role in laser assisted atom probe with semiconductor, as it directly influences the field evaporation. Even though it will be explained in the next section of this chapter, one can still understand that a slow rising of the apex temperature can create delayed evaporation of the atoms, thus directly impacting the mass spectrum resolution. It is then important to know how energy is absorbed and how temperature evolves.

For metals, most of the energy is absorbed over a distance known as the skin depth. The incoming electromagnetic wave accelerates the electrons and create surface currents. This "hot" electrons then rapidly thermalize with the nuclei, transferring their energy to them and creating phonons (heat) over time scale on the order of 0.5 to 10 ps (fast dynamic of electrons). The tip apex region of the specimen is locally warmer and maximal temperature is reached after thermalization. Heat will then flow by conduction toward the tip base and specimen cools down on the order of nanosecond. Most of the energy can be considered as absorbed near the surface and instantaneously heating the sample to give it an initial temperature.

For semiconductors, the absorption is expected to be more complex than for metals. An incident electromagnetic wave will penetrate inside the material and depending on the band structure of semiconductors, different phenomena occur, such as free carriers' excitation and relaxation across the band gap, scattering and recombination of the carriers, which transfer their energy to the lattice by phonon coupling and carrier recombination, with different time scale. It is then important to consider the different time scale of these phenomena as it could influence the temperature evolution. The different phenomena and associated time scale are shown in Figure 2.7 and 2.8 respectively for a direct band gap material as for InGaAs. The following discussion is, however, still valid for indirect band gap material such as silicon.

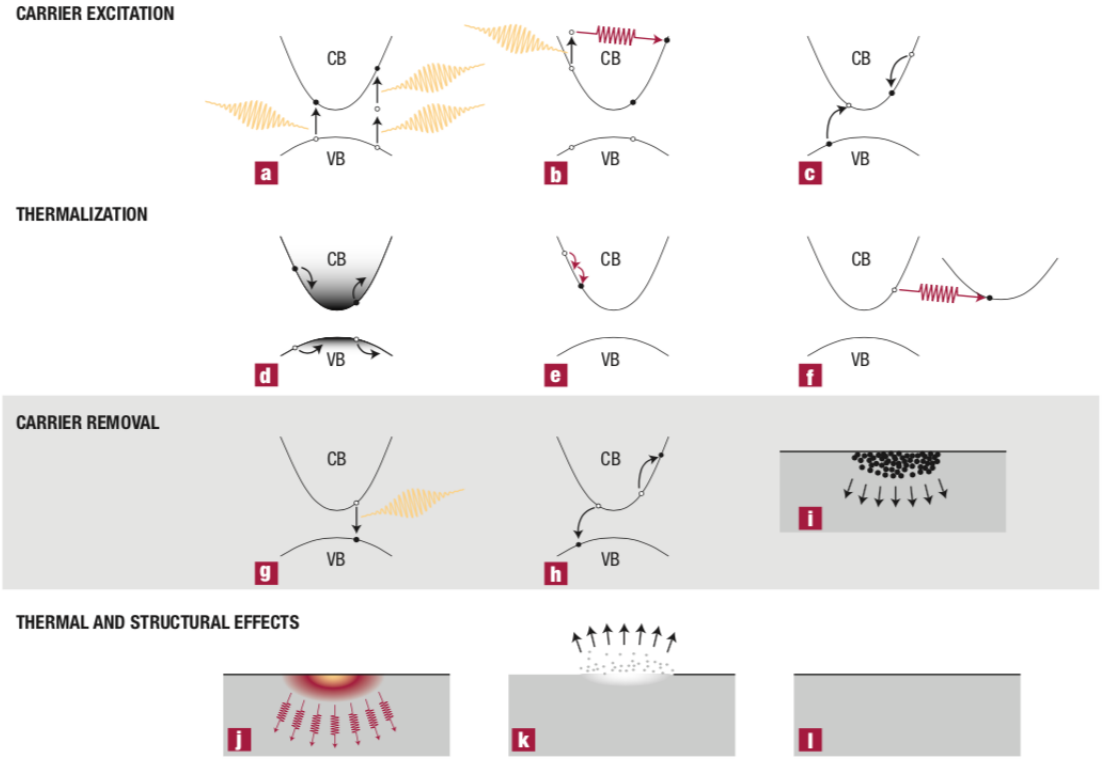

Figure 2.7: Excitation of carrier and lattice by a laser in a direct band gap material. CB is the conduction band and VB the valence band. **a**, Multiphoton absorption. **b**, Free-carrier absorption. **c**, Impact ionization. **d**, Carrier distribution before scattering. **e**, Carrier–carrier scattering. **f**, Carrier–phonon scattering. **g**, Radiative recombination. **h**, Auger recombination. **i**, Diffusion of excited carriers. **j**, Thermal diffusion. **k**, Ablation. **l**, Resolidification or condensation. Figure reproduced from [39].

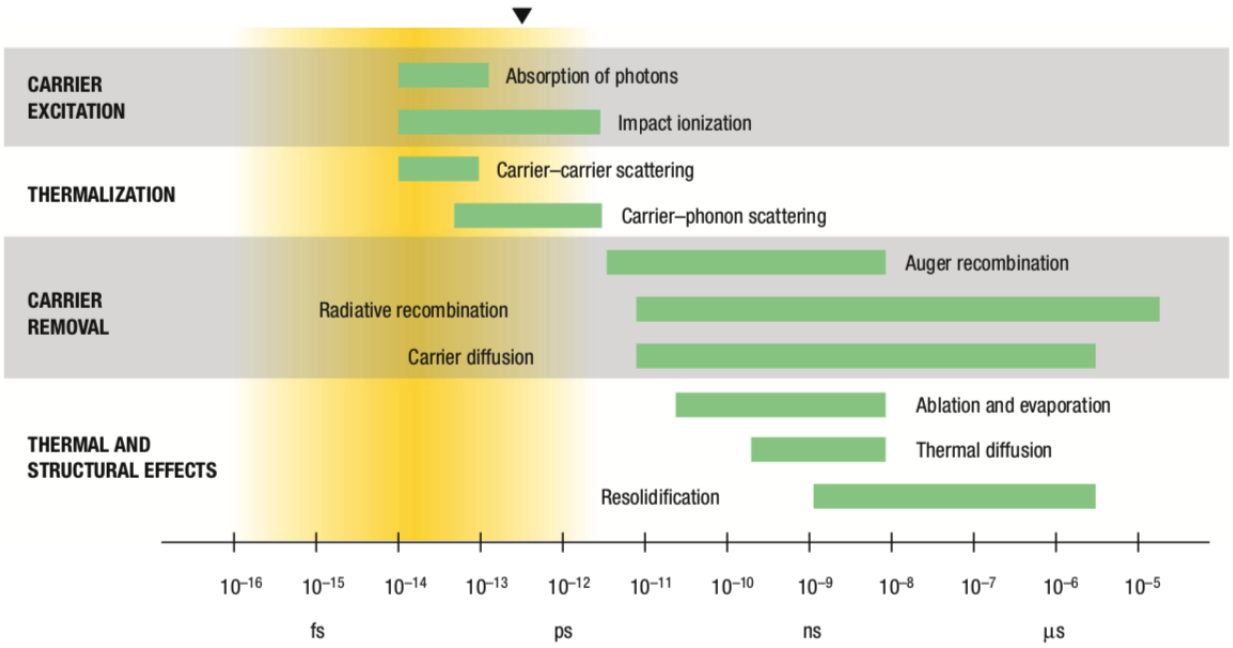

Figure 2.8: Approximation range (green bars) of the different time scales of the different processes in a direct band gap material excited by a laser. The black triangle represents the maximal time scale of the actual laser used in this thesis (∼500fs). Figure reproduced from [39].

As shown in Figure 2.8, four different regimes can be distinguished depending on their time scale:

- Carrier excitation: If one considers that initially at cryogenic temperature all carriers occupy the valence band, at soon as the laser reaches the surface, when the photon energy of the laser is larger than the band gap energy, free carriers are generated either by single photon absorption for direct band gap materials (fig. 2.7a left) or by photon assistance to conserve momentum (fig. 2.7a right) for indirect band gap materials. These free carriers can increase their energy by free carrier absorption (fig. 2.7b) during the time of the pulse.

- Thermalization: After excitation, electrons and holes are redistributed by scattering in the conduction and valence band within few hundreds of femtoseconds (fig. 2.7d). Energy is transferred to the lattice by carrier-phonon scattering (fig. 2.7e and fig. 2.7f), which heats the specimen. Concurrently, free carriers' excitation weakens as the valence band is progressively depleted. Because the emitted phonons carry little energy, many scattering processes are required before thermal equilibrium is reached between the carriers and the lattice, which is made after a few picosecond.

- Thermal effect and carrier removal: From 10^{-11} to 10^{-8}, the excess carriers are removed either by diffusion in the material or recombination of electrons and holes across the gap. Recombination decreases the carrier density and can be either radiative (fig. 2.7g) or non-radiative (fig. 2.7h). Heat is progressively transferred to the lattice with this process, but only a long time relatively after the initial equilibrium temperature was reached with thermalization. Thus, depending on the time scale of the thermal diffusion process, recombination process and diffusion models of the carriers might need to be considered with the thermal diffusion model.

It must also be noted that the nanometric shape of the sample will also influence the laser absorption. For semiconductors, the intensity of an incident electromagnetic wave with photon energy above the band gap energy will follow an exponential decrease (Beer–Lambert law) over a characteristic distance $\delta_{penetration}$, which depends on the semiconductors. The characteristic distance can be as small as a few nanometer (e.g. $\delta_{penetration}$=41nm for InGaAs with green light), which is considered as surface absorption for macroscopic bulk semiconductor, but not in the case of nano-scale sample. Thus, depending on the semiconductor, light can penetrate inside the tip's volume before its intensity has significantly decreased.

If light can penetrate into the volume, because of the comparable size of the tip (radius∼50-150 nm) with respect to the wavelength used (green∼515nm), light coupling is possible, created by interference due to reflection inside the tip. Apparition of maximum and minimum of absorption is thus expected. The laser interaction with nanometric tip will be described in much more details in Chapter 4 with the study of the absorption map and will not thus discussed more in this section.

From the previous note, if light is not absorbed uniformly near the apex, the temperature profile of the apex will be directly impacted, as well as the excess carriers distribution and the temperature evolution of the apex will be different than in the case of a uniform absorption close to the apex. Consequently, the absorption map is the first step in understanding the temperature evolution of the tip.

2.2 Mass spectra

After describing the main aspects of field evaporation and in which ways a laser pulse can induce field evaporation, we discuss about time of flight mass spectroscopy and the relation between the temperature and the time of flight spectra.

2.2.1 Time of flight mass spectroscopy

Pulse field evaporation allows the possibility of using mass spectroscopy. The time of flight t_{flight} of the ion in the atom probe tomography is defined as the time between the departure of the pulse and the detection of the ion. It can be computed through the kinetic energy. As the ion starts to be accelerated away from the tip surface, the electric field gives the ion a potential energy $E_p = neV$, where n is the charge of the ion, V the applied voltage and e the elementary charge. This potential energy is progressively converted into kinetic energy $E_k = \frac{1}{2}mv^2$, where m is the mass of the atomic charge and v (assuming there is no initial velocity when the ion leaves the surface). As the final velocity of the ion is reached within the first few radii of the flight, the velocity v is then $v \simeq \frac{L}{t_{fligth}}$, where L is the distance travelled by the ion from the apex toward the detector. Equating both energy, this gives

$$\frac{m}{n} \simeq 2eV \left(\frac{t_{flight}}{L}\right)^2. \tag{2.5}$$

By analysing the time of flight of the ions, identification of ionic species can be made. Because it is almost impossible to evaporate only one atom with one pulse, multiple atoms will be field evaporated and detected.

One problem of field evaporation is that the exact time of departure (when field evaporation occurs) is not exactly known, which affects the measurement. The assumption made by the actual algorithm is that the atoms evaporate as soon as the laser pulse is sent. From the previous section on the heating mechanisms by a laser, it should be clear that delays in the apex temperature are possible, thus directly delaying also field evaporation. Furthermore,

because field evaporation is a thermal process in nature, emission of ions can happen at any temperature with a probability given by (2.2), especially after the maximal temperature of the apex has been reached. Field evaporation itself does not affect the time of departure because it has been shown theoretically to occurs in a few femto-second [20], very fast compare to the mechanisms of heating. What influence field evaporation are the conditions required to produce it.

2.2.2 Relation between time of flight spectrum and temperature

What an atom probe records are the average number of atoms evaporated in one pulse. Commonly, the mass spectrum is displayed in a graph with the number of counts on the y-axis and the time of flight on the x-axis. The mass spectrum is then called time of flight mass spectrum. The number of counts is directly related to the the detection rate ϕ_{detec}, which is the number of detected atoms over time.

One should not confuse the detection rate ϕ_{detec} with the evaporation rate ϕ_{evap}. From eq. (2.4), ϕ_{evap} can be interpreted as the rate at which ions are emitted from the specimen by field evaporation under an electric field E and temperature T. The detection rate is then defined as the integral over the duration of the pulse of this evaporation rate:

$$\phi_{detec} = \int_{\text{start pulse}}^{\text{end pulse}} \phi_{evap} \epsilon_D N_{At} dt, \tag{2.6}$$

where ϵ_D represents the detector efficiency, N_{At} represents the number of atom that can be field evaporated (only those at the surface apex will be evaporated). In eq. 2.6, it is assumed that the evaporation rate is the same for every N_{At} atoms. In the case of laser pulses, the temperature will vary over time, and so will the evaporation rate and $\phi_{evap} = \phi_{evap}(t)$

For simplicity, the following approximation (considering the temperature in $\phi_{evap}(t)$ is unchanged during the pulse duration) from [6] for the number of atoms detected per pulse is used,

$$\phi_{detec}(t) = \kappa \exp\left(-\frac{Q(E)}{k_b T_s(t)}\right), \tag{2.7}$$

where $T_s(t)$ is the apex temperature, κ depends on different parameters including ϵ_D, N_{At} , the applied DC field and the pulse duration. By knowing the apex temperature evolution, crucial information about the time of flight spectra can be deduced. The link between the number of detected ions and the temperature of the apex has been used to explain the time of flight spectra of silicon by many authors [6][40][23].

2.3 Hit map

In this last section, we briefly discuss about the hit detection of the emitted ions, and the parameter that influence the hit map.

2.3.1 Hit map information

Ideally, the apex shape should be perfectly axis-symmetric implying that the electric field is well defined and known (eq. (2.3)) and each atoms of the apex surface are heated uniformly at the same temperature.The evaporated atoms follow trajectories defined by the electric field, and hit the detector several macroscopic distance from the tip resulting in a magnified projected image of the tip sample. With algorithms, the positions of the detected ions can be computed.

The hit map represents the distributions of impact from a specific ionic species during an atom probe experiment. An example of an hit maps is shown in Figure 2.9 for the As species of an InAlAs tip. Consequently, the hit map of one ionic species gives a direct information of its distribution inside the tip.

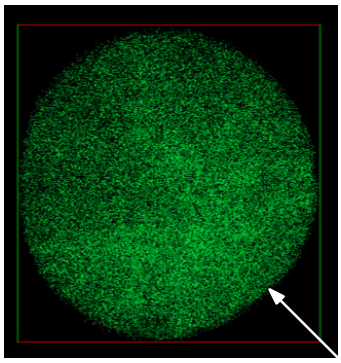

Figure 2.9: Hit map of As from an InAlAs tip. The white arrow indicates the direction of the laser pulses. Data from *Imec*.

2.3.2 Laser induced artifact

Standard reconstruction algorithms are purely based on geometry. If trajectories of the ions were known, perfect reconstruction would be possible. Actually, algorithms assumed the shape remains perfectly hemispherical during an experiment. There are, however, possible artifacts due to the shape of the apex and the laser interaction. It is worth mentioning first that in practice, the pulse laser is applied on only one side of the tip during an experiment.

In the case of a non-uniform heating (e.g. strong absorption on the laser side), the hotter side of the apex will have a stronger field evaporation. Thus, this side will be more evaporated than the shadow side, impacting the hit map as schematically represented in the upper part of figure 2.10 .

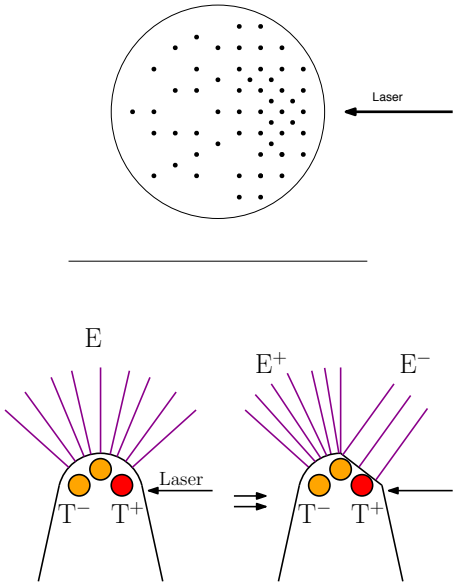

Figure 2.10: A non-uniform heating induces non-uniform field evaporation.

This stronger evaporation on one side can be interpreted in term of probability of field evaporation. Initially, the apex shape is hemispherical and the electric field on the apex surface is uniform (lower left part of figure 2.10). Suppose an incident laser induces a non-uniform

temperature distribution on the apex surface. Consequently, the probability of field evaporation is not constant on the surface. The resulting non-uniform evaporation of atom modifies the apex shape, flattening the evaporated side and indirectly sharpening the opposite side. The local curvature is changed, inducing changes in the local electric field, so that the cooler side has now a stronger electric field than the hotter side (lower right part of figure 2.10). In conclusion, during the evaporation, the apex shape is changing so that the probability of evaporation is kept constant over the surface of the apex as shown in Figure 2.10, breaking the uniform conical shape.

Consequently, the hit map is modified during the transient process, inducing artifact in the reconstruction algorithm. Understanding of these hit map in combination with information of the absorption map is important to understand the influences of the wavelength and power of the beam in atom probe experiment. This experimental hip maps of InGaAs will be analysed in the next chapter, and the absorption map in Chapter 4.

2.4 Summary

In this Chapter, we have discussed the main aspects of the laser pulse atom probe. The mechanisms of field evaporation where an atom is evaporated under the influence of an electric field has been described. Because this is a thermal process, thermal pulses can be used to induced field evaporation, which can be produced by absorption of a laser pulse. However, many difficulties linked with the mechanisms of laser absorption with semiconductors are presents.

We have then discussed about the use of mass spectroscopy with atom probe. The main challenge with mass spectroscopy in atom probe is to know the exact time of departure of the ions, which has been shown to depend mainly on the evolution of the temperature apex. This temperature evolution can cause delayed evaporation, thus impacting mass resolution. A model for the temperature of the tip apex will be proposed in Chapter 5.

Finally, the artifacts influencing the hit maps have been addressed. The importance of understanding the mechanism of absorption and the temperature evolution could greatly improve the interpretation of these hit maps and the accuracy of atom probe. Analising of the distribution of the internal electric field due to laser illumination is done in chapter 4.

Chapter 3

Laser Tip Interaction: From Si to InGaAs

In this Chapter, we first expose what are the previous results obtained for silicon, such as time of flight spectra and some hit maps, and what are the interpretations of them. Following this, we introduce the experimental results obtained for InGaAs tip by *Imec* and compare then to the silicon results.

Because of the novelty of using III-V semiconductor compound in the electronics and photonics domains, the use of the atom probe tomography technique with InGaAs samples is quite recent, and little work have been done on this subject. Previous conclusions obtained for the silicon with La-APT probe will then be used in the hope that it will explained the experimental results obtained for InGaAs.

3.1 Silicon

Silicon exists naturally in three isotopes with proportions given table 3.1.1. In the usual atom probe conditions, silicion field evaporated mostly in the form of a doubly charged ion.

Isotope	^{28}Si	^{29}Si	^{30}Si
Occurrence	92.18%	4,71%	3.12%

Table 3.1.1: Isotope of silicon an their natural occurrence [4].

3.1.1 Time of flight spectra

The time of flight spectra for Si^{2+} at 3 different wavelengths are shown in Figure 3.1. As it can be observed, for all the 3 wavelengths, there are 3 peaks, associated with the presence of the 3 possible isotopes. Their positions are shifted because the heavier the atom, the longer the time of flight for the same ionic charge.

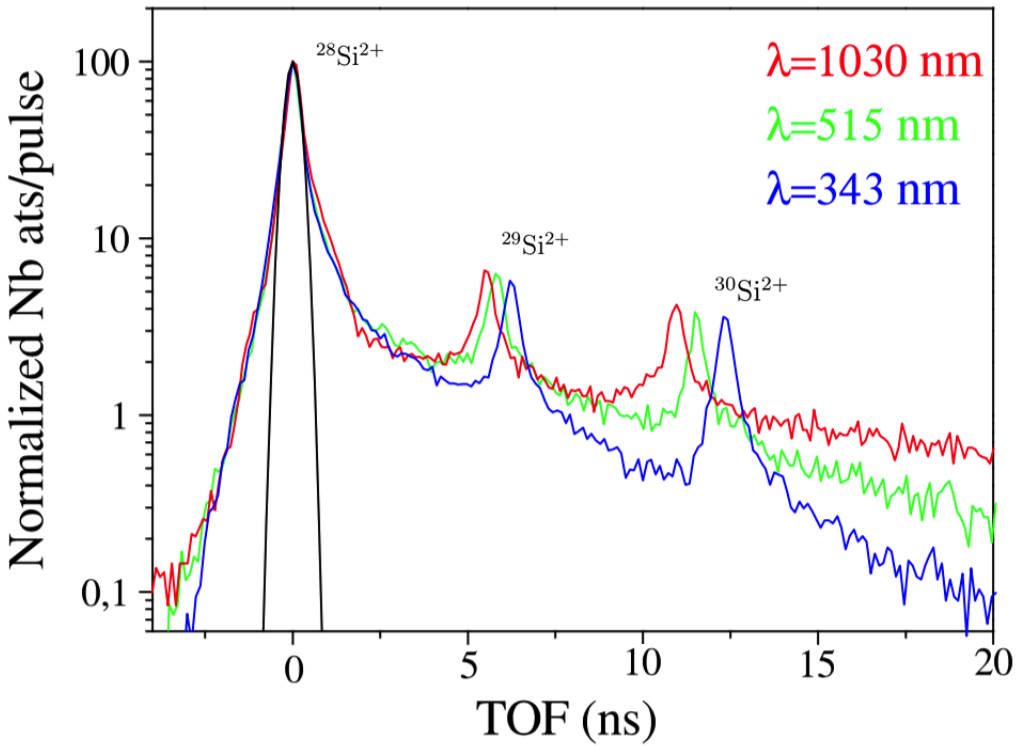

Figure 3.1: TOF spectrum on semi-log scale of Si^{2+} peak for different laser wavelengths. The time axis start when the laser pulse is sent. Reproduced from [42]

.

Neglecting for instance the presence of the 2 smaller peaks associated to $^{29}Si^{2+}$ and $^{30}Si^{2+}$, the shape of the time of flight spectrum for all 3 wavelength presents a similar sharp peak (∼2 ns) followed by a different slow decreasing curve for the number of detected hits called "tail" after the sharp peak, which takes place during several nano-second (∼15-20 ns) after the laser pulse has been send. It can be noted that the mass resolution is better as the wavelength goes from IR to green and green to UV.

3.1.2 Thermal cooling: a slow process

In the last chapter, it has been hint that the number of detected hit is linked to the apex temperature if we consider the field evaporation as purely thermal. Thus, the slow decreasing in the number of evaporated ions (the "tail") is associated to the cooling of the apex temperature and indicates that the cooling time of the apex should be on the order of the nano-second. A thermal diffusion model coupled with drift-diffusion continuity equations for the carriers have been used in [6] [23] [40] to obtained the cooling temperature of the apex. After injecting the temperature in (2.7), their solution correlated quite well the slow decreasing of the TOF spectra of silicon. It indicates that the cooling time of the apex is on the order of 15-20 ns.

The difference in mass resolution can then be explained by looking at the energy absorption maps for the different wavelength as shown in Figure 3.2 As it can be seen, for UV, silicon is strongly absorptive (see Appendix A) almost like a metal and the incident laser is absorbed near the surface. On the contrary, in IR and green, the energy is absorbed in certain regions inside the volume. Consequently, for green and IR, heat must flow toward the apex to trigger field evaporation. The cooling of the heat toward the base of the tip following the rise in apex temperature is then slow down for green and IR compare to UV because the temperature gradients are weaker inside the volume. IR is the worst case, because the patch of energy is

located even further from the apex than for green.

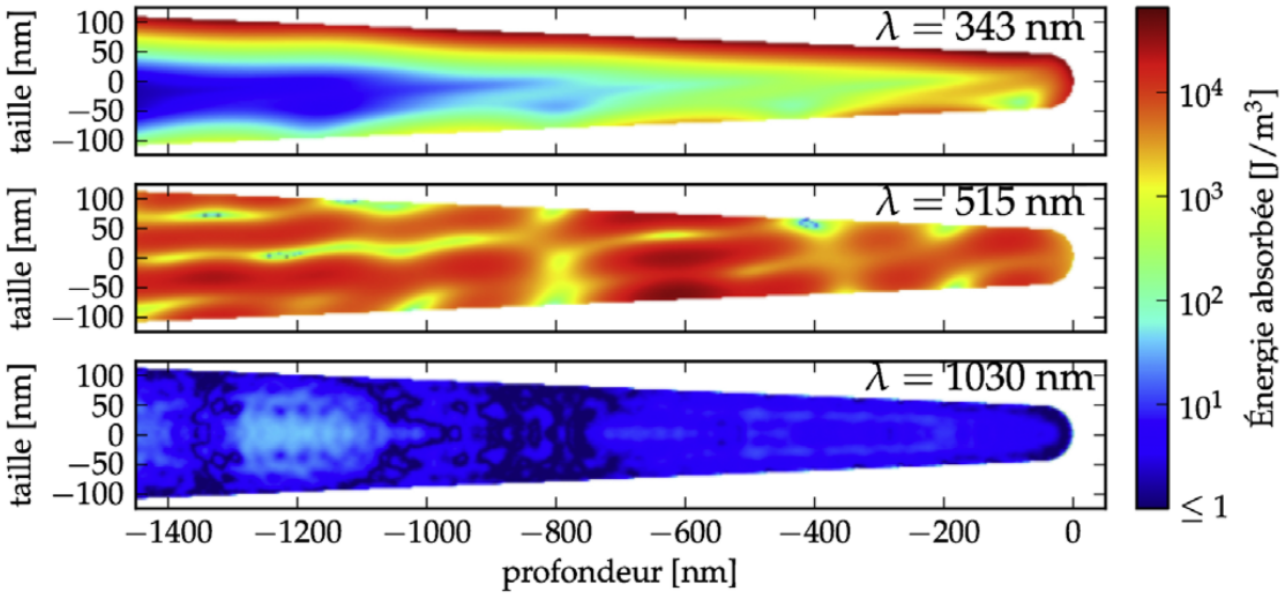

Figure 3.2: Absorption maps of Si tip illuminate with (a) UV light $\lambda = 343$nm, (b) green light $\lambda = 515$nm and (c) IR light $\lambda = 1030$nm. Reproduced from [42]

Sharp peak

However, this absorption map and cooling process cannot explain the fast emission sharp peak observed before the thermal tails (black curve in Figure 3.1). The first reason for this is that the peak is the same (same rise time, same width, same decay time) for all wavelength, thus it is independent from the absorption map. The second reason is that the thermal model neglect the presence of the DC field and surface states of silicon[40].

This peak is usually associated by field induced surface absorption of the laser pulse [20][19][42]. The origin of this narrow peak will not be discussed in this thesis, as it would require another full detail analysis out of the scope of this thesis.

Thermal hump

When the intensity of the laser is increased with IR, a second broad peak , called the "the thermal hump", in the time of flight spectra is visible several nanosecond after the first narrow peak as seen in Figure 3.3. The broader peak of a few nanoseconds is explained by a temperature evolution of the apex and often attributed to a delayed heating of the tip apex, originating from a volume laser absorption at some distance from the apex, which has been shown in [40] using the two temperature model coupled with drift-diffusion continuity equations. In Figure 3.2, the absorption of energy by silicon with IR is mainly made in volume at some distance form the apex. Thus, after the first usual narrow peak, the apex is heated by a delayed heating and this field evaporate some more atoms. Figure 3.3 also shows that the time of flight spectra of silicon tips depends on the power(intensity) of the laser.

Practically, IR pulses with silicon tips are not used, but the "thermal hump" shows clearly that the field evaporation is temperature dependant and hints the importance of the knowledge of the absorption maps.

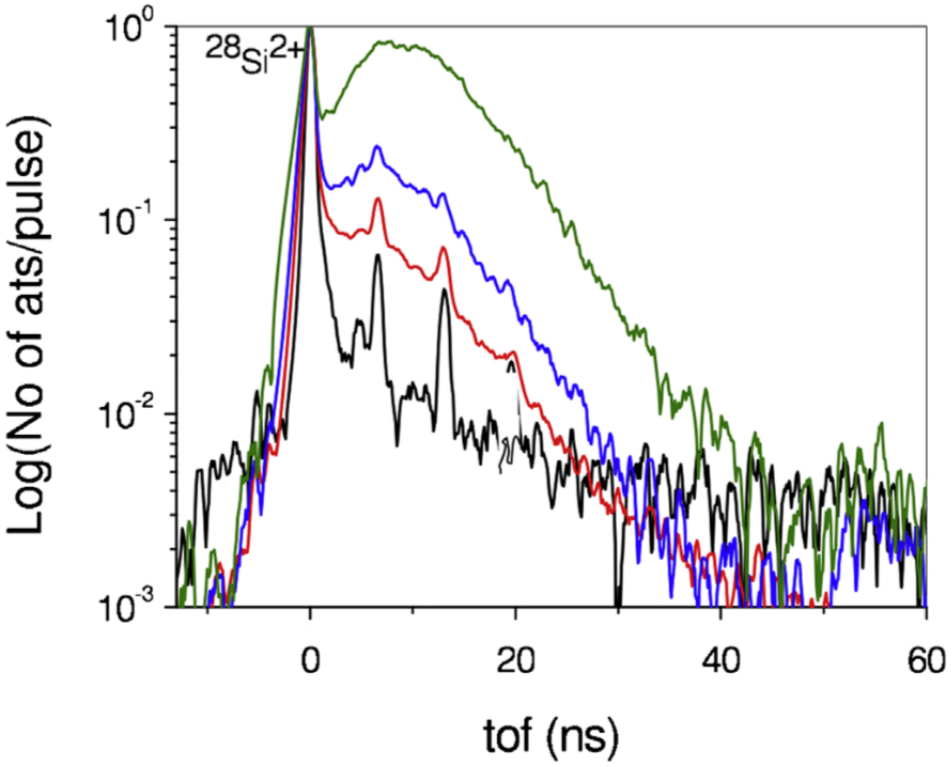

Figure 3.3: TOF spectra of Si^{2+} (a) for IR laser. Black line I=40.2 GW/cm^2, red I=41.2 GW/ cm^2, blue I=42.2 GW/cm^2, and green I=45.7 GW/cm^2, respectively. The broad signal after the sharp peak is the *thermal hump*. Reproduced from [42]

.

3.1.3 Hit maps

When using UV laser pulse with silicon, it is often observed with the hit maps that singly-charged silicon ion are evaporated on the laser side and doubly-charged on the dark side. The charge states of a field evaporated ions is directly linked with the electric field. The stronger the electric field, the more charge can be drained from the atoms. Thus this means that the electric field is stronger on the dark side.

In fact, by looking at the absorption map of UV figure 3.2, the absorption of the energy is confined near the illuminated surface. Thus, the temperature is higher, and a one sided evaporation occurs. This modifies the shape of the tip apex so that the electric is then lower on the hotter illuminated side and higher on the dark side. For green, the absorption is made into the volume and heat will flow more uniformly toward the apex. Thus, there is no one sided evaporation and tips shape under green illumination do not deform. The SEM images after an atom probe experiment with UV show clearly the modification of the apex shape, which is not the case for green as seen in Figure 3.4.

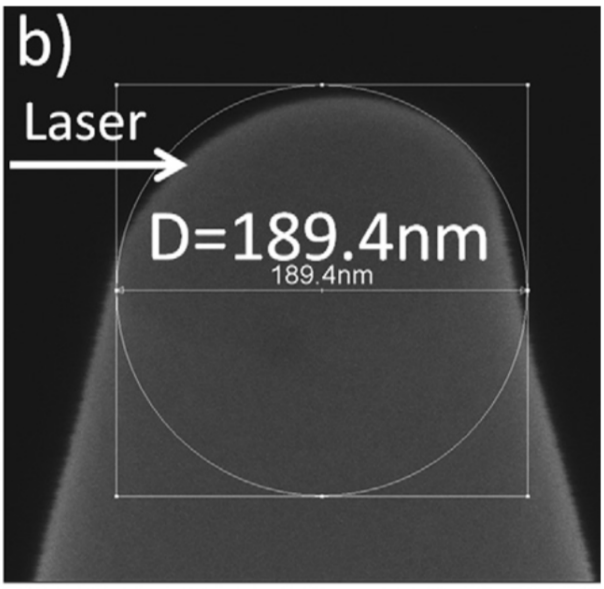

Figure 3.4: SEM image of a silicon tip after analysis with UV laser.Reproduced from [36].

Transient hit maps

The hit maps from silicon tip using UV illumination after the tip has been used under green illumination and the reverse (from UV to green illumination) are shown in Figure 3.5((a) and (b) respectively). The hit map on the left (b) shows that there is a one sided evaporation on the laser side. This is simply explained by the precedent observation: green illumination does not induce one sided evaporation, but UV does. Consequently, the tip after green illumination has kept is hemispherical shape before UV illumination is used.

The hit map on the right (b) shows also a one sided evaporation, but on the other side of the laser. Here, the tip has been first used with UV illumination, which has modifies its apex shape because of a one sided evaporation. When using green, the heating is uniform at the apex because of the heating in volume away from the apex. Thus, the temperature of the apex is uniform, but the electric field is not because of the previous UV illumination (the dark side has a higher field). The dark side will now be more field evaporated, which is seen on the hip map. This conclusions can be once again be interpreted in term of tendency to keep an uniform probability of field evaporation on the surface.

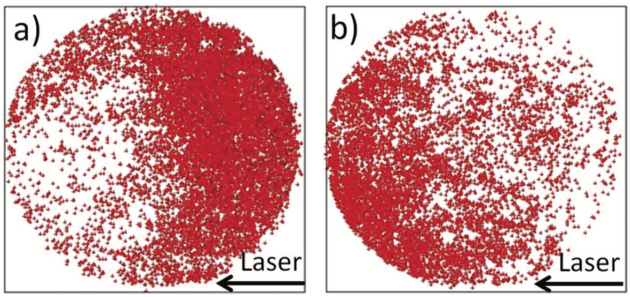

Figure 3.5: Hit maps after switching the laser wavelength: (a) green to UV and (b) UV to green.Reproduced from [36].

3.2 InGaAs

In this section, we now present the recent results obtained at *Imec* with InGaAs tips and compared the results with those of silicon. The InGaAs alloy used in the current atom probe experiment of *Imec* is $Ga_{47}In_{53}As$, which is the most important alloy composition from technological and commercial point of view. In this thesis, we drop the nomenclature as we are only concern with one composition ($Ga_{47}In_{53}As$).

Since it is an alloy, several different ionic species can be presents during field evaporation. However, the mechanisms underpinning the field evaporation for each individual ionic species at the surface of the InGaAs is the same when subjecting to same conditions (temperature, electric field). Thus, the time of flight mass spectra of the different ionic species are essentially the same within a same experiment. For convenience, Indium is taken as reference in this thesis. Indium (In) exists naturally in 2 isotopes with proportions given table 3.2.1. In the usual atom probe conditions, Indium field evaporated mostly in the form of a singly charged ion, $^{115}In^{+}$, and the its peak is the largest one, which is the reason why it is taken as reference.

Isotope	^{115}In	^{113}In
Occurrence	95.7%	4,3%

Table 3.2.1: Isotope of Indium an their natural occurrence [3].

3.2.1 Time of flight spectra

The results of the time of flight spectra for InGaAs tips at different wavelengths are shown Figure 3.6. The first striking observation is that all the 3 different time of flight spectrum look identical, meaning it is independent from the wavelength used.

The second observation is that we also recover a first narrow peak followed by a slow decreasing in the number of evaporated atoms, similar to what was observed for silicon. Although the tails seems to drop faster in InGaAs (3 decays in 10 ns) compare to silicon (3 decays in 20 ns), the slow decreasing is also expected to be described by a temperature evolution of the apex. However, the mechanisms of absorption regarding the three wavelength with InGaAs seem to lead to the same cooling time of the apex temperature (∼10ns).

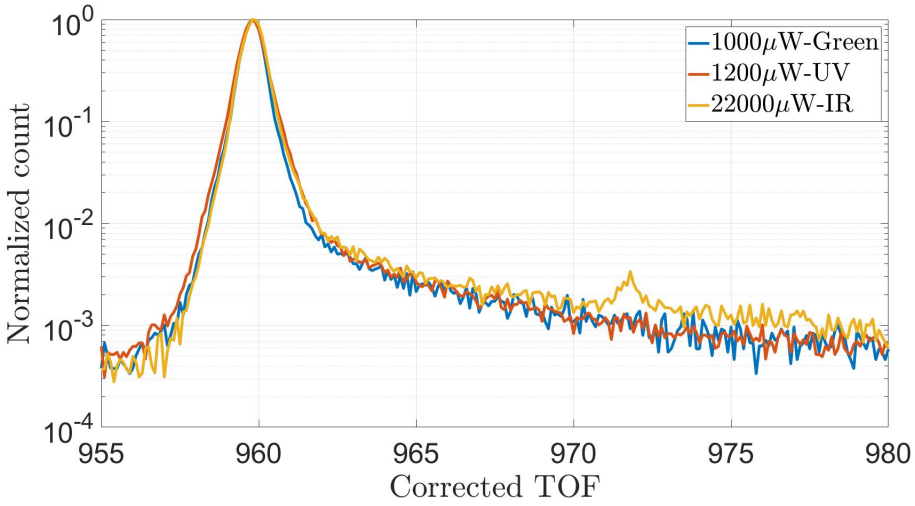

Figure 3.6: Time of flight spectra of ^{115}In for InGaAs tips with different laser wavelength in La-Apt machine. Data from *Imec*.

Influence of the power

It has been shown that the intensity of the laser has an influence on the time of flight spectra of silicon (Figure 3.3). The results for different green power are shown in Figure 3.7. Here again, we observe that the shape of the time of flight spectra of InGaAs seems independent regarding the power used. The slow decreasing in the number of counts is not influenced by the power used. This is an interesting observations, because a higher power would mean a higher energy fed into the tip resulting in a higher apex temperature. However, InGaAs tips seem to cool down always with the same cooling time.

The small secondary peak in appearing for green illumination with 200μW power is an hybrid of ^{115}In. When looking at the mass spectrum of the 200 μW green measurement it can be observed that this peak is at exactly 2 Dalton from the main peak. This could only mean that this corresponds to a hydride of ^{115}In, i.e., InH^{2+}.

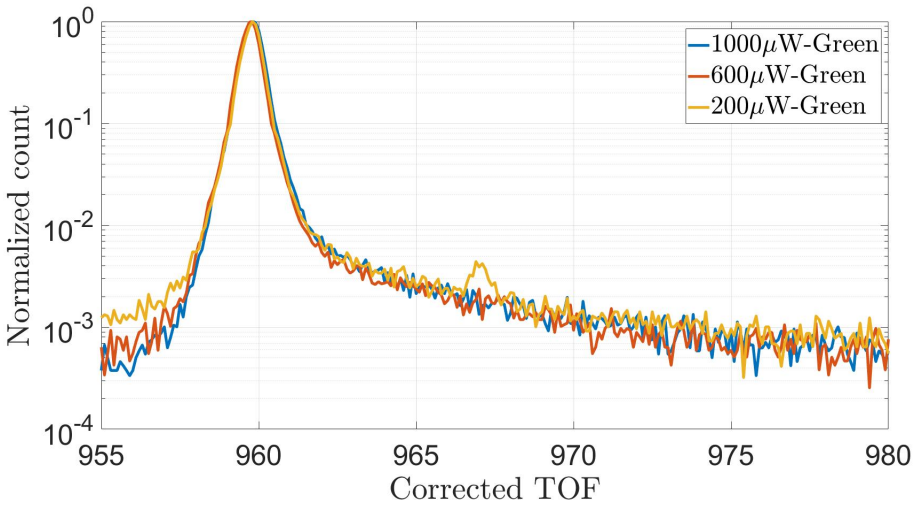

Figure 3.7: Time of flight spectra of ^{115}In for InGaAs tips under green illumination with different laser power in La-Apt machine. Data from *Imec*.

3.2.2 Hit maps

In this section, some results obtained recently for the hit map of InGaAs are discussed. First, we look at the influence of UV illumination on InGaAs tip. It can be observed that initially, by using a 3000μW UV illumination, a one sided evaporation is observed , resulting in the modification of the apex shape of the tip as seen in Figure 3.8, similarly as observed for silicon tip under UV illumination. On the resulting hit map figure 3.9a, this is clearly seen by strong non uniform density of impact.

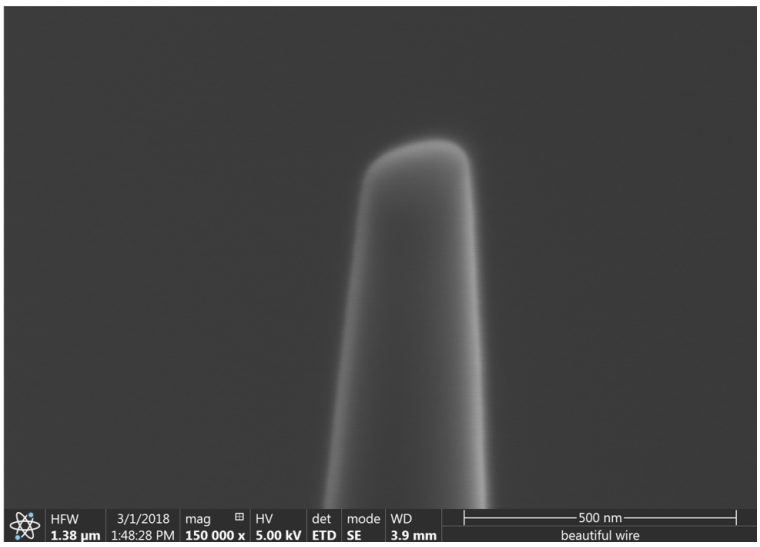

Figure 3.8: SEM image an atom probe tip measured at 3000 μW with UV after 22M atoms. SEM image from *Imec*.

Transient hit maps of a tip are hit maps obtained for different illumination conditions, but with the same tip between each recorded data. Transient hit maps for a tip initially under high power UV illumination and then under low power UV illumination are shown in Figure 3.9b,3.9c and 3.9d. In Figure 3.9b, one sided effect is present during the successive hit maps, opposite to the laser side. In fact, the situation here is similar to the one observed for silicon when switching from UV to green (Figure 3.5b). This means that initially the high power UV has lead to a one sided evaporated on the laser, modifying the apex shape. Then, when using the low power UV illumination, the temperature at the apex was more uniform, but not the local electric field, resulting in a one sided evaporation opposite to the laser side.

When looking at the hit map after some time with the same low power UV illumination in Figure 3.9c, the density of hit is still higher on the dark side, but not as strong as in Figure 3.9b. This is a direct consequence of the tendency of the apex shape to evolve in order to keep an uniform probability of field evaporation on the surface. As the dark side is more evaporated in Figure 3.9b, the apex shape evolves so that the electric field becomes weaker on this side. In the end, the density of hit becomes more uniform as seen in Figure 3.9d. The average density of hit for each hit map is given in Figure 3.10. From figure 3.10b to figure 3.10c, the density becomes less intense on the dark side, and in Figure 3.10d, the density is almost "uniform".

From the previous observation, InGaAs tips absorption with UV is mainly one sided. In order to get more detailed information on the distribution of absorbed energy, the distribution of the internal electric field inside illuminated tip will be analysed in the next chapter.

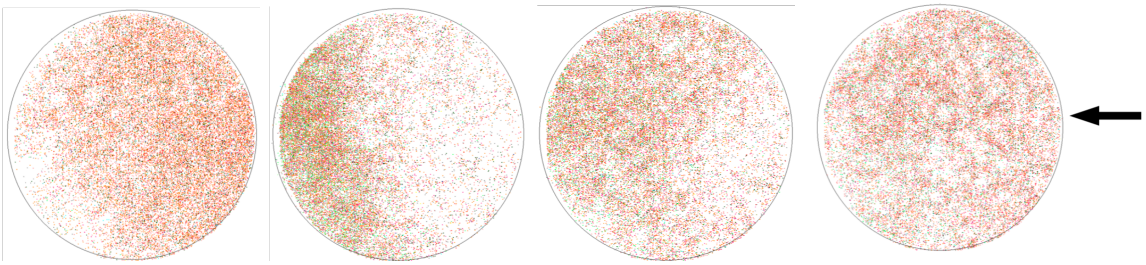

(a) UV-3000 μW (b) UV-200 μW (c) UV-200 μW (d) UV-200 μW

Figure 3.9: Hit maps for InGaAs tip under different initial configuration. The black arrow indicates the laser side. (a) Hit map with high power UV illumination, with previously no evaporation. (b) Hit map with low power UV illumination, with previously the tip from (a). (c) Hit map with previously the tip from (b).(d) Hit map with previously the tip from (c). Data from *Imec*.

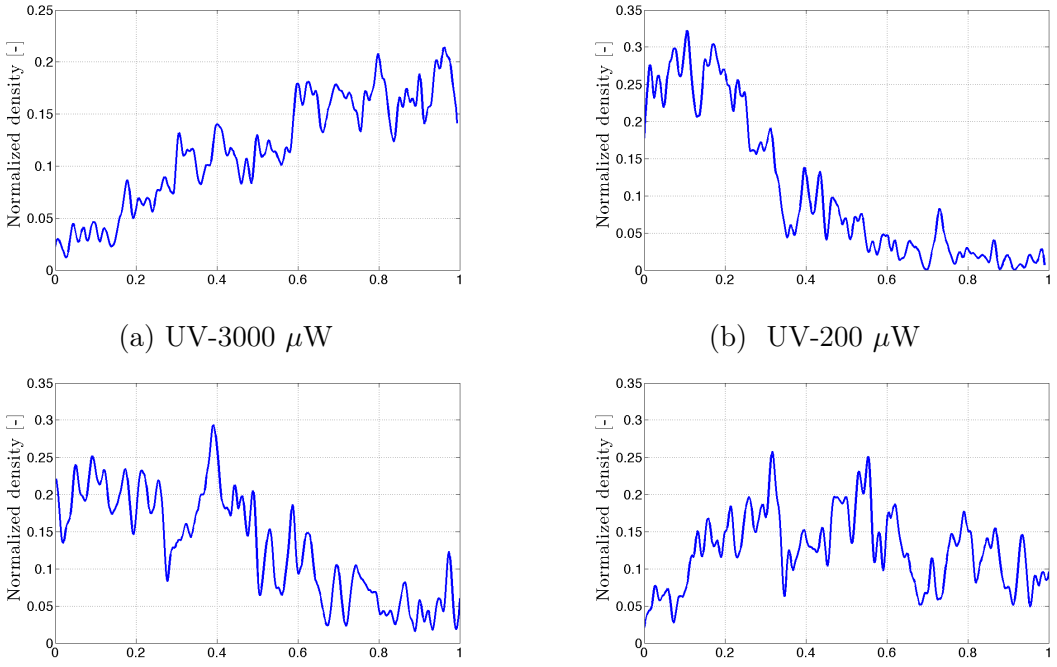

(a) UV-3000 μW (b) UV-200 μW

(c) UV-200 μW (d) UV-200 μW

Figure 3.10: Average density of hit of the hit maps from Figure 3.9.

3.3 Summary

In this chapter, we have described experimental results of laser atom probe with silicon tip from the literature. The TOF spectra for silicon tip presents a sharp peak followed by a slow decrease in the number of counts which depends on the laser wavelength. This slow decrease is explained by a thermal cooling of the apex and is influenced by the distribution of the absorbed energy, which depends on the laser wavelength. For InGaAs, a sharp peak followed by a slow decreasing is also recovered, but it is not dependant on the wavelength used, neither on the power used. In order to see if this observations can be explained by a thermal evolution as it is the case for silicon, estimation based on simple models for the apex temperaton will be amde in chapter 5.

The way energy is deposit inside the tip also influence the hit maps. When analysing transient hit maps (changing the illumination conditions but keeping the same tip), the shape of the tip obtained after a given laser illumination influences the local field evaporation when changing the laser illumination, impacting the hit maps. Thus, understanding of the distribution of the absorbed energy is important in order to explain changes in the hit maps. In the next chapter, the distribution of internal electric field of illuminated tips will be made.

As an example, for silicon tip, UV illumination leads to one sided evaporation, which sharpened the shape on the dark side of the tip. By looking at the absorption map, one sided energy absorption on the laser side is seen and is coherent with the one sided evaporation.

Chapter 4

Light Interaction with nano-scale tips

In this chapter, we discuss the laser interaction with the InGaAs conical tip by looking at the distribution of the internal electric field of the tip when illuminated with light. To obtain the distribution map inside the InGaAs tips, the numerical code, ADDA (Amsterdam Discrete Dipole Approximation), will be used.

In the first section, we briefly explained the hypothesis made and how the laser interaction with the tip will be numerically computed. In the second section, we present and described numerical results obtained with ADDA for InGaAs tips. Some parameters will be varied to analysed their influences on the distribution maps. The link with the experimental results will also be made in this section.

In the third section, different levels of geometrical refinement with increasing complexity will be used to explain the interaction with light and nano-scale conical tips, in order to provide a better understanding of the way light couple with maps. This section aims at understanding how energy is absorbed and the influence of the parameters, not give a full accurate solution of the real problem.

4.1 Numerical scheme and hypothesis

4.1.1 Hypothesis

In the laser assisted atom probe, a specimen is subjected to a laser pulse of duration $T_{pulse} = 500$fs focused on the apex incident normally to the tip's axis of symmetry with a linear polarization parallel to the tip's axis. The parallel polarization is chosen for practical reason, because absorption is higher with a parallel polarization. Thus, for the same laser power, a smaller DC bias voltage is required to induce field evaporation. This has been shown experimentally in [14]. Because it is complex to model the real situation, simplifications will be made.

In reality, to model the interaction between an electromagnetic wave and a semiconductor, one should consider a variable complex refractive index depending on the actual band populations, and the local electric field (influencing the band structure). But this brings too much complexity into the problem, and ADDA is not able to take time variable refractive index. Thus, the first simplification is that in the rest of this chapter, InGaAs will be considered as an isotropic dielectric material with refractive index $\widetilde{n}$ complex, depending on the wavelength used. Regarding the laser pulse, we consider simply the simulation of tip illuminated on one side at 3 different wavelengths: green (515nm), UV(343nm) and IR(1030nm). The refractive index of InGaAs and Si associated to this wavelength can be found in appendix A.

The tip geometry is modelled as a cone of shank angle α with hemispherical cap of apex

radius R_{apex} and length L, as shown in Figure 4.2 (left). Typical value for the apex radius are 20-100 nm, 3000-5000 nm for the length and 2-6°for the shank angle.

4.1.2 ADDA-Numerical constraints

Input parameters

ADDA [45] is an open source program which can simulate light scattering of 3D object of any shape and composition using the discrete dipole approximation DDA. In the discrete dipole approximation, the scatterer is replaced by a set of small cubical subvolumes ("dipoles") as shown in Figure 4.1. Dipole interactions are approximated based on the integral equation for the electric field. More detailed information on the mathematical DDA formulation can be found in [46][28].A more detailled information on the physical interpretation of the DDA formulation can be found in [34]. In this thesis, we used ADDA- Version 1.3b4.

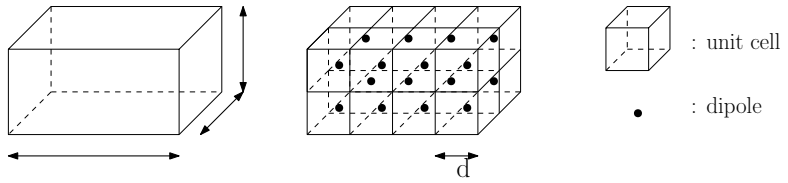

Figure 4.1: The discrete dipole approximation DDA method consider the sample as a ensemble of small cubical dipole of size d.

In order to run an ADDA simulation, several information must be provided to the program: the type of output data, the geometry of the scatterer (defined by the position of each dipole), the wavelength of the laser, the refractive index of the scatterer, the polarizability of the dipole constituting the scatterer, the relative error of the integration, the orientation of the scatterer with respect to the incident beam and the number of dipole per wavelength or equivalently the dipole size.

What we are interested in this chapter, is the distribution of the internal electric field, and more specifically its amplitude ADDA is able to compute directly the square of the internal electric field of the scatterrer. The geometry of the scatterer is defined as shown in Figure 4.2 (right). The default polarizability is chosen, as we are not concern about this here. The relative error is 10^{-5}, which is chosen as a balance between precision and computation time.

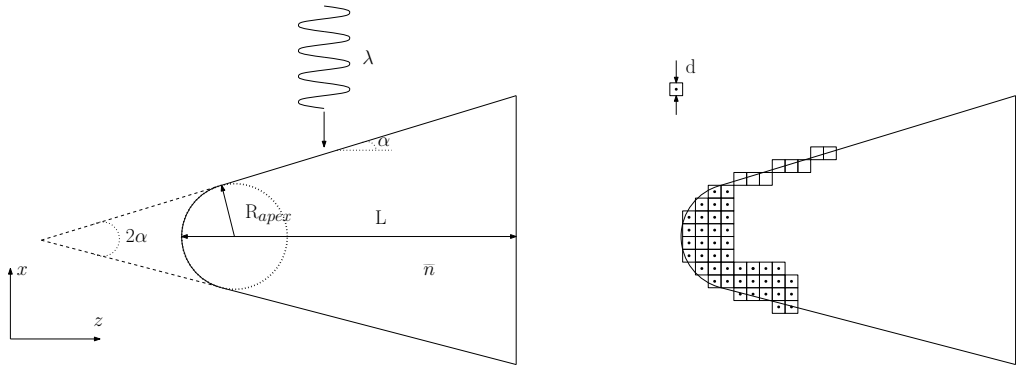

Figure 4.2: (left) Geometry of the conical tip. α is the shank angle, L the tip Length, R_{apex} the apex radius, $\widetilde{n}$ the refractive index of the material and λ the wavelength of the incident beam. (right) Discretisation of the volume with small cubical volume call of size d call dipole.

The *dpl* number

The number of dipole per wavelength, *dpl*, is what define the convergence of the solution. ADDA recommends, as a rule of thumb, the dipole size to be $d = \lambda/(10\,|\widetilde{n}|)$, where λ is the wavelength of the incident beam and . However, this has been shown to give a precision of a several percent for small particles in free space with refractive index $|\widetilde{n} - 1| < 2$ [45], which is not the present case for the InGaAs refractive index at all the wavelength considered (see Appendix A).

In the case of high refractive index such as InGaAs, ADDA explains that errors do not significantly increase with the size of the scatterer by choosing the number of *dpl* with the rule of thumb, but do significantly with increasing the refractive index $\widetilde{n}$. Thus, it is recommended by ADDA to use more *dpl*, but the computation time then increases. On could expect that by decreasing the dipole size by a factor of 2, the computation time would increase by a factor of 2^3 as we work in a 3D volume, but this dependence is not true and depends once again on the refractive index. For example, simulations have been performed for a material with $\widetilde{n} = 2$ and it took half a day compare to a few tens of second for a material with $\widetilde{n} = 1$ for the same volume size on 64 processors [45]. What limits the use of more *dpl* is the available computer resources.

Thus, in this thesis, we rather require the size of the dipole to be below the penetration depth in the hope that it will be sufficient to represent correctly the interaction between the tip and the laser illumination. If the size of the dipole was larger, one dipole would not be able to represent the penetration depth. The penetration depths[1], $\delta = \frac{\lambda_o}{4\pi n_i}$ with $\widetilde{n} = n_r + in_i$, of silicon and InGaAs are given in Table 4.1.1.

	green	IR	UV
Si	1.05e3	82e3	9.1
InGaAs	43.1	315.2	14.2

Table 4.1.1: Penetration depth (nm) for wave incident on a infinite volume of silicon or InGaAs for 3 different wavelengths.

As it can be seen in Table 4.1.1, if we want at least 5 dipoles to represent the penetration depth in the case of UV for InGaAs, the dipole size must be smaller than $d \leq 14.2/5 \sim 2.8$nm. The rule of thumb from ADDA, however, gives $d \sim 9.37$nm. Our choice is motivated as a balance between reasonable computation time and sufficient precision and the hope of a good convergence. Additionally, the size of the dipole must be at least small enough to correctly represent the actual volume of the tip. For example, if we have a tip with an apex radius $R_{apex} = 25nm$, we required at least the dipole size to be at most $d = 5nm$.

One drawback of using ADDA is that it is difficult to estimate if the solution has converged for complex shapes such as the conical tip, since no analytic solution can be used. It must be clear that the relative error imposed in the simulation is only an error on the numerical integration. Thus, although the numerical scheme converges, the physical meaning fullness of the solution is questionable. In the case of special shape, such as sphere, by increasing the

[1]The intensity is proportional to the square of the electric field, which for a plane wave propagating inside a medium of complex refractive index $\widetilde{n} = n_r + in_i$ (n_i is the extension coefficient) is given by $\mathbf{E}(z,t) = \mathrm{Re}\left[\mathbf{E}_o e^{i(\widetilde{k}z-\omega t)}\right] = \mathrm{Re}\left[\mathbf{E}_o e^{i(2\pi\widetilde{n}/\lambda_0 z-\omega t)}\right] = e^{-2\pi n_i z/\lambda_0}\mathrm{Re}\left[\mathbf{E}_o e^{i(kz-\omega t)}\right]$. I$= |\mathbf{E}|^2 \propto e^{-4\pi n_i z/\lambda_0} = e^{-z/\delta}$ and the penetration depth is the distance after which the intensity is reduced by 1/e

number of *dpl*, the solution tends to converge. We will then assume in this thesis that it will be also the case for the conical tip.

Remarks

Several remarks can be made. The construction of the tip volume with a discrete number dipole of finite volume leads to several artifacts. The first one is the creation of stairs case sidewalls as shown in Figure 4.2. The consequence of this stairs case sidewalls is the apparition of high intensity electric field in the corner of them as shown in Figure 4.3a. This impacts the actual maximal value which can be wrongly interpreted on the absorption map. However, it affects only locally the electric field.

The second remark is the apparition of a surface layer which doesn't seem affected by the electric field as seen for example in Figure 4.3a. This effect has not been investigated and might be a numerical artifact. However, it doesn't seem to have an impact on the distribution of the internal electric field other than the apparition of a layer with no electric field in (x,z) cut plane.

Finally, the usual tip dimensions are $R_{apex} \sim$ 25-150 nm, L$\sim$ 4000-5000nm and $\alpha \sim$ 2-10°. However, it is not possible to run simulation of real tips while keeping the dipole size constant so the tip must then be made shorter.

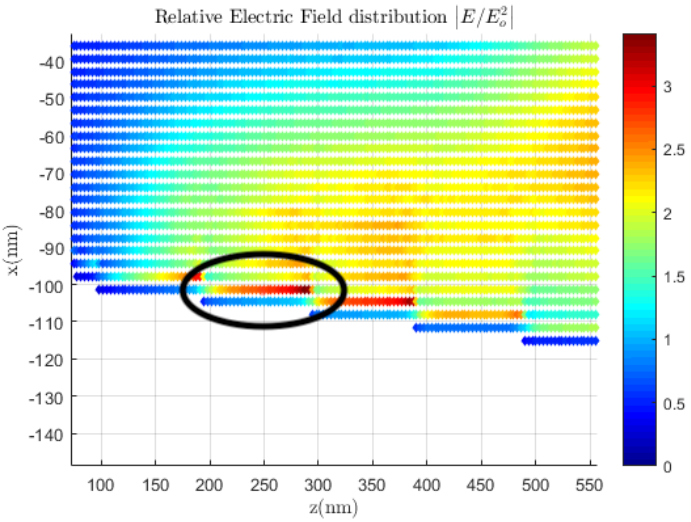

(a) Zoom of a transversal cut of ADDA simulation for an InGaAs tip: creation of stairs case sidewalls leading to artificially high intensity of the electric field in their corner.

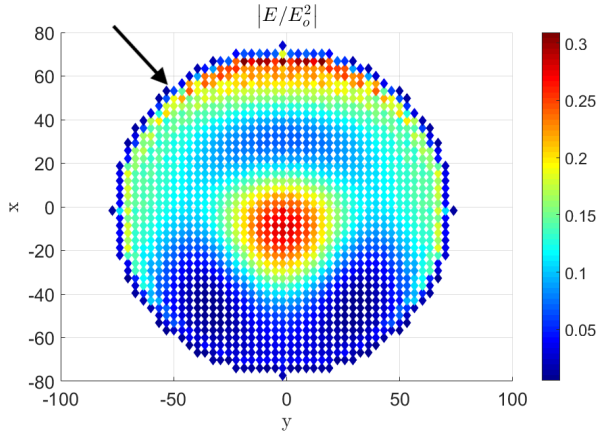

(b) Axial cut of a ADDA simulation for an InGaAs tip: apparition of of a layer with zero internal electric field.

Figure 4.3: The discrete dipole formulation leads to several artifacts: (a).creation of strair case sidewalls and (b) apparition of a surface layer with no internal electric field.

4.2 Numerical Results

4.2.1 Influences of the wavelength

First, we start by showing simulations for 3 different wavelengths with a tip of radius $R_{apex} = 50$nm, shank angle $\alpha = 2°$ and length L=1.5μm. The reason the tip is not longer is due to computer resources. Simulation with longer tips can be run in a reasonable amount of time, but the number *dpl* must then be decreased. The problem with making tips longer is that it does not increase the number of dipole linearly, but more than that since it is a cone.

UV

When UV is used, most of the intensity of the electric field is located near the surface as seen in Figure 4.4a, which is expected because of the stronger damping of InGaAs in UV. The pen-

etration depth is 14.2 nm, much smaller than the dimension of the tip, except close to the apex.

Thus, this correlate quite well with the results observed in the transient hit maps figure 3.9. Since most of the intensity of the electric field is located near the surface, it can be expected that most of the energy is absorbed in this region. Thus, UV illumination can effectively lead to a one-sided evaporation on the laser side which modify the shape of the apex.

Green

When green laser is used, the intensity of the electric field is located at specific regions (R∼45,55,62 and 87 nm) inside the volume of the tip as seen in Figure 4.4b. They result from constructive interferences as it would be shown in the last section of this chapter.Two maxima are located close to the apex for this specific geometry (apex radius, shank angle, length) and the most intense is located on the laser side. What is interesting is the fact that a maximum of intensity is observable for large radius (R∼87nm at z=1400nm), which is not really expected because the penetration depth is 43.1 nm in green with InGaAs and the wave needs at least to travel an approximate 125 nm before reaching these regions. The origin of this maximum as well as their location are discussed later in this chapter.

IR

When IR is used, the situation is similar to the green case, maxima are located at specific radius (R=60 and 90 nm). However, the maxima in Figure 4.4c are located further away from each other and the maximun at R=90 is expected (penetration depth is 315.2 nm with IR) compare to the unexpected maximum at R∼87nm for green. The larger spacing between the 2 maximum is a consequence of the longer wavelength of IR (1030 nm) than green (515 nm) as it will be explained later. Note that the intensity of the maxima is higher with IR than with green, consequence of the smaller damping in IR than in green, which lets more constructive interferences to occur between the multiple reflected wave inside the tip.

From the previous observation, it must be clear that not only the wavelength does influence the distribution of internal electric field map, but also the penetration depth. For UV, since the penetration depth is 14nm, this means that practically the intensity will be located near the surface almost all the time. For IR the penetration depth is 315.2nm, thus, an absorption in volume is always expected if we consider the practical dimension of a tip. For green, the penetration depth is 43.1nm. Here, the situation is intermediate, depending on the dimension of the apex, the intensity can be expected to be either located mostly in volume for small apex radius, or mainly on the surface for large apex radius. This is discussed here below.

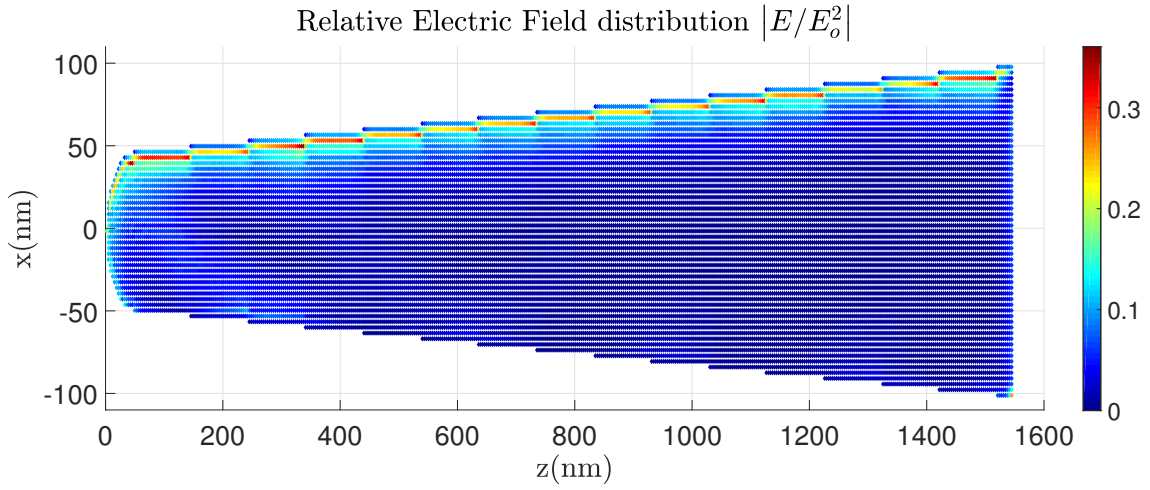

(a) UV.

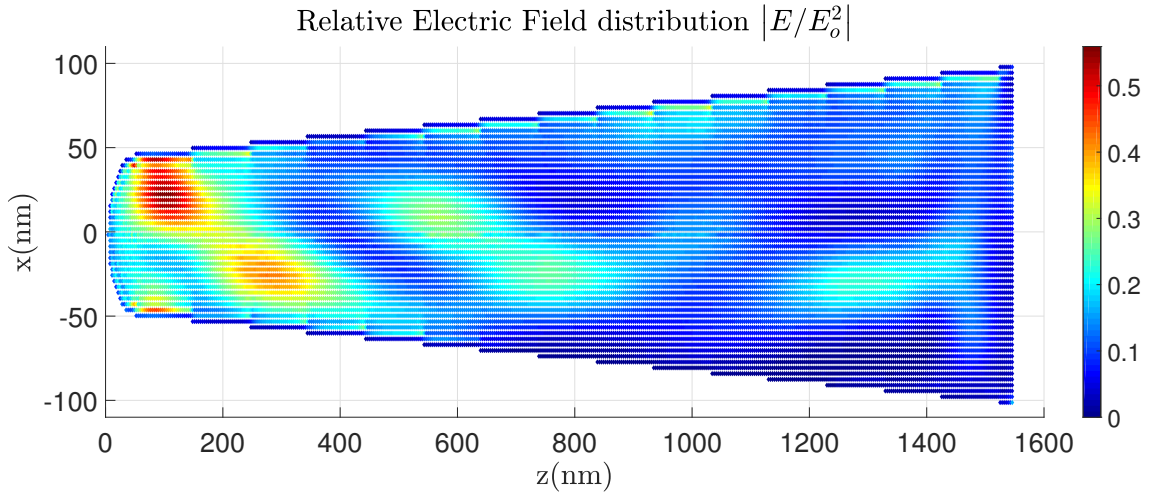

(b) Green.

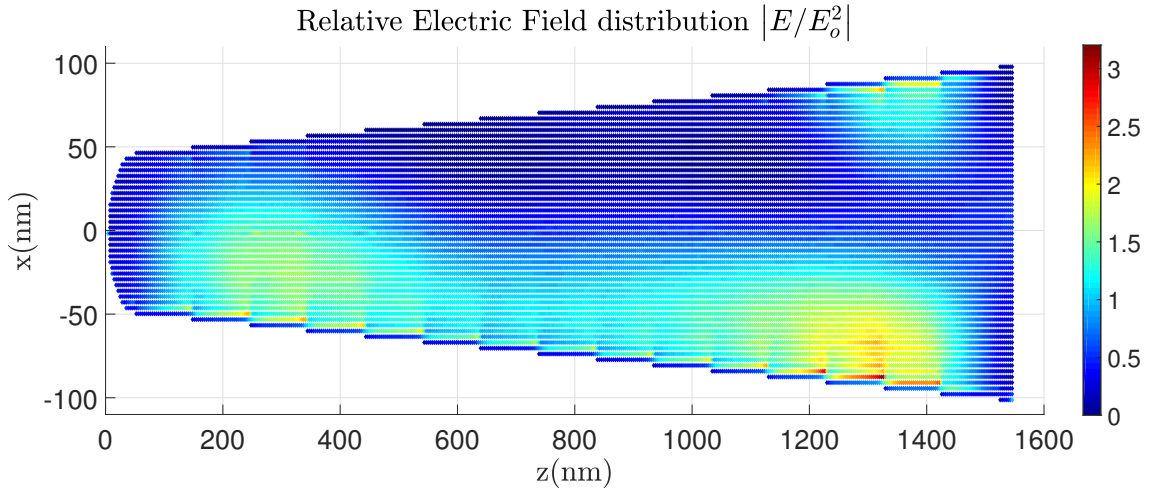

(c) IR.

Figure 4.4: ADDA simulations with InGaAs tip for different wavelength. Apex radius R=50nm, length L=1.5μn and shank angle $\alpha = 2°$. (a)UV with a number of dpl=100, (b)green with a number of dpl=150 and (c)IR with a number of dpl=300.

4.2.2 Influences of the apex radius

We now look at the influence of the apex radius for each wavelength. The analysis of the difference radius is useful because during an experiment, the apex radius will increase as the tip is progressively evaporated. One problem with the current La-ATP machine is the impossibility of making in-situ imaging of the tip. So, we don't know the apex radius unless we take it out of the tool. Once we take it out, it is usually not possible to re-start the tip in the atom probe tool without performing a focused ion beam (FIB)[2] cleaning step (which modifies again the radius). By understanding how the electric field distribution changes with the apex radius, it is possible to see where energy will be mostly absorbed and predict important effect such as one-sided absorption.

Because it is not possible to simulate large volume with a large number of *dpl*, restriction have to be made on the geometry. When increasing the apex radius while keeping the same length (figure 4.2 left), the number of dipole increase more than proportionally and computation time increases drastically. Thus, when the apex radius is increased, the length will be decreased to keep a reasonable computation time. Note that since ADDA simulates the scattering of the tip considering its real dimension to get the internal electric field. Thus, 2 tips with different length will have different internal electric distribution, considering for example effect cavity effect. However, as it would be explained in the last section of the chapter, the solution for the distribution of the electric field obtained as inside the volume is not expected to be influenced that much (see later) by the tip length.

UV

For UV, because damping is very strong (small penetration depth compare to the size of the tip), only for very small apex radius (less than 30 nm), volume absorption is visible. But in general, only surface absorption will dominate with UV, as it shown for different apex radius in Figure 4.5 for different apex radius. Thus, during an atom probe experiment with UV, one sided energy absorption is expected to dominate.

Green

Three different radii are tested: 50 nm, 75 nm and 100 nm as shown in Figure 4.6. For 50 nm apex radius, comparable to the penetration depth in green (41 nm), electric field intensity is mainly located in volume as seen in Figure 4.6a.

For 75 nm apex radius, electric field intensity is located in volume and on the surface, although a larger part is made in volume as seen in Figure 4.6b. The maxima located at R=75nm and R=90 nm are not expected as the apex radius is almost twice the penetration depth. Maxima located deep inside the volume are also observed for the 50 nm apex radius figure 4.6a. The only possible origin is constructive interference that increase locally the electric field inside the volume. This will be explained in more details later in this chapter.

For 100 nm apex radius, most of the electric field is located near the surface, although electric field intensity in volume is still visible close to the apex as seen in Figure 4.6c. Thus, by varying the apex radius, for small apex radius, the electric field intensity is mainly located in volume, and no one sided absorption is expected from green. But for larger apex radius (above 75 nm), the electric field intensity in volume is reduced and is located more near the surface. Thus, when evaporating the tip with green, different behaviour are possible because

[2]FIB is usually the last step when making conical tip out of bulk material.

the distribution of electric field intensity evolves and absorption of energy is expected to be influenced.

IR

Three different radii are tested: 50 nm, 75 nm and 100 nm as shown in Figure 4.7. Because the penetration depth in IR is 315.2 nm, electric field intensity is present mainly in volume is present for every practical apex radius as expected. Maxima are present at specific radius. Note however that in Figure 4.7b, the maximum located at R=60 in Figure 4.7a has disappeared. Note also that there is almost no internal electric field inside the apex region for the 3 cases figure 4.7a, 4.7b and 4.7c. These 2 remarks show that there is a clear influence of the apex as it will be shown later in this chapter.

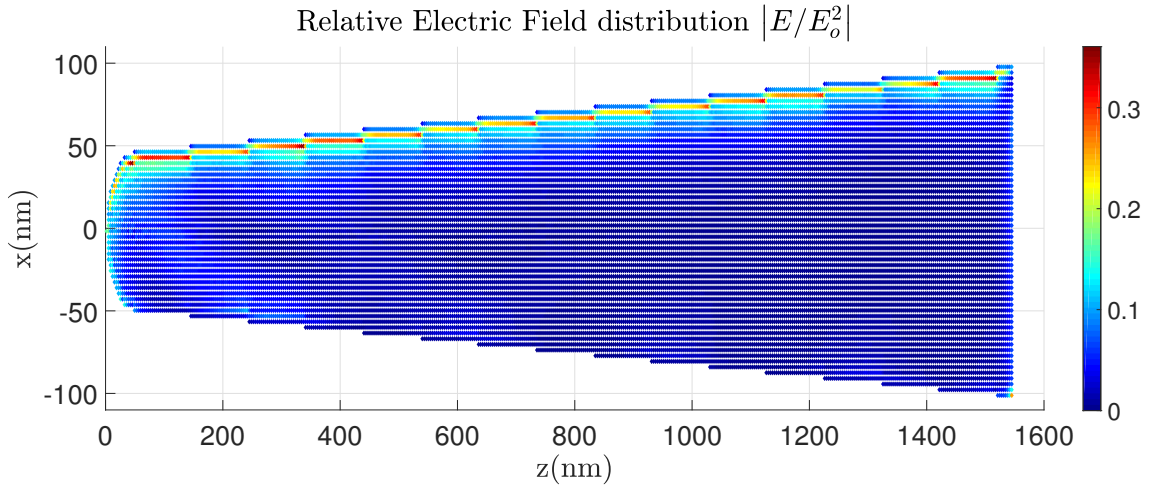

(a) R_{apex}=50nm .

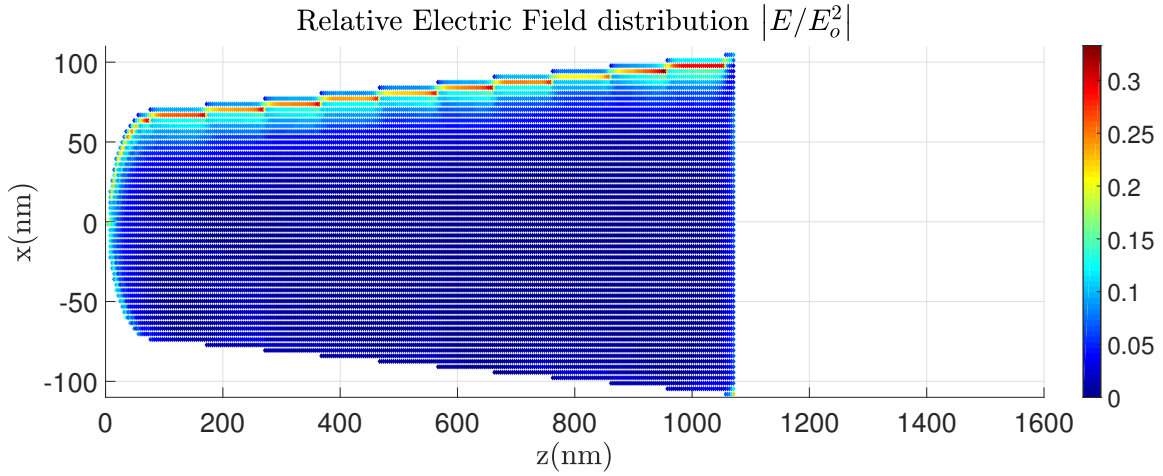

(b) R_{apex}=75nm.

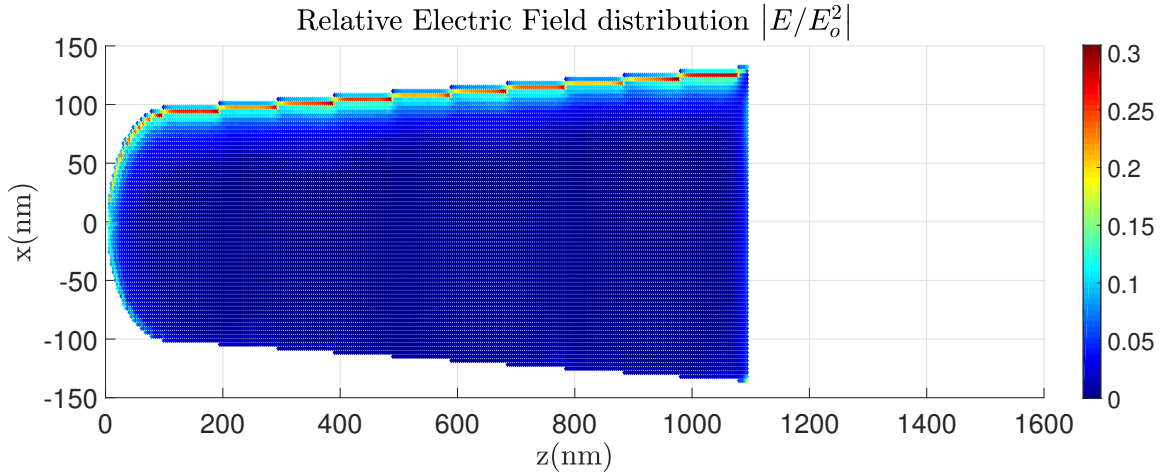

(c) R_{apex}=100nm.

Figure 4.5: ADDA simulations with InGaAs tip with UV illumination. Shank angle $\alpha = 2°$, Number of dpl=100. Apex radius (a)R_{apex}=50nm and length L=1.5μn; (b)R_{apex}=75nm and Length L=1μn; (c)R_{apex}=100nm and Length L=1μn.

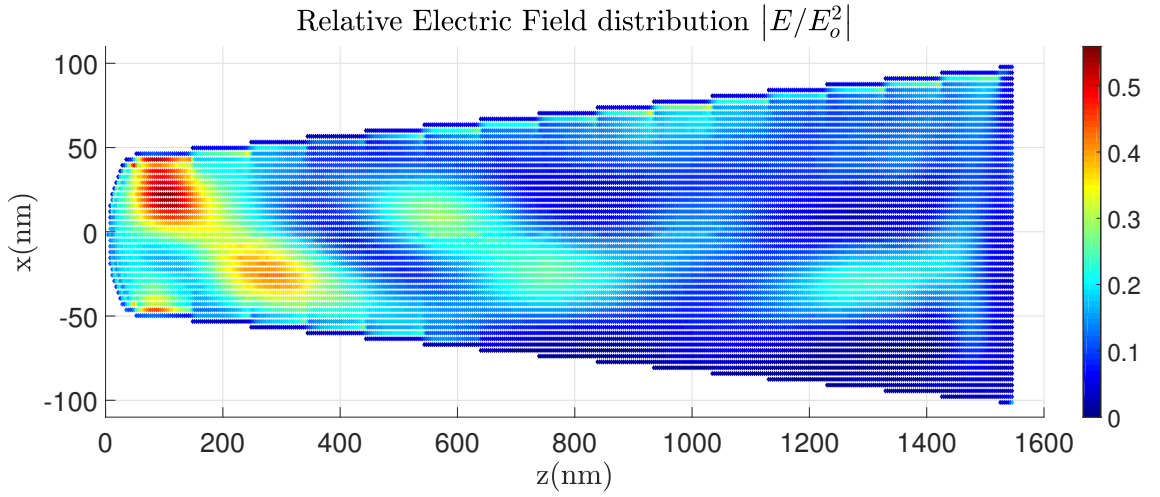

(a) R_{apex}=50nm.

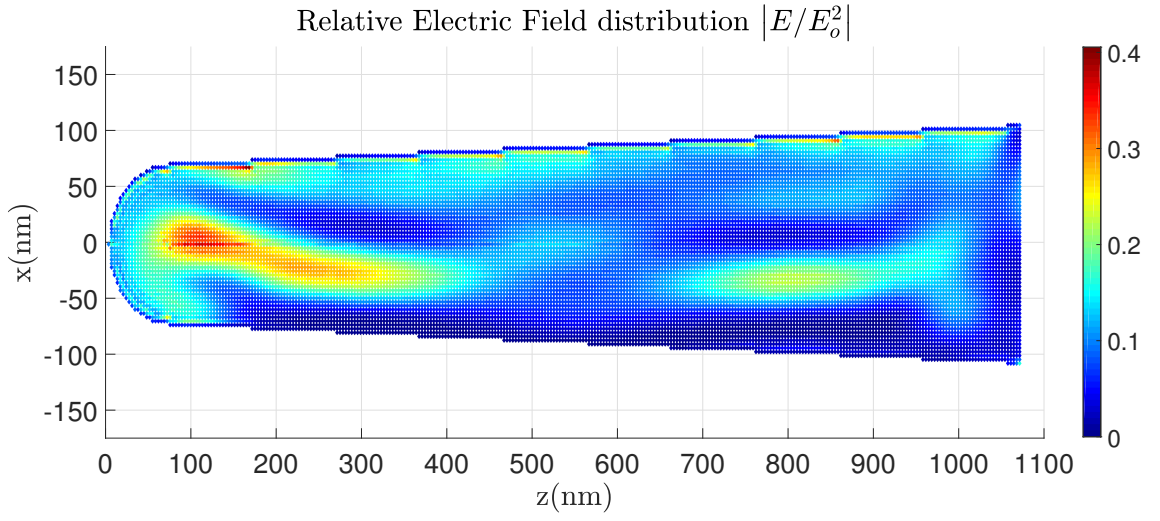

(b) R_{apex}=75nm.

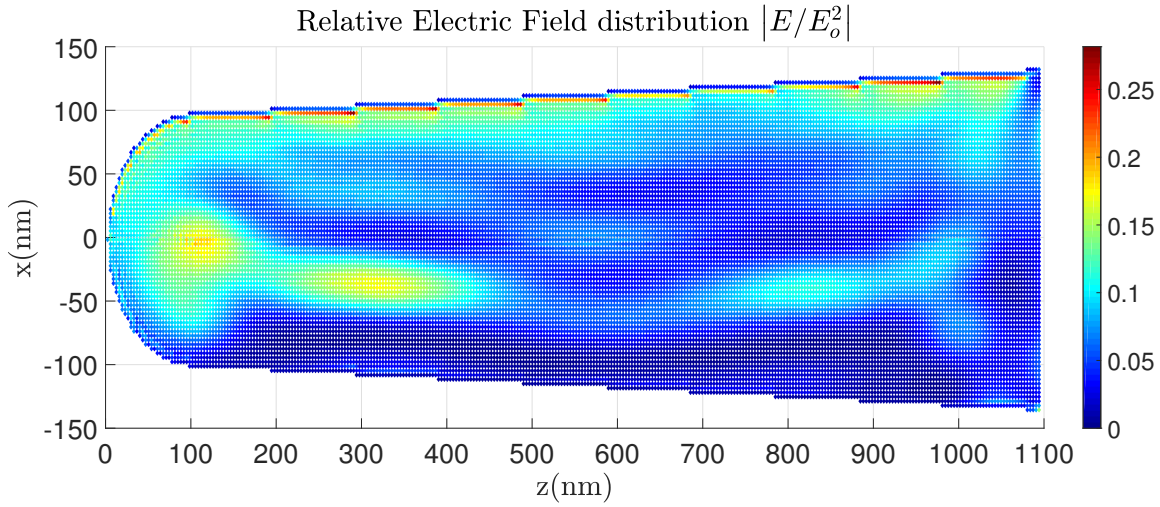

(c) R_{apex}=100nm.

Figure 4.6: ADDA simulations with InGaAs tip with green illumination. Shank angle $\alpha = 2°$, Number of dpl=150. Apex radius (a)R_{apex}=50nm and length L=1.5μn; (b)R_{apex}=75nm and Length L=1μn; (c)R_{apex}=100nm and Length L=1μn.

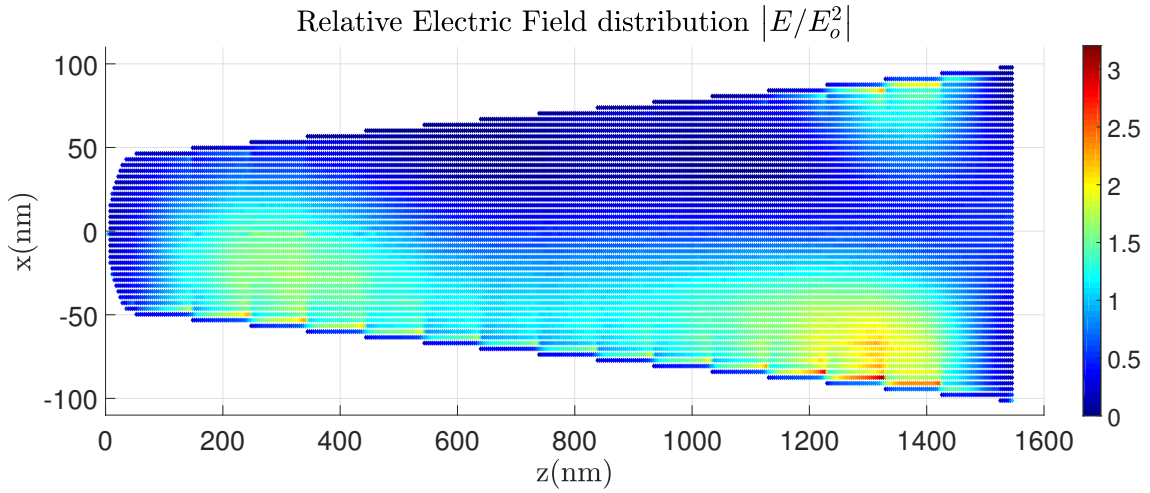

(a) R_{apex}=50nm.

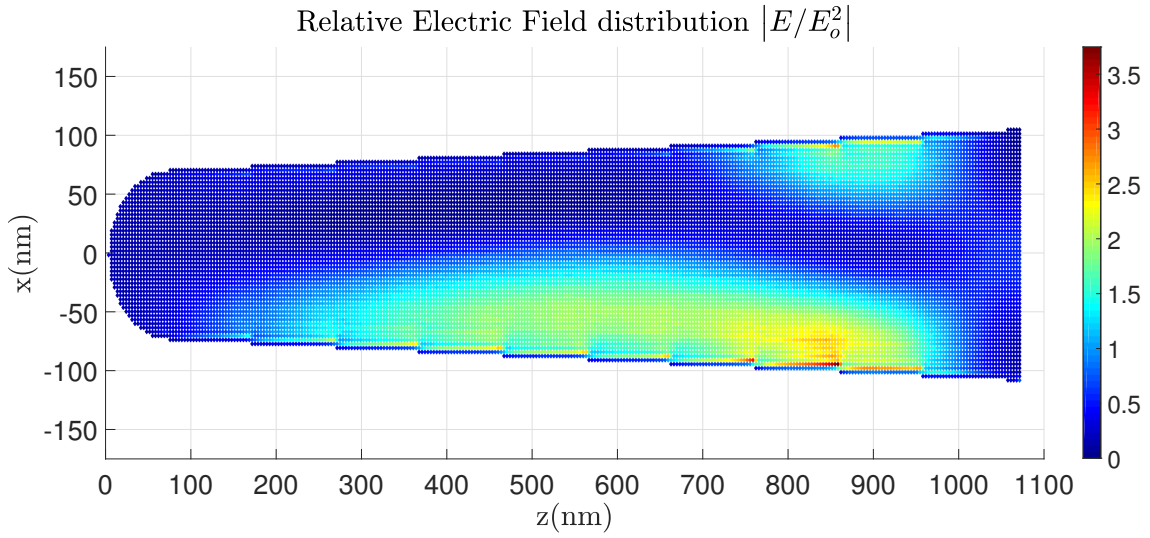

(b) R_{apex}=75nm.

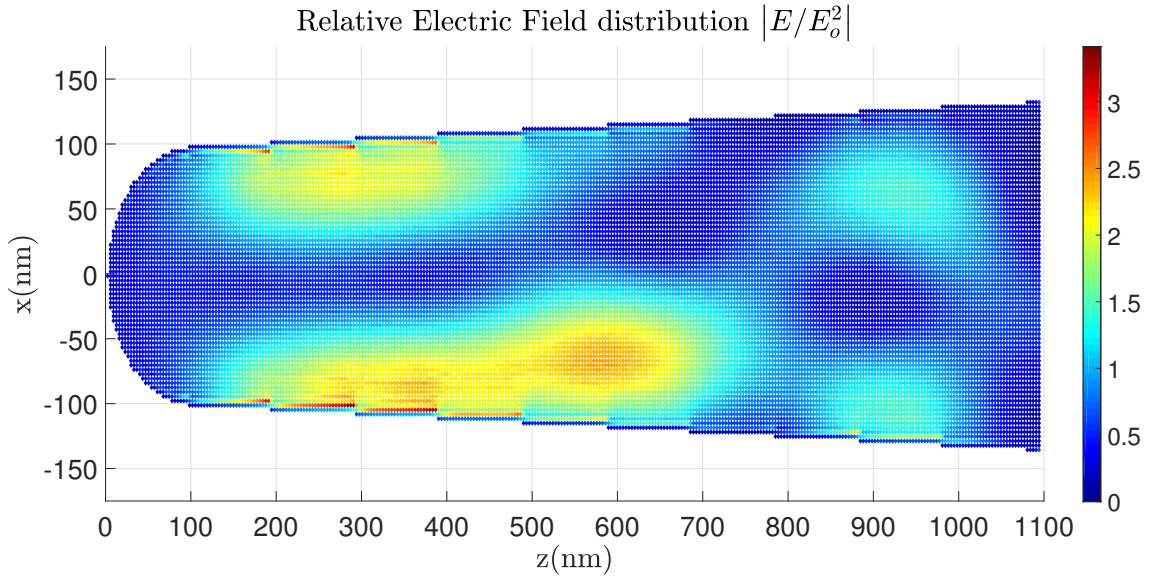

(c) R_{apex}=100nm.

Figure 4.7: ADDA simulations with InGaAs tip with IR illumination. Shank angle $\alpha = 2°$ and Number of dpl=300. Apex radius (a)R_{apex}=50nm and length L=1.5μn ; (b)R_{apex}=75nm and length L=1μn; (c)R_{apex}=100nm and length L=1μn.

4.2.3 Influences of the shank angle

We now look at the influence of the shank angle for each wavelength. When increasing the shank angle the length will be decreased, for the same reason as the apex radius.

UV

For UV, when changing the shank angle, the situation is remains unchanged between each case in Figure 4.8: The intensity of the internal electric field is located near the surface, and nothing penetrate in the volume of the tip. Shank angle does not influence the distribution of the internal electric field for UV.

Green

When increasing the shank angle from 2 to 4 ° (figure 4.9a to figure 4.9b), the positions of the maxima are located at the same radius (R=75nm and R=90 nm). When increasing the shank angle to 8°, the situation is similar to before, maxima are located at the same radius. Note however that for large radius (above R=100nm), no maxima are visible. This is simply explained by the fact that when the wave enters the tip at those large radius, the penetration depth is comparatively small to the distance the wave needs to travel inside the cross section. Thus, for large radius, the situation for green is similar to UV in term of distribution of the internal electric field

IR

When increasing the apex radius from 2 to 4 ° (figure 4.10a to figure 4.10b), the maxima for the 4° shank angle are located closer to the apex, but at still at the same local radius (R=60 and 90 nm) as the 2° shank angle figure 4.10a. The situation is similar for a shank angle of 8° as seen in Figure 4.10c.

However, it can also be observed that the maximun appearing at R=50nm in Figure 4.10a and 4.10b disappears in Figure 4.10c. Here it is clear that the apex must have influenced the internal electric field in this region, by creating destructive interference. By increasing the shank angle, the maxima are located closer to the which would explain why the maximum at R=50nm disappears for a shank angle of 8°.

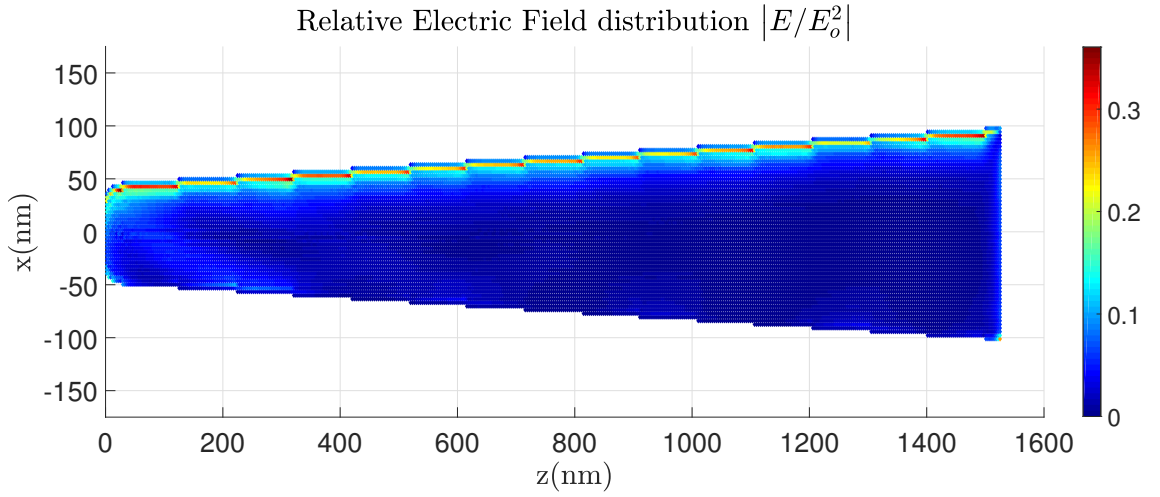

(a) $\alpha = 2°$.

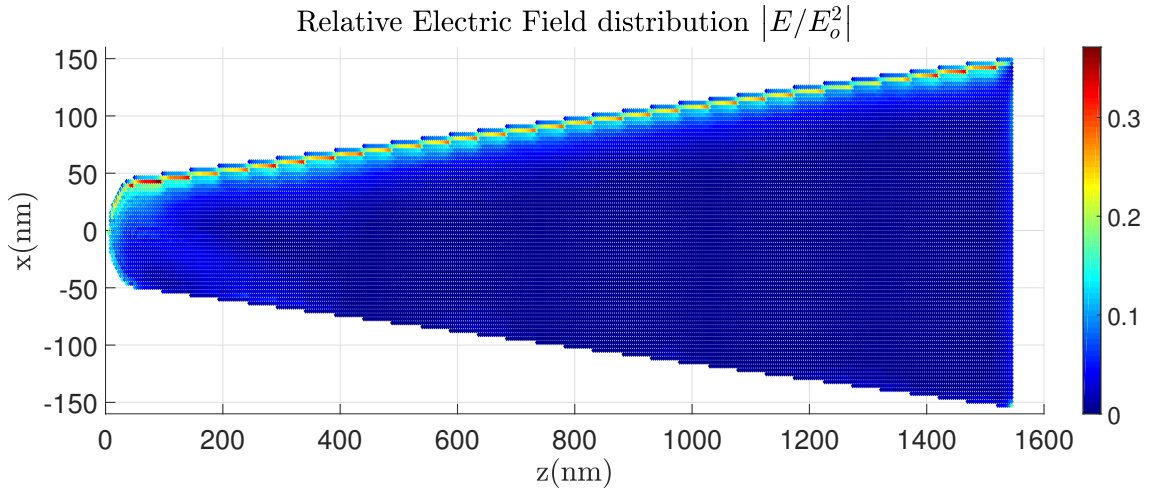

(b) $\alpha = 4°$.

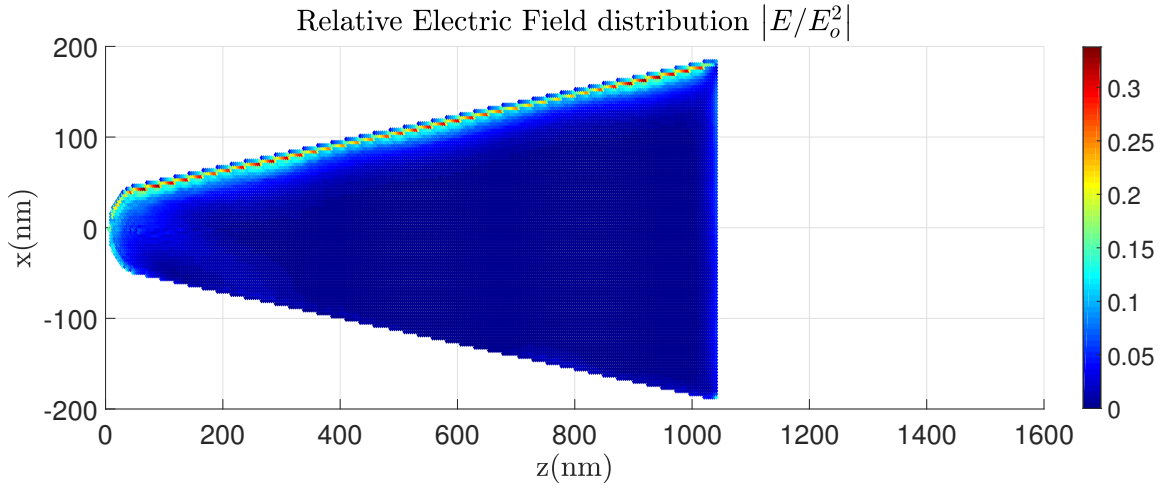

(c) $\alpha = 8°$.

Figure 4.8: ADDA simulations with InGaAs tip with UV illumination. Apex radius R_{apex}=50nm, Number of dpl=100. Shank angle (a)$\alpha = 2°$ and length L=1.5μn;(b)$\alpha = 4°$ and length L=1.5μn; (c)$\alpha = 8°$ and length L=1μn.

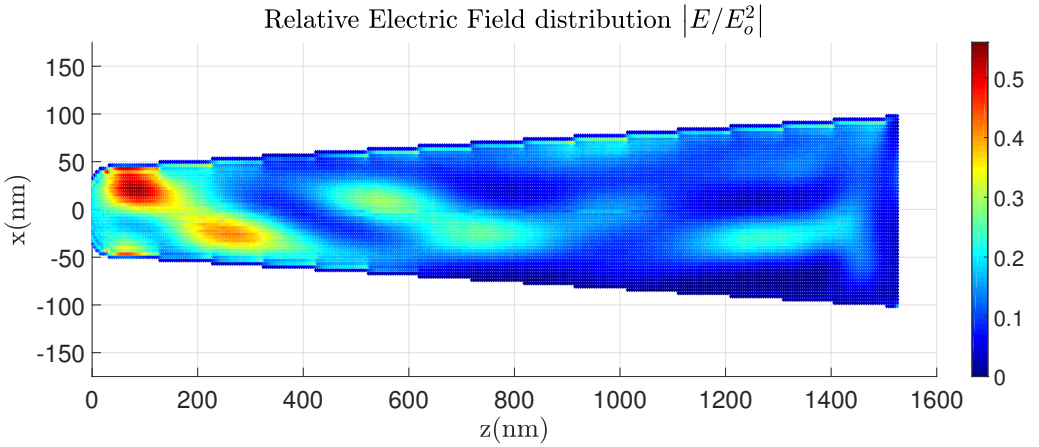

(a) $\alpha = 2°$.

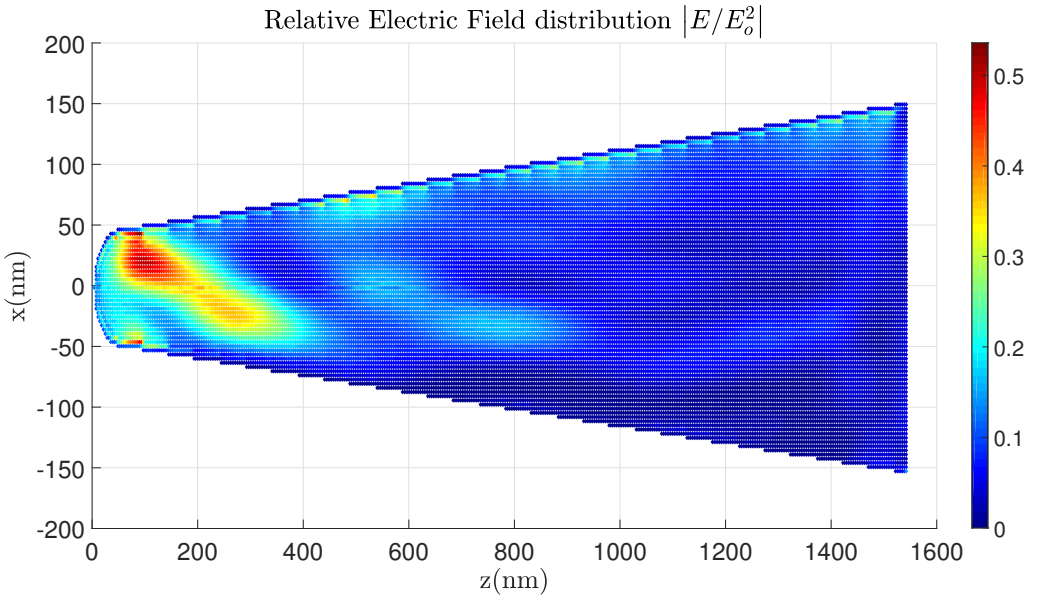

(b) $\alpha = 4°$.

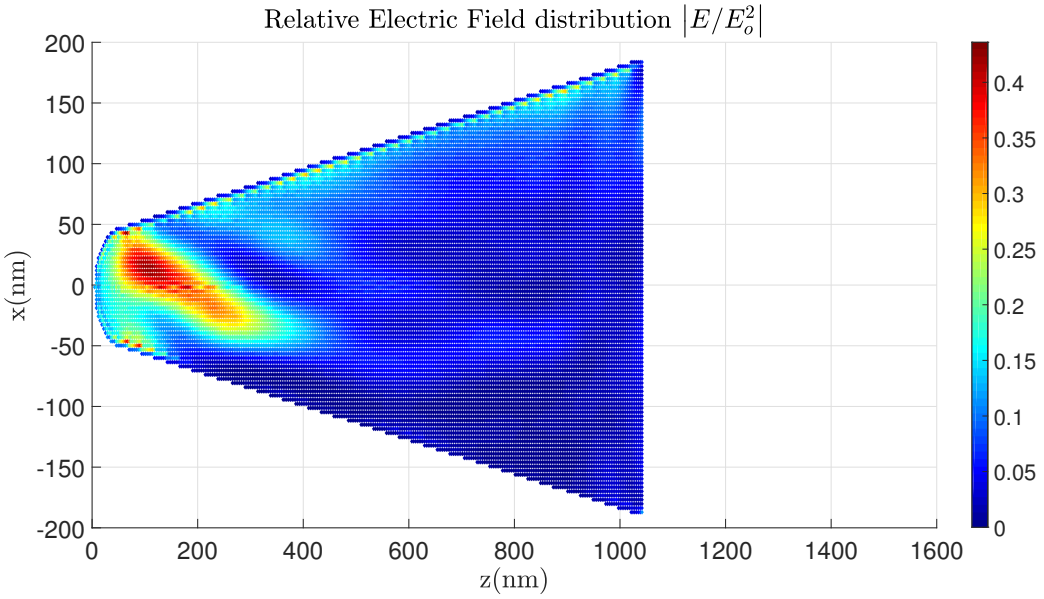

(c) $\alpha = 8°$.

Figure 4.9: ADDA simulations with InGaAs tip with green illumination. Apex radius R_{apex}=50nm, Number of dpl=150. Shank angle (a)$\alpha = 2°$ and length L=1.5μn;(b)$\alpha = 4°$ and length L=1.5μn; (c)$\alpha = 8°$ and length L=1μn.

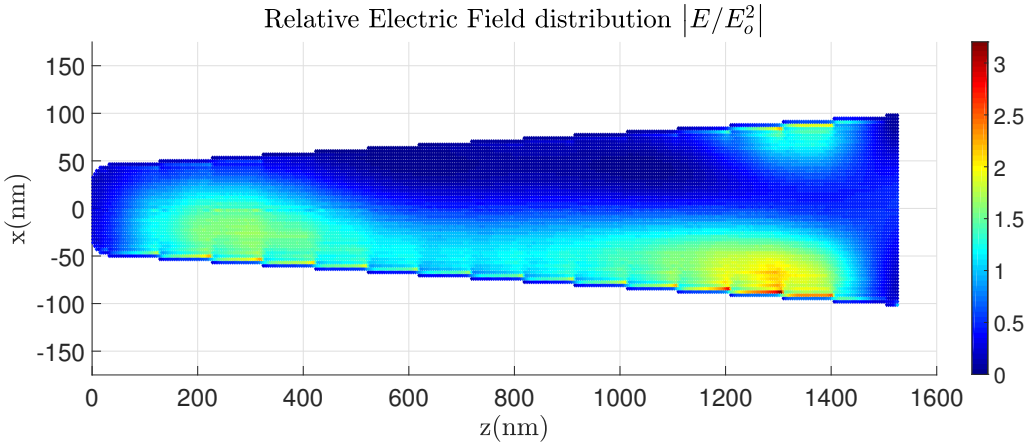

(a) $\alpha = 2°$.

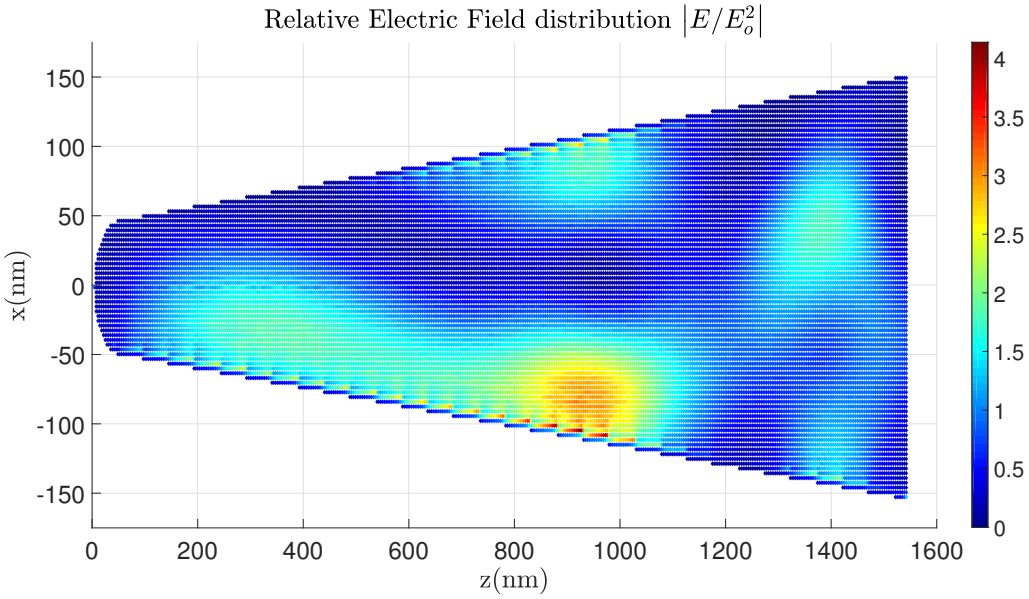

(b) $\alpha = 4°$.

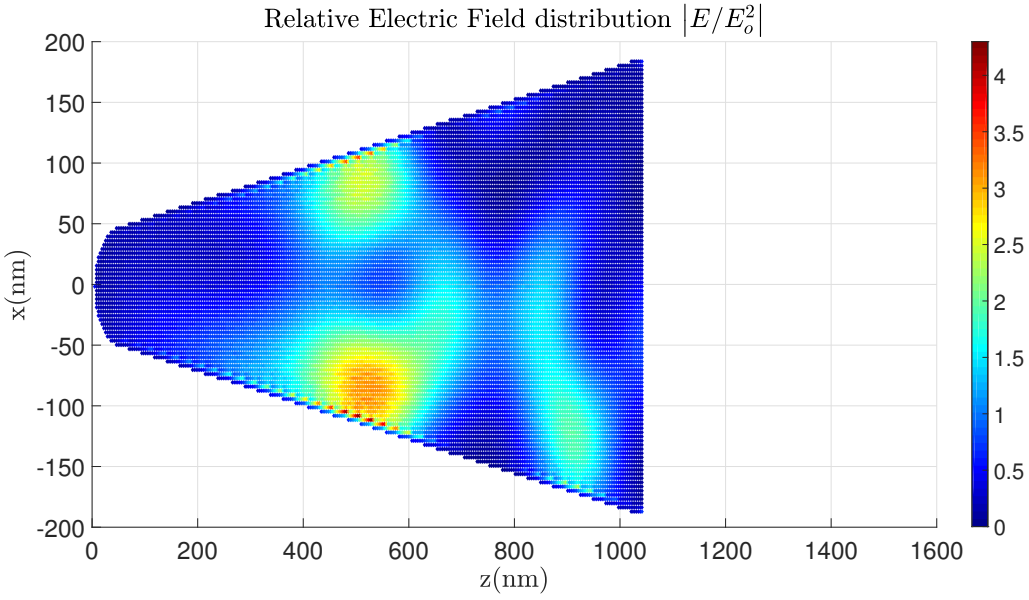

(c) $\alpha = 8°$.

Figure 4.10: ADDA simulations with InGaAs tip with IR illumination. Apex radius R_{apex}=50nm, Number of dpl=300. Shank angle (a)$\alpha = 2°$ and length L=1.5μn;(b)$\alpha = 4°$ and length L=1.5μn; (c)$\alpha = 8°$ and length L=1μn.

4.3 Understanding of light coupling in conical tip

In this section, we characterize the previous distribution map based on fundamental principles of light interference and coupling inside nano-scale volume with high aspect ratio using different level of geometrical refinement of increasing complexity. We first show an ADDA simulation for an InGaAs tip with 2° shank angle, 25 nm apex radius and 2.5μm long in Figure 4.12d with the results from different level of geometrical refinement figure 4.12a 4.12b and 4.12c and then explain each of these model.

The first model (figure 4.12a) is based on the analytical solution for the internal electrical field inside thin film and the tip is approximated as a stack of thin films as shown in Figure 4.11. The second model is based (figure 4.12b) on the analytical solution for the internal electrical field inside an infinitely long cylinder and the tip is approximated as a stack of cylinders as shown in Figure 4.11. The last model considered also the tip as stack of cylinder but takes into account the influence of the lateral interfaces.

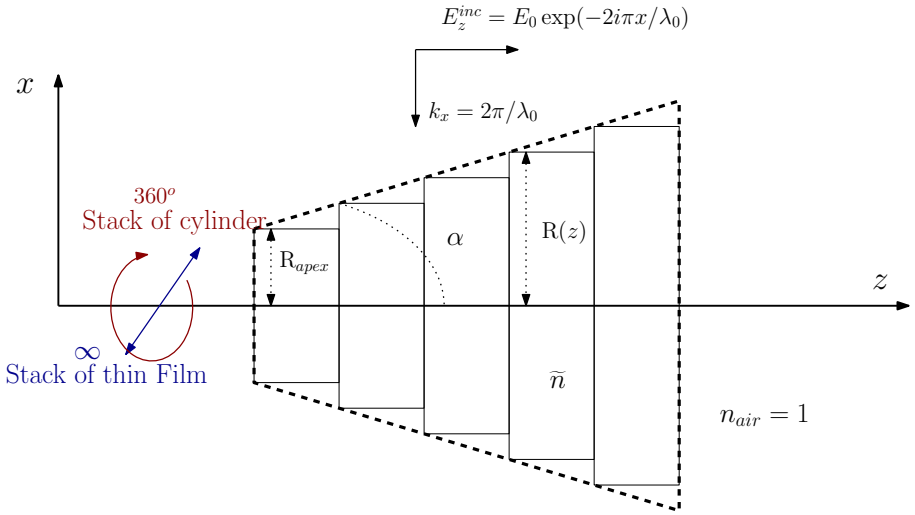

Figure 4.11: Representation of the actual tip with a stack of thin film (2D) and a stack of cylinder (3D).

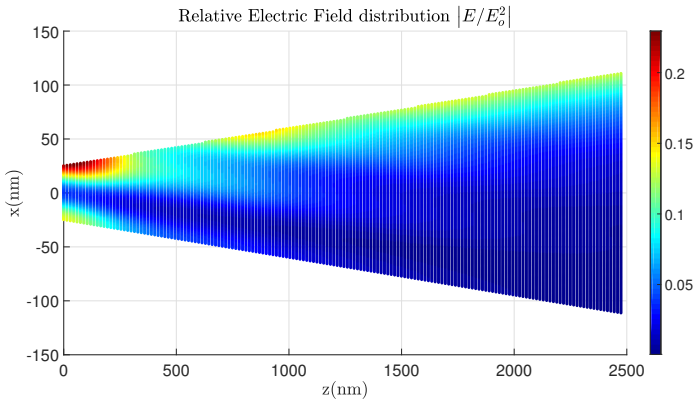

(a) Analytical solution for the stack of thin film model.

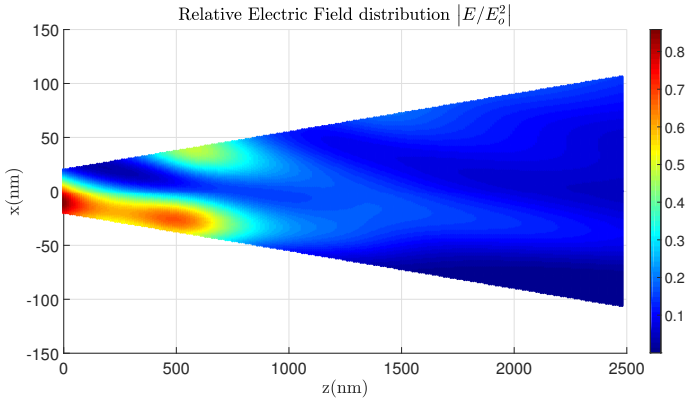

(b) Analytical solution for the stack of cylinder model.

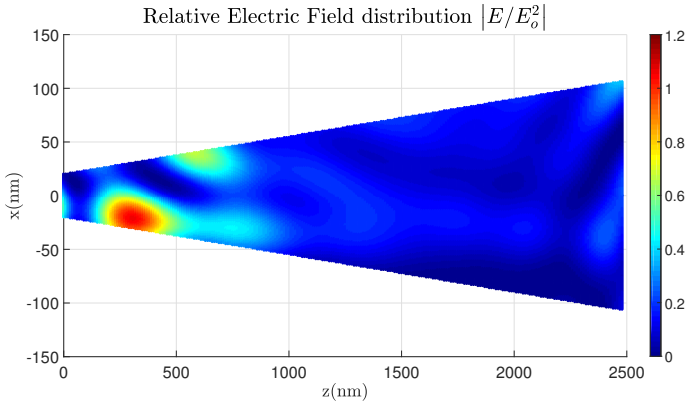

(c) Analytical solution for the stack cylinder model with the influence of the lateral interface.

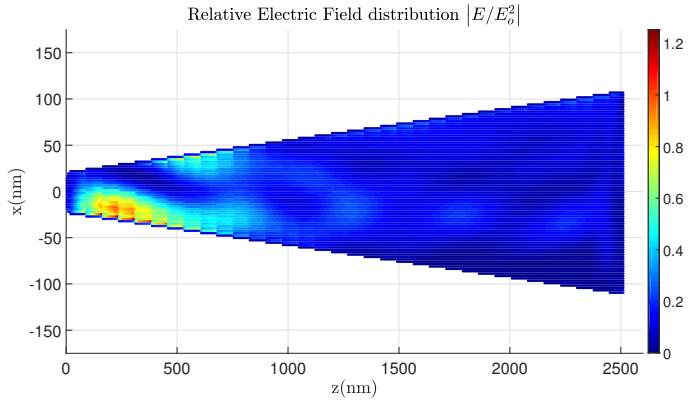

(d) ADDA numerical solution for conical tip. *dpl*=200.

Figure 4.12: Solution for a tip with R_{aapex} = 25nm, shank angle $\alpha = 2°$ and length L= 2.5μm.

4.3.1 Stack of thin film

As explained previously, maxima at specific radius can be observed when illuminating the tip with IR and green light. In fact, these are the results of constructive and destructive interference taking place inside the silicon tip. Indeed, this can be shown by simplifying the 3-dimensional conical tip geometry by a 2-dimensional stack of thin films [26] as shown in Figure 4.11. Despite being a crude approximation, an analytical solution can be obtained and offer an easy qualitative understanding.

We consider the tip-air interface as the origin of the phase and the thin film of height R(z). When the incident wave crosses the interface, it is only partly transmitted inside the film. After the transmission, the wave travelled inside the film and its intensity is partially damped following an exponential decrease. When reaching the bottom interface, part of the wave is transmitted in the air and is lost, and the other part is reflected back inside the tip. The reflected wave superposes with the incident wave and can interference. Taking into account the infinite reflections inside each film of height 2R(z), this gives

$$\begin{aligned} E_{z,int}(x) = E_0 \widetilde{t}_0^{\perp} \{ & \exp\left[-2i\pi\widetilde{n}(x - \mathrm{R}(z))/\lambda_0\right] \\ & + \widetilde{r}^{\perp} \exp\left[2i\pi\widetilde{n}(x + 3\mathrm{R}(z))/\lambda_0\right] \} \frac{1}{1 - (\widetilde{r}^{\perp})^2 \exp\left[8i\pi\widetilde{n}\mathrm{R}(z)/\lambda_0\right]}, \end{aligned} \tag{4.1}$$

where $\widetilde{t}_0^{\perp} = 2/(\widetilde{n}+1)$ is the normal incidence air-to-tip transmission coefficient and $\widetilde{r}^{\perp} = (\widetilde{n}-1)/(\widetilde{n}+1)$ is the normal incidence internal reflection coefficient. More details information about the derivation of (4.1) can be found in [26].

In this model, a constructive interference takes place when the reflected wave and the incident wave have the same phase. This happens when at some point inside the tip, the reflected wave has travelled a distance equal to a multiple of a wavelength has shown in Figure 4.13 i.e when the height of the thin film is $H = 2R_k(z) = k\lambda_0/(2n_r)$. Thus, for radius $\mathrm{R}_k = k\lambda_0/(4n_r)$, maxima are possible. The thin film approximation predicts a maximum for InGaAs at $R = 28$nm, which is observed in Figure 4.12a. In the ADDA simulation figure 4.12d, this maximum is also observed, but on the opposite side and for a slightly larger radius (R$\sim$ 35nm) compare to the maximum of the stack of thin film. The other predicted maxima are not visible in Figure 4.12a because their intensity is too low due to the high damping of InGaAs.

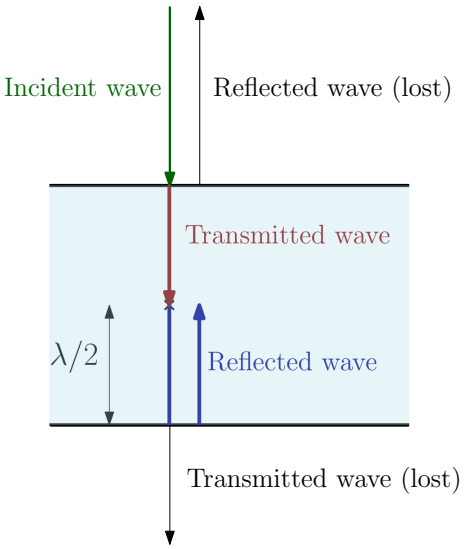

Figure 4.13: Representation of the condition to have a constructive interference. The incident wave (in red) interference constructively with the reflected wave (in blue) in this case.

Note that in this model, varying the shank angle does not modifies the radius at which the maxima appear. In case of a higher shank angle, the maxima will be closer between each other in the z direction. Indeed, the condition for constructive interference $\mathrm{R}_k = \lambda_0/(4n_r)$ can be rewritten in term of z as $z_k = (R_k - R_{apex})/\tan(\alpha) = (\frac{k\lambda_0}{4n_r} - R_{apex})/\tan(\alpha)$ and the interval is $\Delta z_k = (\frac{\lambda_0}{4n_r})/\tan(\alpha)$. This confirmed the changes observed in Figure 4.10 when varying the shank angle with IR.

In the thin-film approximation, we have neglected the tilted walls with respect to the propagation direction of the incident beam and the finite thickness of the tip. If we don't neglect the tilted, we then consider the tip as a truncated wedge. In this case, the incident beam normal to the axis of the wedge now leads to a non-zero propagation of the waves along the z direction. this extra power, significant for silicon tip as shown in [26], it not significant for InGaAs tip, as this extra propagation along the tip axis are quickly damped.

4.3.2 Stack of cylinder

A more complex level of geometrical refinement can be obtained by considering the tip as a stack of cylinder as shown in Figure 4.11. Then, we can use the analytical solution provided by the Mie theory for an infinitely long cylinder [13] (page 27). The analytical solution for this model is then

$$\begin{aligned} E_{z,int}(r,\theta,z) = E_0 \Bigg[& d_0\left(\frac{\mathrm{R}(z)}{\lambda_0}\right) J_0\left(\frac{2\pi\widetilde{n}r}{\lambda_0}\right) \\ & + \sum_{k=1}^{\infty} 2i^k d_k\left(\frac{\mathrm{R}(z)}{\lambda_0}\right) J_k\left(\frac{2\pi\widetilde{n}r}{\lambda_0}\right)\cos(k\theta)\Bigg], \end{aligned} \tag{4.2}$$

where the coefficients $d_k(\mathrm{R}(z)/\lambda_0)$ are determined by the boundary conditions at r=R(z) of the Maxwell's equations. The J_k is the k^{th}-order Bessel function of the first kind [7].

As it can be seen in Figure 4.12b, we recover the same behavior as the stack of thin film model. There are maxima at specific radius, which can now be interpreted as constructive interference. Compare to the stack of thin-film, these maxima are shifted to larger radius by approximately $\lambda_0/(8n_r)$. Thus, maxima are visible at $R_k = (2k+1)\lambda_0/(8n_r)$. For InGaAs, we then have maxima at R_1=14nm and R_2=43nm. In Figure 4.12b, 2 maxima are visible at R_1=25nm and R_2=43nm. The second maximum is expected, but still shifted compare to the maximum radius in ADDA (R$\sim$35nm). For the first one, this is on fact the end region of the maximum from R_1=14nm, which has a relative high intensity compare to the maximum at R_2=43nm, consequences of the strong damping of InGaAs.

Note that the electric field predicted by the stack of cylinder is one order of magnitude greater than the thin-film. This is a direct consequence of the confined geometry of a cylinder, which has an effect of focusing the intensity of the wave [26]. However, the maximal intensity from the stack of thin film is still smaller than the maximal intensity of the ADDA simulation.

The validity of this model required that the particle along the z direction must be smooth enough so that the coupling between each cylinder slab is negligible. Bogdanowicz et al. [24] experimentally showed evidence of these maxima by irradiating with high-fluence ($\sim$100 mJ^2/cm^2) IR laser conical tip in a LA-Apt tool. Although the coupling becomes important at the resonant radius and can violate the validity of the model, the resulting SEM image of the tip after the experiment showed apparition of sharp holes at specific radius indicating strong localized absorption, which was predicted by the analytic solution has shown in Figure 4.14.

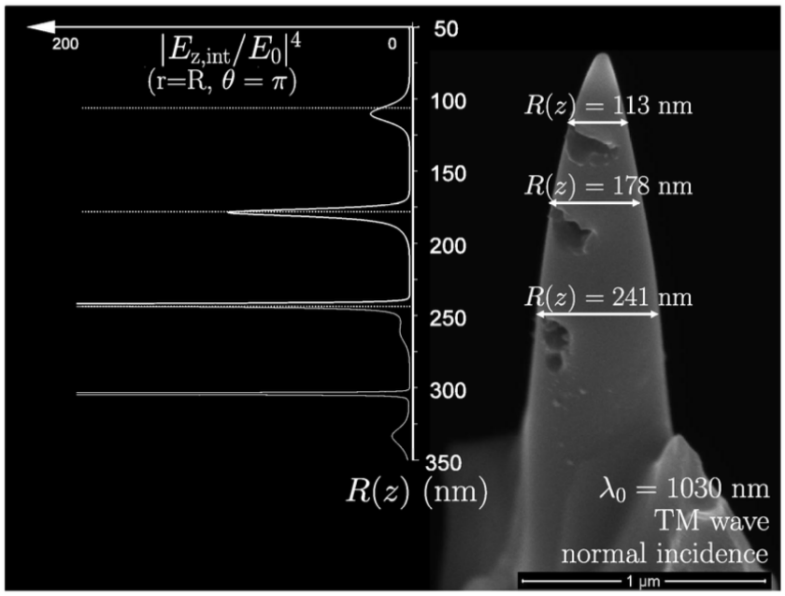

Figure 4.14: (left) 4th power of the internal electric field (∼ absorbed power in a dominant two photon absorption process.) from Mie theory along the illuminated side of an IR-irradiated silicon tip as a function of the local radius R(z).(rigth) Silicon tip illuminated by a high-fluence IR pulsed laser. Constructive interference occur at R(z)∼ 113,178 and 241nm. Reproduced from [24].

4.3.3 Apex coupling

The ADDA simulation actually considers the impacts of the apex and the base of the conical tip. The reason why the Mie solution seems to be unable to reproduce the results from ADDA simulations close to the apex for the InGaAs is because the analytical solution (4.2) used is based on the hypothesis of infinitely long cylinders and thus neglect the impact of the lateral interface (i.e. the apex). However, by comparing the internal field in the axial cut from the numerical simulation and from the Mie solution close to the apex, qualitative agreement (the intensity is different) is still present as shown in Figure 4.15. When looking at some distance from the apex (e.g: 1000nm), qualitative and quantitative agreement is present as seen in Figure 4.16.

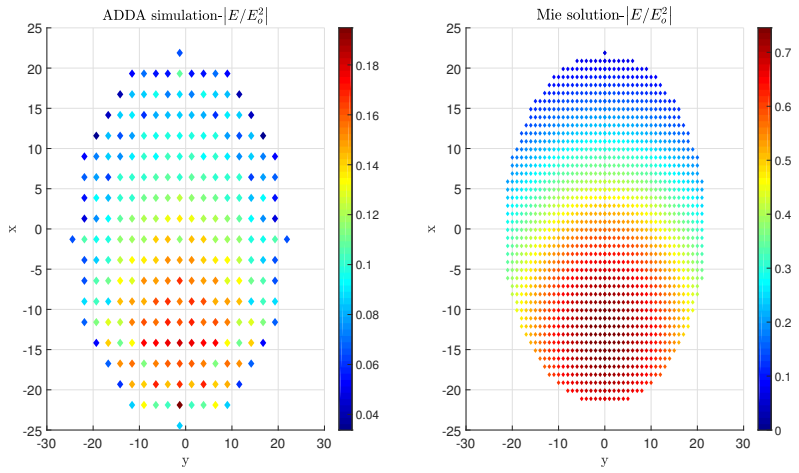

Figure 4.15: Comparison of the intensity of the internal electric field between (left) an axial cut at R=23nm for z=25nm of the ADDA simulation figure 4.12d and (right) Analytical Mie solution for R=23nm.

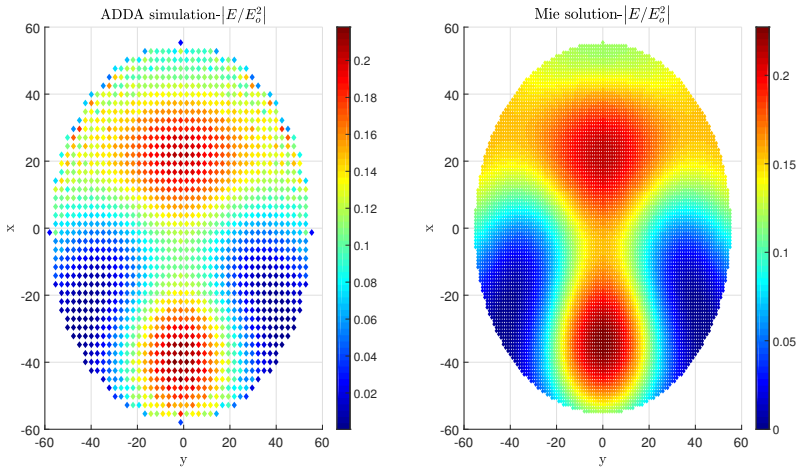

Figure 4.16: Comparison of the intensity of the internal electric field between (left) an axial cut at R=55nm for z=1000nm of the ADDA simulation figure 4.12d and (right) Analytical Mie solution for R=55nm.

From these observations, the Mie solution can be used almost everywhere inside the tips, at least to get a qualitative information on the distribution inside of internal electric field inside the tip. At some distance (see later in this section) from the apex, the quantitative behaviour is also recover by the Mie solution.

To see what the influence of the apex is, lets discuss an example from the literature [25]. In the case of a silicon tip with green light, it has been observed experimentally that the Mie solution (4.2) cannot match the apparition of periodic ripple close to the tip apex because their frequency along the tip axis is too high [25] as shown in Figure 4.17a.

In order to consider the possible influence of the apex, they look at how light can couple in the apex region and propagate inside the tip. Bogdanowicz et al. [25] shows that if a coupling with the apex and the incident wave exists, it can also propagate into the tip. To have an effective propagation of electric field from the apex along the tip axis, 2 conditions must be investigated. First, the electric field inside the apex region generated by the coupling with apex and the incident wave must be on the same order as the internal field given by the Mie solution. The second condition is that the conical tip must be able to guide away the electromagnetic power to have a significant absorption in the volume [25] (mode propagation).

In [25], they show that coupling is significant for a silicon tip with apex radius $R_{apex} = 50$ nm with green and only the HE_{11} mode is dominant. Provided some approximations, by superposing the analytical solution for the internal electric field in a dielectric cylindrical fibre of variable radius with the electric field predicted by the Mie solution, the apparition of periodic ripple close to the tip apex can be matched as shown in Figure 4.17b.

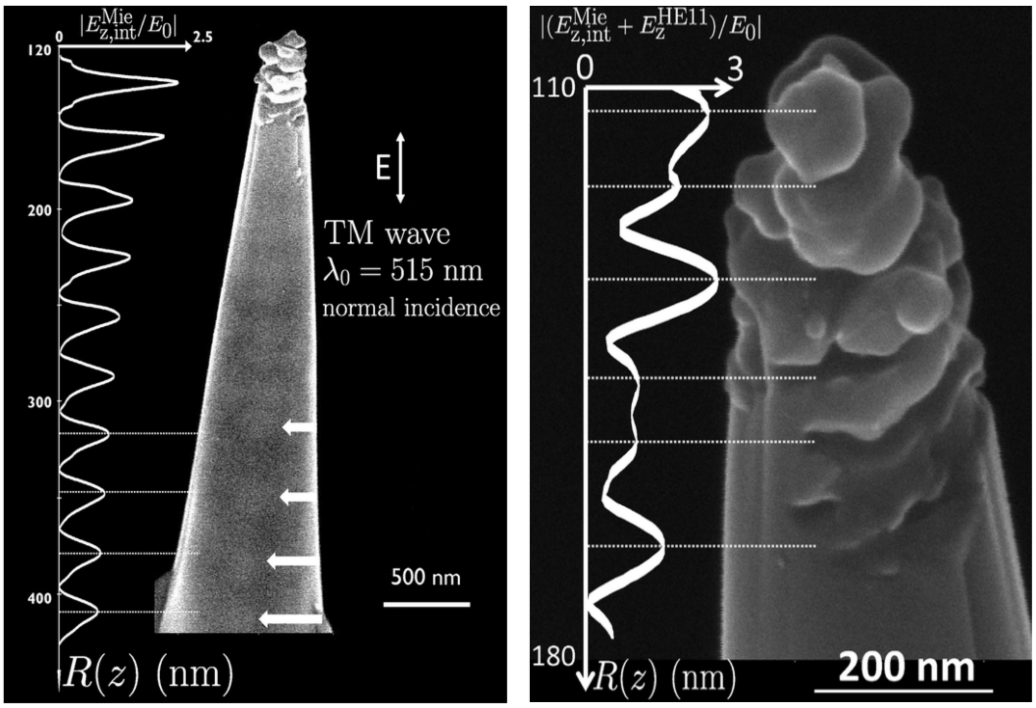

(a) (b)

Figure 4.17: (a) (left)Normalized Mie electric field along the illuminated side of a green-irradiated conical silicon tip as a function of the local radius R(z).(a) (right) SEM image of a silicon tip irradiated with a high-fluence (∼150 mJ/cm^2) green pulsed laser. (b) Amplitude of the interference between the Mie electric field and a mode (HE_{11}) from the apex . Reproduced from [25].

In order to use the model from [25], however, the analytical solution for an InGaAs dielectric cylindrical fiber must be known, which requires numerical methods and has not been done in this thesis. Instead, in order to keep the problem as simple as possible, we consider that a coupling exist between the apex of radius R=25nm and the incident wave and that a propagation is significant inside the conical tip. However, we neglect the actual shape of the mode propagating inside the cone, and consider simply the propagation of a plane wave from the apex superposed to the mie solution as shown in Figure 4.18. Thus the solution for the electric field becomes

$$E_{z,int}(r,\theta,z) = E_{z,int,mie} + E_0 \exp(-2i\pi(z+\lambda_0/2)\widetilde{n}_{test}/\lambda_0). \tag{4.3}$$

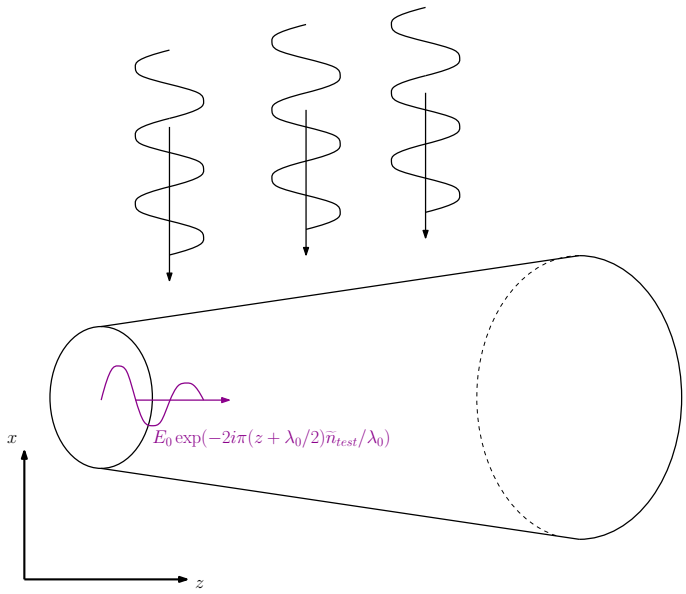

Figure 4.18: Representation of the mode coming from the apex which interferes with the internal electric field from the Mie solution (black). The mode is considered as a simple plane wave (purple) of wavelength λ_0 with complex refractive index $\widetilde{n}_{test}$. The complex part of the wave is there to model the decay of the mode along the axis.

Because the intensity of the "side" wave should decay as the local radius increases [25], we consider a complex refractive index $\widetilde{n}_{test}$ to represent the decay. Because this model is oversimplified, exact value of the refractive index $\widetilde{n}_{test}$ is hard to determine based on a mathematical development. Thus, one way to determine values for $\widetilde{n}_{test}$ is to consider a simpler case than the conical tip (e.g. a cylinder).

As shown in Figure 4.19, the simulation for a finite cylinder by ADDA shows periodic maxima along the tip axis, consequence of a cavity effect inside the cylinder. If we take the Mie solution for an infinite cylinder, by adding the "side" waves and adjusting the value of $\widetilde{n}_{test}$ to get a good qualitative and quantitative agreement between analytical and numerical results as shown in Figure 4.20, a value for $\widetilde{n}_{test}$ can be determined. It is found that for a cylinder with radius 30nm and length 1.5μm, $\widetilde{n}_{test} = 1.15 + 0.2i$ fits the best. However, this method is empirical, as we totally neglect the actual conical shape of the tip, and thus we neglect the coupling existing between each cross section.

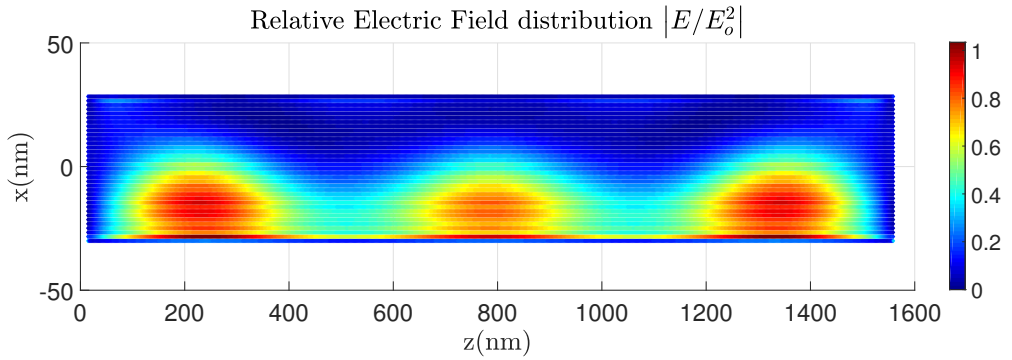

Figure 4.19: Transversal cut of the internal electric field in a cylinder (length L=1.5μm and $R_{apex} = 30$nm) illuminated with green light ncident on the top of the cylinder. Simulated with ADDA.

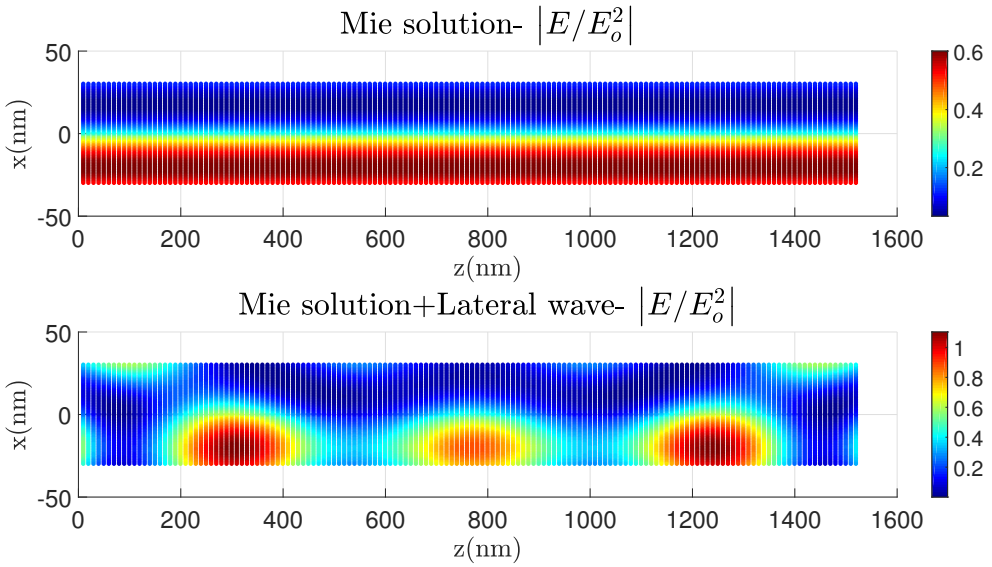

Figure 4.20: Transversal cut of the internal electric field in a cylinder (length L=1.5μm and $R_{apex} = 30$nm) illuminated with green light incident on the top of the cylinder. (up) Mie solution for an infinite cylinder. (down) Mie solution for an infinite cylinder superposed with a plane wave of refractive index $\widetilde{n}_{test} = 1.15 + 0.2i$ coming from each lateral interface.

Comparison between figure 4.12c and 4.12d shows a better agreement in the distribution of the internal electric field than with only the mie solution figure 4.12b. The maximum at R$\sim$35nm is correctly recovered. We can see that the maximum at R=25nm in Figure 4.12b has "disappeared" and that the electric field is very low to the apex surface, which is observed in Figure 4.12d. What is more, the maximal intensity from the model is now closer to the intensity obtained in the ADDA simulation. Thus, this shows that a coupling between the apex and the incident wave is present.

We can now look back at the axial cut from figure 4.15 and 4.16, but this time we add the lateral wave from the apex. For the axial cut close to the apex, as seen in Figure 4.21, a better quantitative agreement is made between the numerical solution and the model. For the axial at z=1000nm in Figure 4.22, addition of the lateral wave is almost unnoticed, which is logical since the penetration depth of this lateral wave is 204 nm, except near the top, where the intensity is slightly higher than in 4.16. This change is due to the simplified shape of the actual lateral mode. For example, the first mode HE_{11} can be approximate with a Gaussian shape [8]. Thus, the influence of the mode decreases near the surface. To get the distance from the apex where the lateral wave can be neglected and only the Mie solution remains, we can take the penetration depth based on the empirical refractive index.

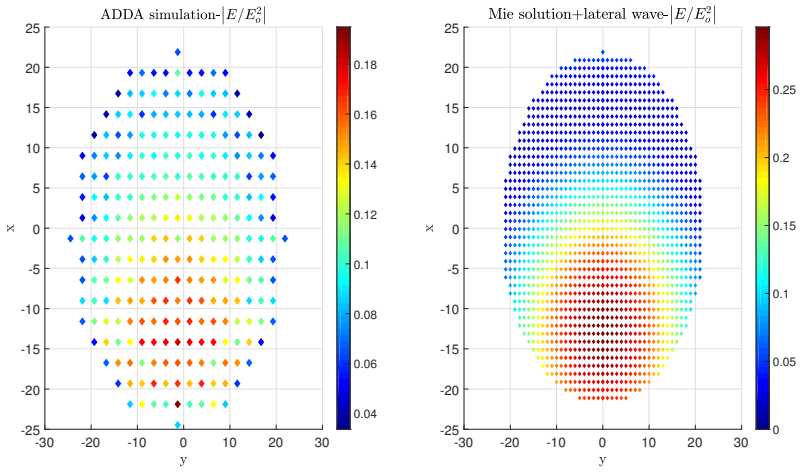

Figure 4.21: Comparison of the intensity of the internal electric field between (left) an axial cut at R=23nm for z=25nm of the ADDA simulation figure 4.12d and (right) Analytical Mie solution for R=23nm with a lateral wave.

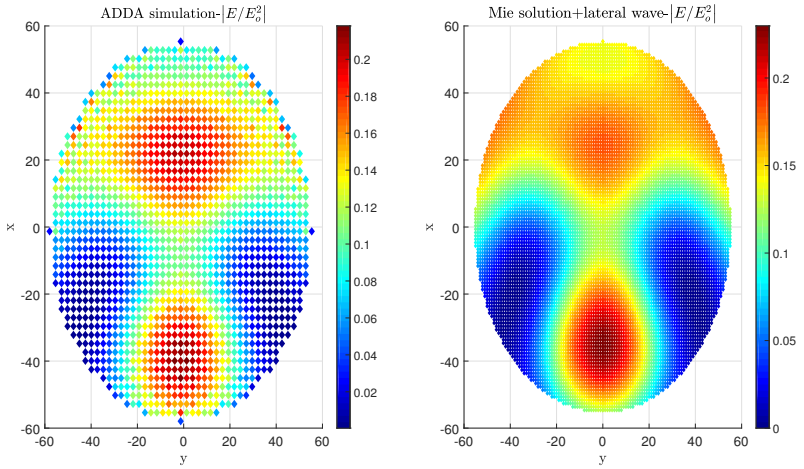

Figure 4.22: Comparison of the intensity of the internal electric field between (left) an axial cut at R=55nm for z=1000nm of the ADDA simulation figure 4.12d and (right) Analytical Mie solution for R=55nm with a lateral wave.

4.4 Conclusion

In this chapter, we have described and analysed the absorption map of InGaAs tip using numerical results simulated with ADDA. Three different wavelengths have been tested:UV, green and IR with different apex radius and shank angle.

The distribution of the electric field inside the tip UV is mainly located near the surface on the laser side at all practical tip's dimension and can thus lead to one sided absorption. For IR, on the other hand, the distribution is mainly in volume with maxima located at specific radius. The last wavelength, green, is intermediate between UV and IR. Depending on the apex radius, electric field can be either located in volume for apex radius of size comparable to the penetration depth, of either in surface for large radius ($R_{apex} \geq 2\delta_{green}$). Thus, for IR and green, energy is expected to be absorbed mainly in volume

When analysing IR and green, the distribution maps show maxima at specific radius inside the volume. The origin of these maxima is constructive interference between the reflections

taking place inside tip. Using different level of geometric refinement, it can be shown that these maxima are located at specific radius given by $R_k = (2k + 1)\lambda_0/(8n_r)$ using the Mie solution. The Mie solution can be used to predict the distribution inside the volume of the tip except close to the apex, where propagating waves created by a coupling between the apex and the incident wave can be significant. The exact distance from the apex where the Mie solution can be used without being perturbed by the apex wave depends on the geometry and the wavelength, which could be determined by a more detailed analysis than presented in this thesis.

Chapter 5

Apex temperature evolution

In Chapter 2 we have shown that if we can assume the field evaporation to be a thermally activated process, then the number of detected hit per pulse is temperature dependant. In chapter 3, we have shown that the slow decreasing observed in the TOF spectra for silicon can be correlated with the temperature evolution of the apex. The difference in mass resolution between IR, UV and green is then a direct consequence of the absorbed energy distribution of silicon at each wavelength.

In this chapter, we investigate the temperature evolution of the apex for InGaAs tip. We first proposed a thermal model considering the different time scale involved. Then, based on the distribution of internal electric field obtained in chapter 4, we analysed the temperature evolution and compare it to the TOF spectra of InGaAs shown in chapter 3.

5.1 Thermal model

In this section, we present the thermal model commonly used to study the thermal evolution of silicon tips. We then transpose this model for InGaAs tips and simplified it considering the characteristic of InGaAs. In chapter 3 we have shown that the cooling times associated the TOF spectra of silicon figure 3.1 are on the order of a few nanoseconds. For InGaAs, the slow decreasing was also on the order of a few nanoseconds. Thus, the times scale of the apex cooling for InGaAs is expected to be on the order of a few nanoseconds.

5.1.1 Uncoupling of the full problem

In section 2.1.4 in chapter 2, we have described the interaction between a 500 fs pulse laser and a semiconductor and the time scales associated with the different phenomena taking place inside the semiconductors (figure 2.8). By comparing the different time scales, the carrier excitation (taking place during the pulse$\sim$500fs) and the thermalization (a few picoseconds) are much faster than the carrier diffusion/ recombination (from 10^{-11} to 10^{-8}) and the thermal diffusion (expected on the order of a few nanoseconds). The former processes can be considered as instantaneous processes regarding the latter processes.

Thus, the thermal diffusion and the carrier diffusion/recombination will be assumed as uncoupled from the others effects. Doing so, we can consider separately the process of energy absorption resulting from the complex interaction between the laser and the semiconductor, from the diffusive process.

Regarding the time scale of the diffusive process, the laser pulse instantly creates a distribution of excess carriers inside the tip. The excess carriers rapidly thermalize to the band edge and heat the sample to give it an initial temperature. During the thermalization process, the

carriers are usually assumed to be fixed because of their slow diffusion coefficient (justified a posteriori)[6][40]. Then the thermal and carrier diffusion with recombination processes start. Because recombination can transfer energy to the lattice, the temperature evolution can be influenced by both the thermal and carrier diffusion. Thus, in order to estimate the temperature, we should solve a system of coupled equations describing the evolution of free carriers and temperature.

In this thesis, in order to get a first approximation of the temperature evolution, we will simplify this coupled problem by simply considering the temperature evolution to be influenced by heat diffusion. We thus neglect the diffusion and recombination of the excess carriers.

The reason for this apparent crude simplification is explained further by looking at the different times scale for InGaAs and carrier diffusion and the type of recombination for InGaAs. We first explain what is the model commonly used for silicon to evaluate the diffusion of carriers in the coupled thermal and carrier diffusion problem just below. Because InGaAs is a direct band gap semiconductor, the main recombination process might be different than for silicon, which is an indirect band gap semiconductor.

5.1.2 Thermal-carrier diffusion/Recombination

We consider the situation of a tip in vacuum attached by its base to a large proof mass of constant temperature T_{base} (Heat reservoir), illuminated by a 500 fs laser pulse of power P_{laser}, wavelength λ, spot radius R_{spot} and repetition rate f_{rep}. Before the laser pulse is sent, the whole tip is at its base temperature. As soon one pulse laser is sent (t=0), thermal and carriers diffuse start (uncoupled hypothesis).

Carrier diffusion/Recombination

After the thermalization process, the free carriers have a Maxwell's Boltzmann distribution and evolve following a drift-diffusion model. It is, however, usually assumed that the electric field is screened inside the volume of the tip within a few picoseconds after the pulse, thus the drift can be neglected [6]. Combining the time evolution equations for holes and electrons, the ambipolar diffusion[1] formulation can be used to describe the global evolution of the free carriers,

$$\partial_t n = G - R + \nabla \cdot (D_a \nabla n), \tag{5.1}$$

where G is the generation rate of carriers, R the recombination rate of carriers, n is the excess carriers concentration and D_a the ambipolar carrier diffusion coefficient. The generation term is only present during the laser pulse and disappears when the carrier diffusion starts, so $G = 0$. The recombination rate depend en the level of carrier injection and the material.

For silicon, a high injection level is usually supposed and Auger recombination[2] is the dominant effect. Thus in the approximation of auger recombination, $R = R_A = C_A n^3$, with C_A the auger recombination coefficient equal to $10^{-31}\text{cm}^6/\text{s}$ for silicon [6].

For InGaAs, the carrier lifetime and thus the recombination process, depend on the doping level [35]. For undoped to low doping ($<10^{15}\text{cm}^{-3}$), Shockley–Read–Hall recombination dominates. In the doping range from 10^{16} to 10^{18} cm^{-3}, radiative recombination is the dominant

[1] An ambipolar diffusion for a semiconductor is the diffusion of an electron and a hole which move together

[2] Auger recombination is a non-radiative process in which the energy from the recombination of an electron and a hole is directly given up to an electron in the conduction band instead of generating a photon of energy E_{gap}. This electron then thermalizes back down to the conduction band edge, transferring its energy to the lattice.

mechanism. For higher doping level, Auger recombination dominates ($C_A = (C_e + C_h)$, with $C_e = 5 \times 10^{-30}\text{cm}^6/\text{s}$ and $C_h = 7 \times 10^{-29}\text{cm}^6/\text{s}$ for InGaAs [43]). Practically, the InGaAs tip used in this thesis have a low doping of $n < 1e16\text{cm}^{-3}$ [3]. In this thesis, we can consider the radiative recombination to be dominant for the InGaAs, and $R = R_R = B_R n^2$, with $B_R = 1.43 \times 10^{-10}\text{cm}^{-3}\text{s}^{-1}$.

Concerning ambipolar carrier diffusion coefficient, its value depends on the concentration of excess carrier and on the temperature [18]. However, it is considered as constant in (5.1) for simplicity[23][40]. The value for the silicon is $18\text{cm}^2/\text{s}$ [40] and $22\text{cm}^2/\text{s}$ for the InGaAs [37].

In order to get the initial distribution of excess carrier n_{init}, we should consider the exact interaction between the laser and the semiconductor. However, the exact electronic processes taking place inside the material are complex to model in practice. Thus, as it has been done in chapter 4, we assume that a complex refractive index depending on the wavelength can represent the electronic processes taking place inside the material. The absorbed energy u_{abs} can be then be computed using eq. B.11 (see appendix B). From the absorbed energy, we can compute n_{init}, as in [6], considering only interband absorption of the laser is considered,

$$n_{init}(x, y, z) = \frac{u_{abs}(x, y, z)}{h\nu}, \tag{5.2}$$

where $u_{abs}(x, y, z)$ is the absorbed energy per unit volume for one pulse, $h\nu$ is the photon energy at the wavelength of the pulse laser. During the diffusion, no carriers escape from the surface of the tip neither go through the base of the tip. Thus, we have $\nabla n \cdot \mathbf{n} = 0$ at the surface of the tip.

Heat Diffusion

Now considering the heat diffusion inside the volume, a simple diffusion equation is considered,

$$\rho C_p \partial_t T + \nabla \cdot (-k \nabla T) = Q, \tag{5.3}$$

where ρ is the density of the material, C_p the heat capacity at constant pressure, k the thermal conductivity, T the temperature and Q the heat generation rate from recombination. Because the tip will cool from its maximal temperature (usually measured 300K in the lab) to its base temperature ($\sim$20-30K), temperature dependence of the thermal properties must be considered. Their values for silicon and InGaAs can be found in appendix A.

Heat generation rate Q depend on the type of recombination. For Auger recombination, the process leads to transfer of energy to the lattice, thus it needs to be considered in the thermal evolution temperature,

$$Q = E_{gap} R_a = E_{gap} C_A n^3. \tag{5.4}$$

For radiative recombination, each recombination release a photon of energy E_{gap}. In order to keep think simple, we can first consider that this energy is not transferred into heat to the lattice, but is lost, so $Q = 0$.

We assume that there is no convection (vacuum) neither radiation at the surface of the tip, and that heat is transferred by conduction to the heat reservoir at constant temperature. Thus, $\nabla T \cdot \mathbf{n} = 0$ at the surface of the tip, and $T = T_{base}$ at the base of the tip. The initial temperature

[3] Actually, the top 100 nm is p doped ($\sim$2e19cm^{-3}). The rest (1 μ m of i-InGaAs) has a low doping of n$<$1e16cm^{-3}. Although the top 100 nm of the InGaAs is p doped, there is very less probability that it is saved during sample preparation.

distribution T_0 can be computed by conservation of energy. Using thermodynamics, the energy released by thermalization heats the sample from T_{base} to T_0,

$$\int_{T_{base}}^{T_0} \rho C_p dT = n_{init}(x,y,z)(h\nu - E_{gap}), \tag{5.5}$$

where $(h\nu - E_{gap})$ represents the energy released by the scattering of the electron to the band edge. Note that in (5.5), the distribution of $n_{init}(x,y,z)$ is assumed unchanged during the thermalization process and all the carrier are assumed to relax to the band edge. This causes a slight over estimation of the actual temperature. By solving simultaneously (5.1) and (5.3), the temperature at the apex can be computed. Note that for InGaAs,(5.1) and (5.3) are actually uncoupled. Thus, there is actually no need in solving (5.1). The excess carriers are still taken into account through (5.5), but their evolution doesn't influence the temperature for InGaAs.

5.1.3 Orders of magnitude

Without solving (5.1) and (5.3), estimation of the different time and length scales can still be obtained. In any diffusive process, the characteristic time scale of the problem can be estimated with

$$\tau \sim \frac{L^2}{D}, \tag{5.6}$$

where D is the diffusive coefficient and τ the characteristic time scale of the problem over the distance L. The diffusive coefficient for the carrier evolution is explicitly given in (5.1). Note that during the thermalization (few pico-seconds), we assume that the initial distribution of excess carriers was fixed. We can estimate the characteristic length travelled by the carrier during a pico-second for silicon and InGaAs respectively. $L_{thermalization} \sim \sqrt{18 \times 10^{-4} \times 10^{-12}} \sim 42 \times 10^{-9}$m= 42nm and $L_{thermalization} \sim 47$nm, which is assumed as negligible in [6][40]. We will also assume the same here for simplicity of calculation, although this assumption is not really justified since the dimension of the apex are on the same order as these diffusion length.

The thermal diffusivity is defined as

$$D_t = \frac{k}{\rho C_p}, \tag{5.7}$$

which is temperature dependant. Some value for silicon and InGaAs at different temperature are shown in Table 5.1.1. As it can be seen, the thermal diffusion coefficient of InGaAs is several order of magnitude less than the thermal diffusion coefficient of silicon. This is a direct consequence of the smaller thermal conductivity of InGaAs (appendix A). It is interesting to note that the thermal diffusivity of silicon increases 2 orders of magnitude when temperature decreases from 300K to 50K, which helps to cool faster the tip. This is not the case for InGaAs, where thermal diffusivity increases also, but not significantly.

Material	Temperature (K)	Thermal diffusivity (cm^2/s)
Silicon	300	1.05
	100	22.3
	50	164
InGaAs	300	0.035
	100	0.058
	50	0.098

Table 5.1.1: Thermal diffusivity D of silicon and InGaAs at different temperature.

We approximate the cone as a cylinder in the next discussion. Estimation of the different time scales for heat diffusion and carrier diffusion along the tip axis and along the cross section of the tip are given in Table 5.1.2 for practical tip dimension at 300K and 100K. Considering the estimation of the cooling time along the tip length, for silicon, the estimation at 300K (237ns) is far too large compare to what is expected in the TOF (15-20 ns, from 3.1.1). This is even worst for InGaAs which is 2 orders of magnitude too large compare to the TOF estimation (10 ns from 3.2.1).

These estimation are in fact too naive, because the thermal properties depend on the temperature. For example, when temperature decreases form 300K to 100K, thermal diffusion increases significantly for silicon and the characteristic time scale decreases by one order of magnitude.

For InGaAs, the decrease in the characteristic time scale is, however, not significant when temperature decreases. Thus, there is a problem here, because the expected cooling time is 10 ns, but the estimated cooling time is 2 orders of magnitude greater than expected. There are different neglected effects that could explain the large estimated cooling time.

In the estimation in Table 5.1.2, we have assumed that the cooling process takes place all along the tip's length. If the cooling is significant only on a length scale smaller than the tip's length, for example 1 μm (five times smaller), the cooling time would be 25 times faster, which would make the cooling time for a silicon tip consistent with the TOF decay. For InGaAs, this would still not be enough (7.1μs/25$\sim$284ns). The increase in local cross section radius as we move away from the apex has been also neglected (we considered a cylinder in Table 5.1.2). Intuitively, an increase in the cross section would make the diffusion of heat faster because the thermal resistance would locally decrease.

L	Tip diameter(100nm)	Tip length (5μm)
$\tau_{carriers,Si}$	0.55ps	1.38ns
$\tau_{carriers,InGaAs}$	0.45ps	1.13ns
$\tau_{thermal,Si,300K}$	95ps	237ns
$\tau_{thermal,InGaAs,300K}$	2.8ns	7.1μs
$\tau_{thermal,Si,100K}$	4.47ps	11.1ns
$\tau_{thermal,InGaAs,100K}$	1.73ns	4.34μs

Table 5.1.2: Characteristic cooling time for silicon and InGaAs at different temperatures and for different characteristic lengths.

Comparing now the carrier and heat diffusion time scales, as seen in Table 5.1.2, at 300K, the carriers diffusion faster than thermal diffusion in silicon and InGaAs when temperature . When temperature decreases to 100K, however, thermal diffusion increases significantly for silicon and the characteristic time scale associated (11.1 ns) becomes on the order of the carrier diffusion. Thus at low temperature, the carrier and thermal diffusion have the same dynamics. Because for silicon carriers recombination release energy to the lattice through Auger recombination, carrier diffusion cannot be neglected, which justify the use of a couple model for silicon.

On the contrary, for InGaAs, the dynamics of thermal diffusion is always 3 order of magnitude slower than the carrier diffusion, whatever the temperature. Thus, carrier can be assumed to reach a uniform distribution inside the tip before heat diffuses. Because we consider radiative recombination where energy of the recombination is lost (uncoupling between carrier and heat diffusion), the spatial distribution of excess carrier and temperature can be computed separately.

5.1.4 1D-simplification

In order to simulate the temperature evolution of the tip, one has to solve the system of couple equations (5.3) and (5.1) for silicon and only equation (5.3) for InGaAs. Because solving the full 3 dimensional equation can be computationally expensive, we simplify the problem by considering only a 1D diffusion along the tip axis.

Physically, this 1D temperature evolution is consistent with the 3D temperature evolution along the tip axis if variations in the tip cross section doesn't affect the evolution along the tip axis. This is equivalent as considering an uniform temperature distribution in each cross section of the conical tip, which is justify here by the high aspect ratio of the tip. Heat diffuses much faster in the cross section (typical dimension around 100 nm) than along the tip as seen in Table 5.1.2. Note, however, that the heat diffusion in the cross section of the tip for InGaAs (a few nano-seconds) is on the order of the TOF slow decrease curve, which is not the case for the silicon tip. Thus, for InGaAs, the 1D assumption can be questioned.

In order to get a 1D version of the conical tip, we must evaluate the budget of the 3D heat equation on a infinitesimal control volume dV.

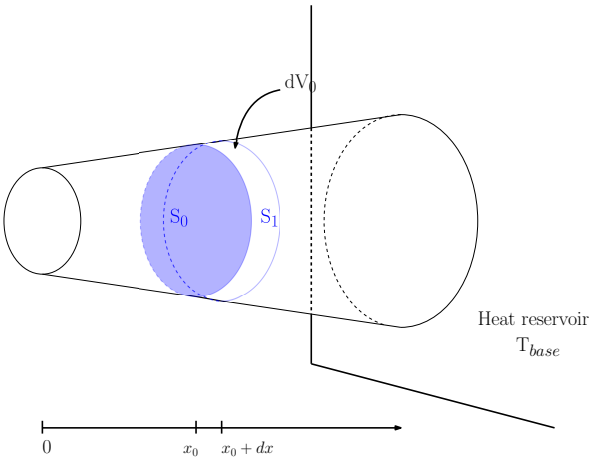

Figure 5.1: Representation of the volume of integration for the 1D heat equation on a conical tip.

Considering no convection (vacuum) and no radiation, the heat equation (5.3) integrated on the control volume dV_0 as shown in Figure 5.1 gives (see appendix C)

$$\left(\rho C_p R^2 \partial_t T\right) + \partial_x(-kR^2\partial_x T) = R^2 Q, \tag{5.8}$$

with $R = R(x)$ the local radius and $Q = E_{gap}R_{si,ingaas}$. The boundary conditions are $\partial_x T\Big|_{x=0} = 0$ (at the apex) and $T\Big|_{x=L} = T_{base}$ (at the base). Similarly for the ambipolar diffusion equations, equation (5.1) becomes,

$$\left(R^2\partial_t n\right) + \partial_x(-D_a R^2 \partial_x n) = -R^2 R_{si,ingaas}, \tag{5.9}$$

with $R_{si} = C_A n^3$ and $R_{ingaas} = 0$. The boundary conditions are $\partial_x n\Big|_{x=0} = 0$ (at the apex) and $\partial_x n\Big|_{x=L} = 0$ (at the base).

The initial carriers distribution is given by

$$n_{init}(x) = \frac{\frac{1}{S(x)}\int_{S(x)} u_{abs}(x,y,z)dS}{h\nu} = \frac{u_{abs,1D}(x)}{h\nu}. \tag{5.10}$$

where $S(x)$ is the cross sectional area at position x. The initial temperature distribution is given by

$$\int_{T_{base}}^{T_0} \rho C_p dT = n_{init}(x)(h\nu - E_{gap}). \tag{5.11}$$

5.1.5 Numerical resolution

In order to solve (5.8) and (5.9), a numerical solver, *GetDP*, is used. *GetDP* is a apen-source program for the numerical solution of integro-differential equations. It can be used also to solve coupled physical problems (electromagnetic, thermal, etc.) as well as of numerical methods (finite element method, integral methods, etc.). It can deal with such problems of various dimensions (1D, 2D or 3D) and time states (static, transient or harmonic). In this thesis, we use finite element to solve the equations. Because the problem is 1D, the domain is simply a line. The grid mesh is generated using *gmsh*[15], a free 3D finite element mesh generator.

When using *GetDP*, the user needs to write in ASCII data files the organization of the data defining the discrete problem and the symbolic mathematical expressions of the problem in the form of a weak formulation of the equations. The weak formulation of (5.8) and (5.9) can be easily work out as it is simply Diffusion equation. Since the thermal properties are temperature dependant and $R_{si} = C_A n^3$, a non linear algorithm must be used. In this thesis, we use the simple Picard's iteration to handle the non-linearity.

5.2 Temperature evolution

In this section, we analysis the temperature evolution of the apex using the 1D simplified model. Let us recall that we are interesting in the cooling time of the apex, as it is expected to directly influence the TOF spectra.

Let's first consider that all the incoming energy of the laser is used to heat the sample. It is the same as considering that there is no carrier excitation and all the energy form the photon is transferred to the electron already present in the conduction, which then thermalize and transfer their energy to the lattice. Thus, the initial temperature is given by

$$\int_{T_{base}}^{T_0(x)} \rho C_p dT = u_{abs,1D}(x). \tag{5.12}$$

This over-simplified model allows to focus the analysis only on the thermal diffusion, which, as we will see in the following part of the chapter, already gives important results.

5.2.1 Initial temperature profile

We consider first a tip with R_{apex}=50nm, $\alpha = 2°$ and L=4μm. Since no internal electric field for a tip with L=5μm could have be simulated with ADDA due to computational resources, we artificially consider that the portion of the tip not simulated is not heated, and is thus at the base temperature T_{base}. This assumption will be discussed. The laser pulse has a repetition rate of f_{rep} = 100kHz with a spot radius R_{spot} = 20μm and a pulse duration T_{pulse} = 500fs. The base temperature T_{base} = 20K.

The temperature profiles for a UV illumination with laser power P=1.2mW , green illumination with laser power P=1mW and IR illumination with laser power P=4mW are shown in Figure 5.2. Computation of $u_{abs,1D}(x)$ is based on the internal electric field of figure 4.4a, 4.4b and 4.4c respectively.

The temperature profiles at each wavelength in Figure 5.2 follows the distribution of electric field from 4.4a, 4.4b and 4.4c. For UV, since the electric field is located near the surface only (figure 4.4a), as x increases, the cross section $S(x)$ increases and the average absorbed energy per unit volume decreases. The situation is similar in green. For IR, the 2 maxima in Figure 4.4c are present in the initial temperature profile for IR.

Note that when looking at the maximal temperature value at each wavelength in Figure 5.2, the assumption that all the energy is used to heat the sample seems to give reasonable temperature profile considering that the usual measured temperature are around 300K. The periodic ripples visible in the temperature profile along x are due to 2 contributions from the DDA approximation and the integration eq. (5.10). Firstly, the DDA formulation leads to the creation of staircase sidewalls and make the cross section section $S(x)$ follows a discrete function ($S(x)$ is constant over the step, and increase by one dipole size at each step). Secondly, the staircase sidewalls (see 4.1.2) lead to high intensity of the electric field in their corner. Thus, these 2 contributions are reflected in $u_{abs,1D}(x)$. These ripples are, however, not significant as they localized.

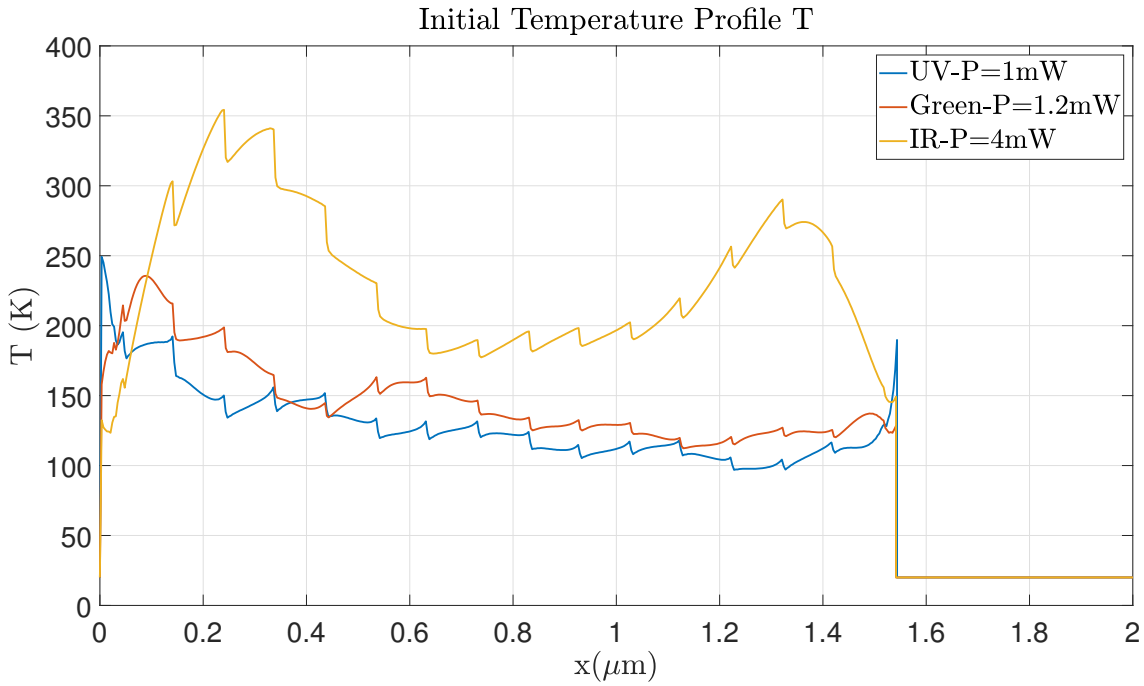

Figure 5.2: Initial temperature profile for a tip with R_{apex}=50nm, $\alpha = 2°$ and L=4μm at different laser illumination. The region $x > 1.5\mu$m is assumed to be non heated.

5.2.2 Impact of the wavelength

The temperature evolution at the apex for the different wavelength are shown in Figure 5.3. The results are also shown in Figure 5.4 in x-log scale to better see the temperature evolution. The first striking observation in Figure 5.4 is that the cooling process predicted by the model is on the order of few microseconds, as it was estimated in 5.1.3. This is an issue, as we are 2 to 3 orders of magnitude higher than what is expected in the TOF spectra figure 3.6.

The second observation is that the time for the tip to cool down to its base temperature depends on the laser illumination conditions. The model predicts that the cooling takes more time when using IR illumination with laser power P=4mW than green and UV illumination with laser power P=1mW and 1.2mW respectively. By looking at the initial temperature profile, the longer cooling time for IR is reasonable because the initial average temperature for IR was higher than UV and IR. However, the decrease in the TOF spectra is similar for each wavelength

(3.6). Thus, once again, the thermal model predicts a wavelength dependence that is not seen in the experimental data.

In Figure 5.4, we can see that the maximal temperature with IR illumination is reached later (around 10^{-8}s) than with green and UV illumination (around 10^{-9}s). This is a consequence of the initiale temperature profile figure 5.2. For IR, the profile present a maximum at $x \sim 0.3\mu$m from the apex ($x = 0\mu$m), which is not the case for green and UV. A quick estimation of the time required for the heat to travel a distance $L = 0.3\mu$s using eq. (5.6) gives $\tau \sim 2.5 \times 10^{-8}$s, which is in good agreement what is seen Figure 5.4.

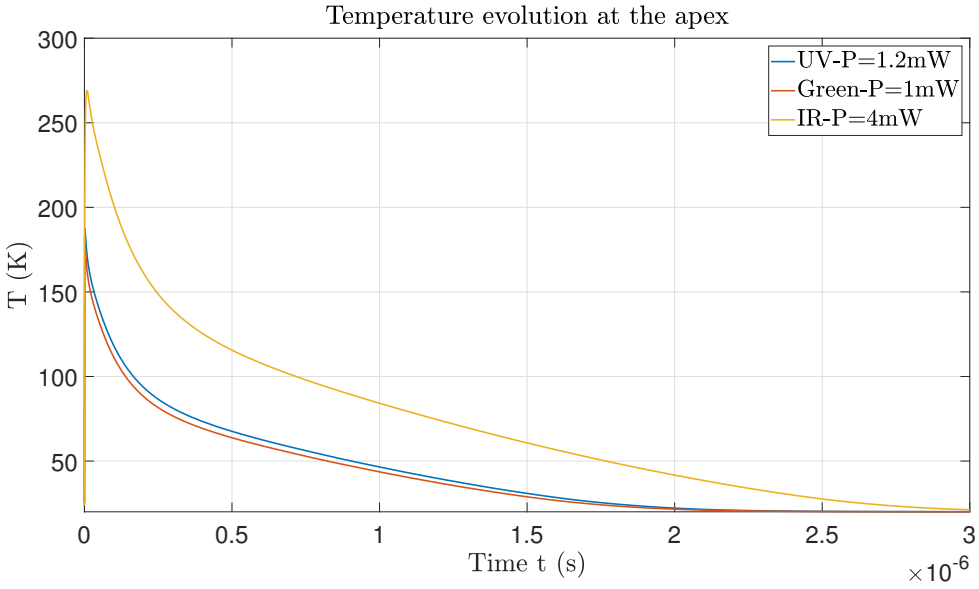

Figure 5.3: Temperature evolution of the tip's apex for a tip with R_{apex}=50nm, $\alpha = 2°$ and L=4μm at different laser illumination.

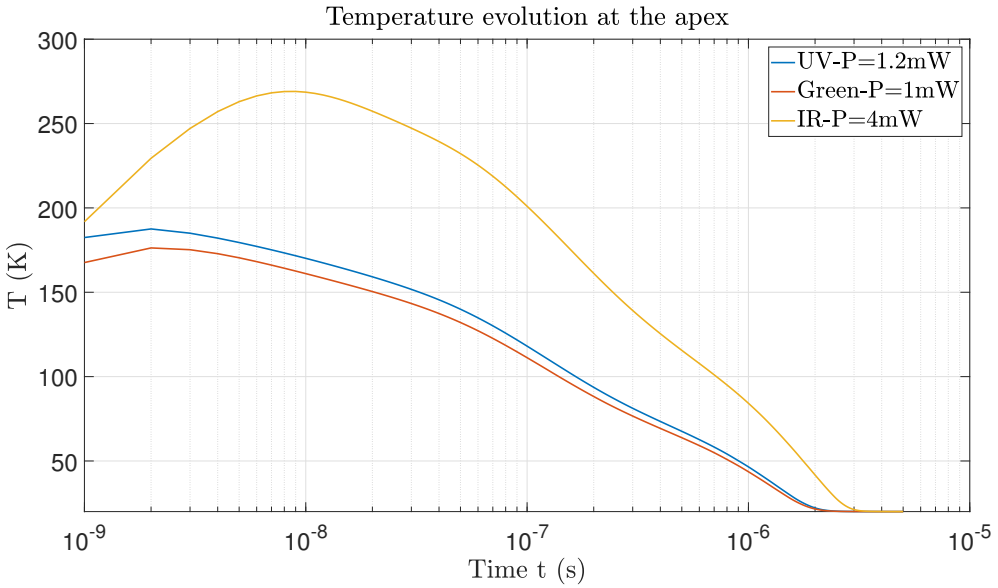

Figure 5.4: Temperature evolution of the tip's apex for a tip with R_{apex}=50nm, $\alpha = 2°$ and L=4μm at different laser illumination on a x-log scale.

5.2.3 Impact of Laser power

The temperature evolution at the apex for at different power with green illumination are shown in Figure 5.3. The results are also shown in Figure 5.4 in x-log scale to better see the temperature evolution.

As seen in Figure 5.5, when the power is decreased, the cooling process is similar between each cases. The total time required for the tip to cool down from its maximal temperature to its base temperature is slightly reduced when the power is decreased, about 2.5μs , 2μs and 1.5μs at laser power P=1mW, 0.6mW and 0.2mW respectively, which is related to the maximal temperature of the tip. More time is required to cool the tip at higher temperature.

From the previous observation, the thermal model indicates that the power should influence the TOF as it influences the cooling time. However, this is not the case as seen in Figure 3.7. What is more, the order of magnitude of the cooling process predicted by the thermal model is far too long, on the order of the microsecond. In order to explain this problem, we have to investigate what might influence the cooling time and verified the validity of the hypothesis.

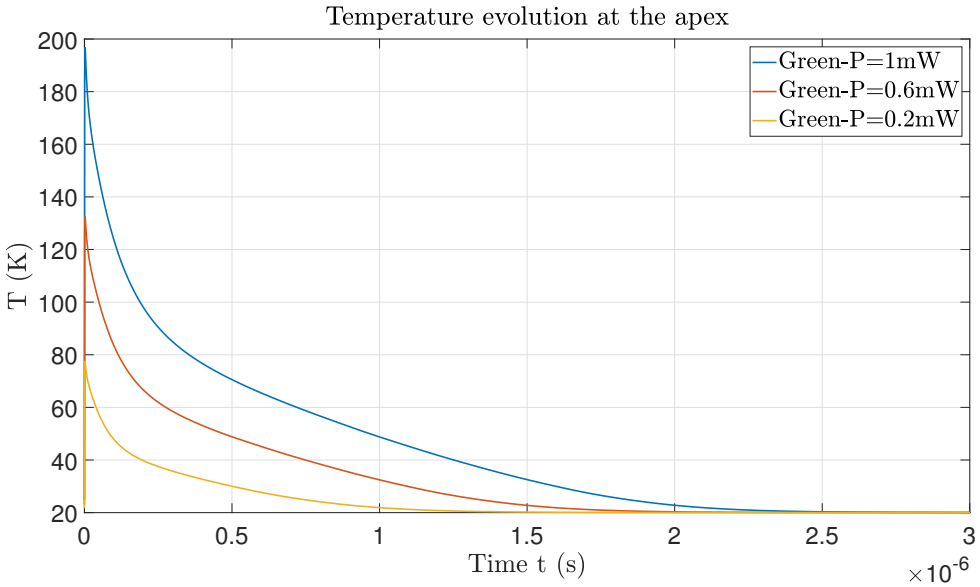

Figure 5.5: Initial temperature profile for a tip with R_{apex}=50nm, $\alpha = 2°$ and L=4μm under green illumination at different laser power.

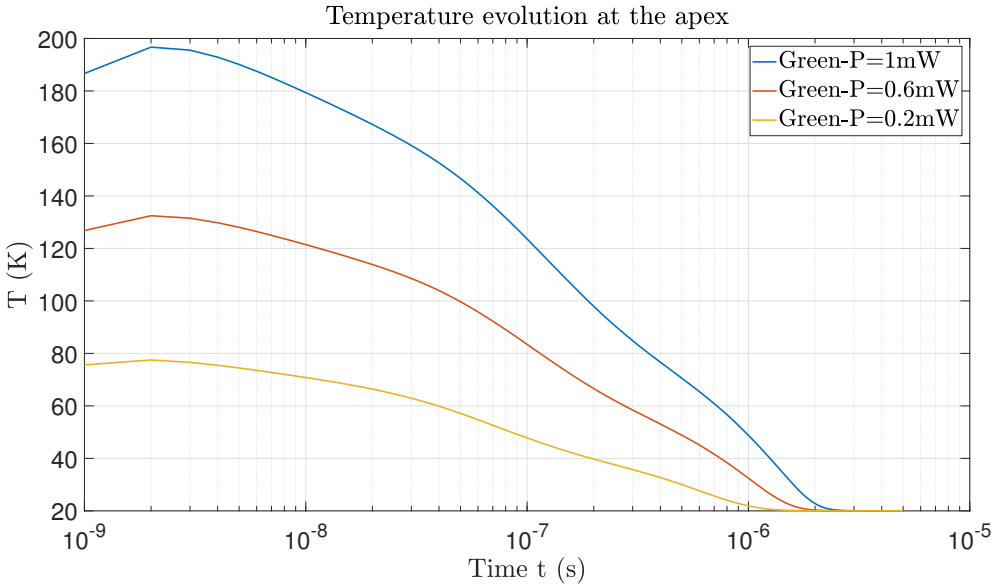

Figure 5.6: Temperature evolution of the tip's apex for a tip with R_{apex}=50nm, $\alpha = 2°$ and L=4μm under green illumination at different laser power.

5.2.4 Impact of the initial parameters

What we mean by the impact of the initial parameters are every parameters that have not been investigates, such as the shank angle, the apex radius, the tip length and the base temperature. We analyse the variation of these parameter for a tip under green illumination with laser power P=1mW.

Shank angle

The tip we considered has an apex radius R_{apex} = 50nm, length 4μm and $T_{base} = 20K$. The results for the temperature evolution of the apex for shank angle $\alpha = 2$, 4 and 8° are shown in Figure 5.7 and in x-log scale in Figure 5.8. Initial temperature profile based on Figure 4.9.

As it can be seen in Figure 5.7, the cooling is slightly faster when the shank angle increases. In fact, for higher shank angle, the cross section increases faster as x increases. When heat flows, the section it can crosses is then higher. Similarly to and electrical resistance, the local thermal resistance and more heat can flows, which cools down the tip faster. This effect is clearly visible when we consider the cooling of tip uniformly heating at 300K for different shank angle as shown in Figure 5.9.

Note that the average energy density decreases for higher shank angle since the local cross section is higher. Thus temperature is lower, which can favor faster cooling. However, in our case, this effect is not visible since the initial temperature profile are determined on tips quite short (figure 4.9) compare to the total length 4μm.

Although for higher shank angle, cooling is slightly faster, it cannot decrease the cooling time by 2 orders of magnitude.

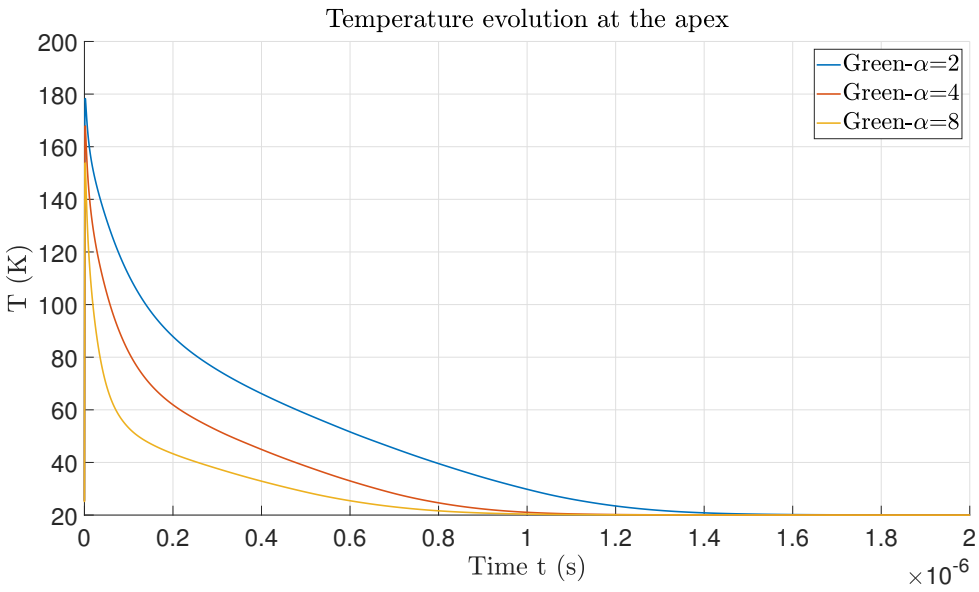

Figure 5.7: Temperature evolution of the tip's apex for a tip with R_{apex}=50nm, L=4μm under green illumination at P=1mW at different shank angle

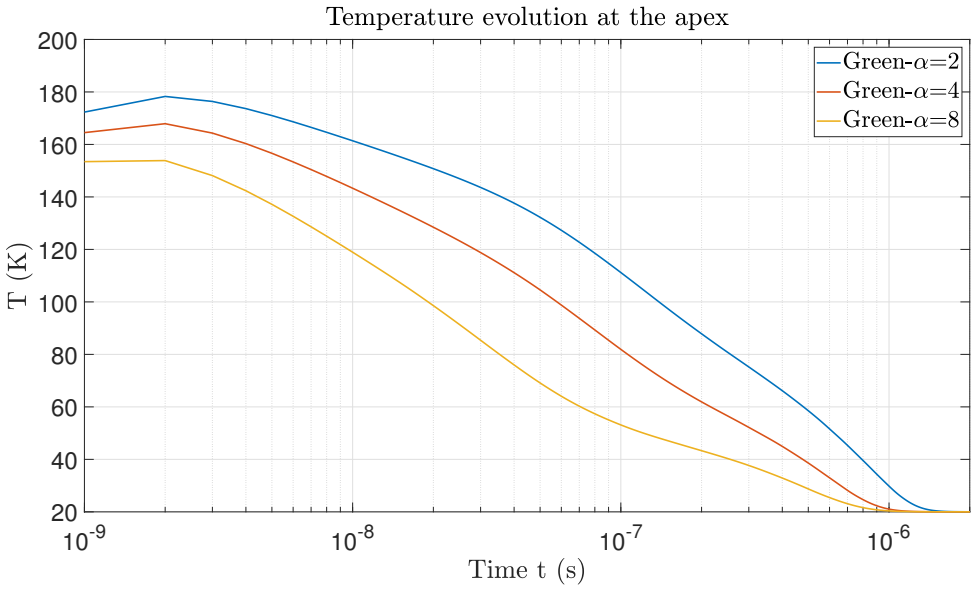

Figure 5.8: Temperature evolution of the tip's apex for a tip with R_{apex}=50nm, L=4μm under green illumination at P=1mW at different shank angle on a x-log scale.

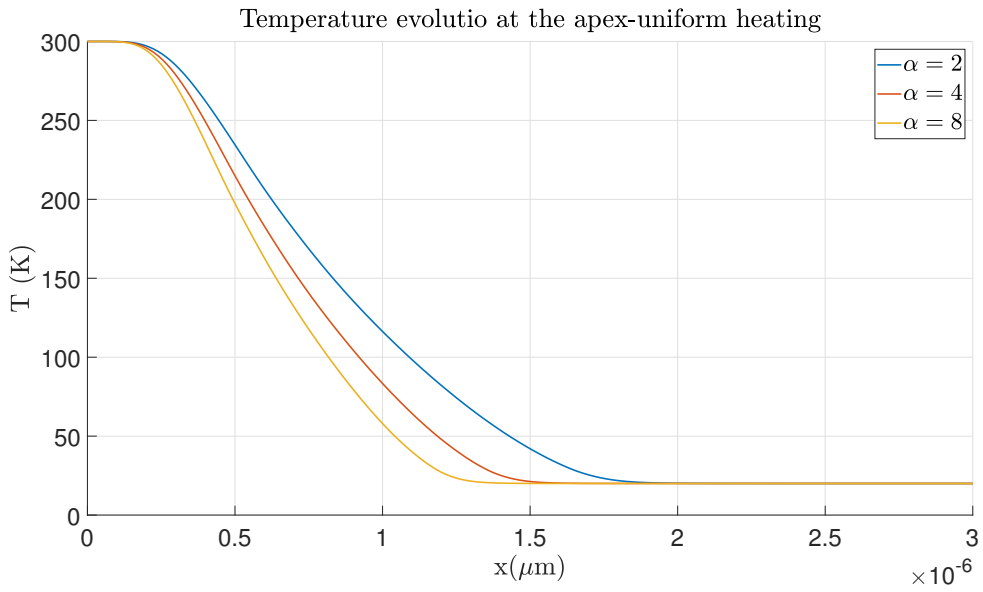

Figure 5.9: Temperature evolution of the tip's apex for a tip with R_{apex}=50nm, L=4μm at different shank angle. This tip is uniformly heated.

Tip length

The tip we considered has an apex radius $R_{apex} = 50$nm, shank angle $\alpha = 2°$ and $T_{base} = 20K$. The results for the temperature evolution of the apex for a length $L = 2$, 3 and 4μs are shown in Figure 5.7 and in x-log scale in Figure 5.11. Initial temperature profile based on Figure 4.9.

As it can be seen in Figure 5.10, the cooling process is faster when the length is decreased, which is consistent with eq. 5.6. When decreasing the length by a factor of 2, the characteristic cooling time is decreased by a factor of 4, which is the case in Figure 5.10 when going from L=4μm (τ_c ~1.5μs) to L=2μm (τ_c ~0.4μs). However, the cooling time is still far too large, even when the length decreases. To get a cooling time on the order of a few nanosecond as in the TOF spectra, the tips length should be ten times smaller than 4μm, which is not the case.

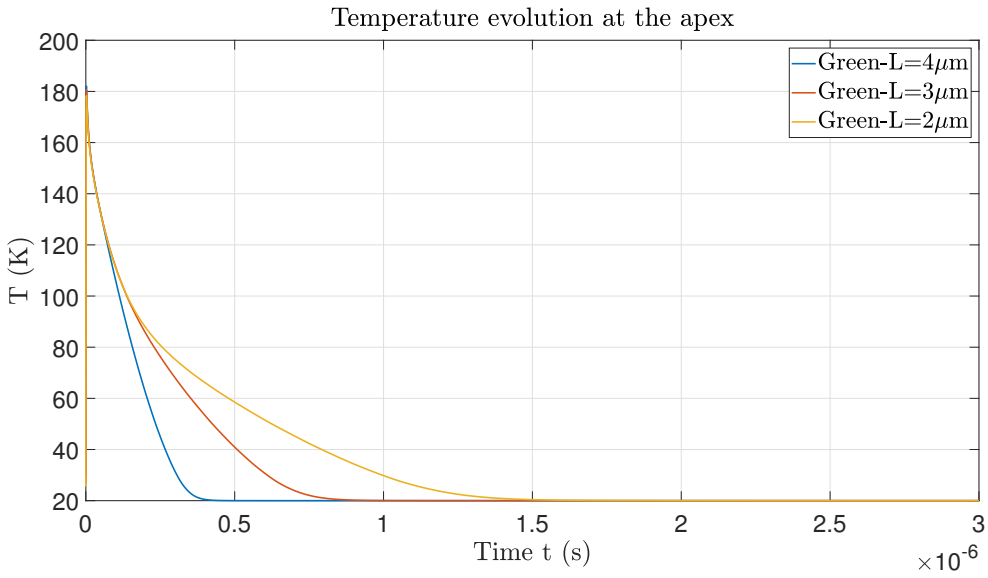

Figure 5.10: Temperature evolution of the tip's apex for a tip with R_{apex}=50nm, α=2° under green illumination at P=1mW at different tip length L.

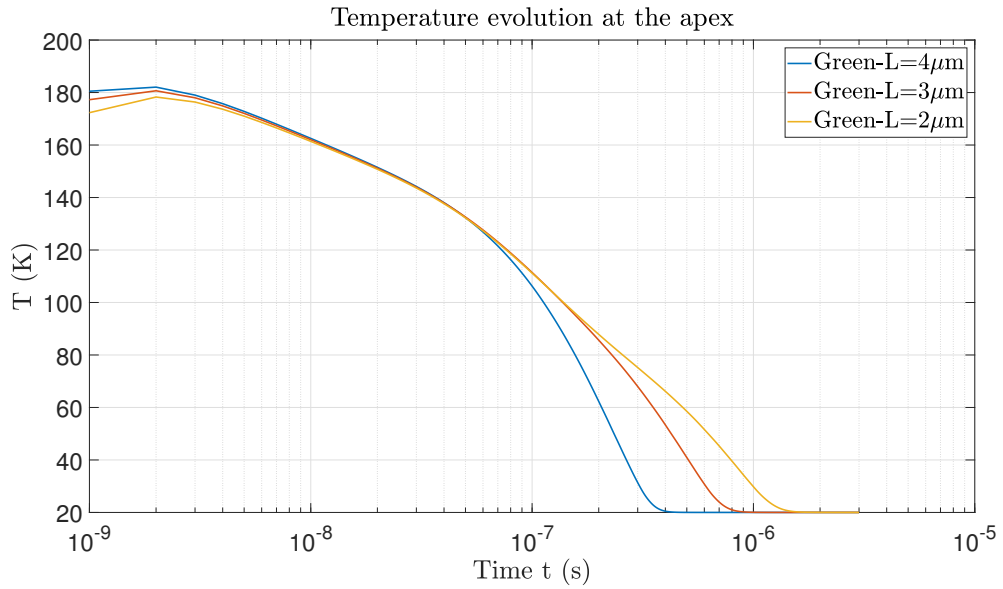

Figure 5.11: Temperature evolution of the tip's apex for a tip with R_{apex}=50nm, α=2° under green illumination at P=1mW at different tip length L on a x-log scale.

Base temperature

The tip we considered has an apex radius R_{apex} = 50nm, shank angle α = 2° and length L=4μm. The results for the temperature evolution of the apex for a base temperature T_{base} = 20, 40 and 60K are shown in Figure 5.12. Initial temperature profile based on Figure 4.9. Note that the initial temperature profile is modified since we compute the integral in eq. 5.12 from T_{base} to $T_0(x)$.

As it can be seen in Figure 5.12, the cooling is slower when the base temperature is increased (3μs at T_{base} = 60K, 2.5μs at T_{base} = 40K and 1.5μs at T_{base} = 20K). This is a consequence of the increase of the thermal diffusivity at low temperature as seen in Figure A.6, which helps to cool down faster when the temperature of the apex drop below 50K.

However, the increase in thermal diffusivity is not significant enough when the temperature of the base decreases to have a cooling time on the order of few nanosecond.

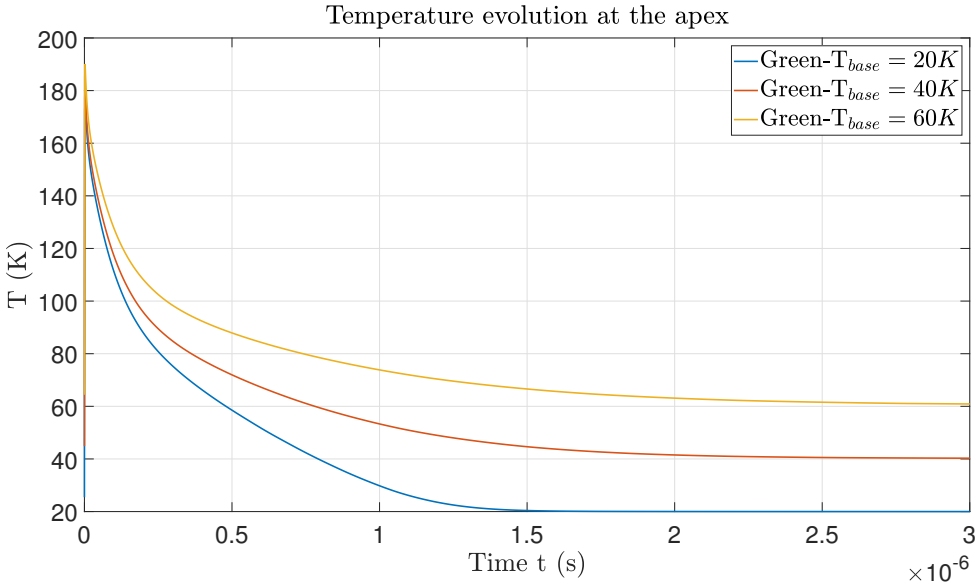

Figure 5.12: Temperature evolution of the tip's apex for a tip with R$_{apex}$=50nm, L=4μm $\alpha = 2°$ at different base temperature T_{base}.

5.3 Validity of the simplified model

From the previous observations on the parameters of the problem, it can be concluded that the simple thermal model is not able to explain the TOF spectra in Figure 3.6. Concerning the cooling time, even when combining all the effects to decrease it, a cooling time on the order of a few nanosecond cant be recover with this simple model. The reason for this problem is mainly due to a poor conductivity of the InGaAs.

In the model used in the previous section, we have made several assumptions in order to evaluate the temperature.

5.3.1 Initial temperature profile

To determine the initial temperature profile, we have made 2 assumptions. First, we have supposed that all the absorbed was used to heat the sample in equation (5.12). If we consider IR illumination with laser power P=22mW used in Figure 3.6, the resulting initial temperature profile shown in Figure 5.13 indicates that the maximal temperature is 1500K, above the melting temperature (see A.2.2), which is unexpected. However, this can be explained as a possible overestimation of the absorbed energy.

First, when we compute the absorbed energy, we have to calculate first the intrinsic electric field of the pulse laser (see Appendix B). The value of the intrinsic electric field is dependant on several parameter such as the sport size R_{spot}, the repetition rate f_{pulse}, the average laser power P_{avg} and the pulse duration T_{pulse} (eq. (B.5)). Uncertainty in the value of this parameters is present [23]. For example, if the spot size is 40μm rather than 20μm, the intensity of the laser is smaller (the effective area has increased by a factor of 4, power per unit area thus decreases) and so the absorbed energy is also smaller (eq. B.11). In this example, by reducing increase the spot size, the initial temperature is then lower as seen in Figure 5.13.

Second that can reduce the initial temperature is the carrier excitation. If we don't neglect the carriers excitation in (5.11), photon energy is absorbed and excites carriers, which only return part of the energy to the lattice through thermalization. Thus the initial temperature is smaller. However, since we now considered the carrier into the problem, we need to look in more details about the dynamics of carrier diffusion/recombination since recombination might return energy to the lattice. This is discussed in the next section of this chapter.

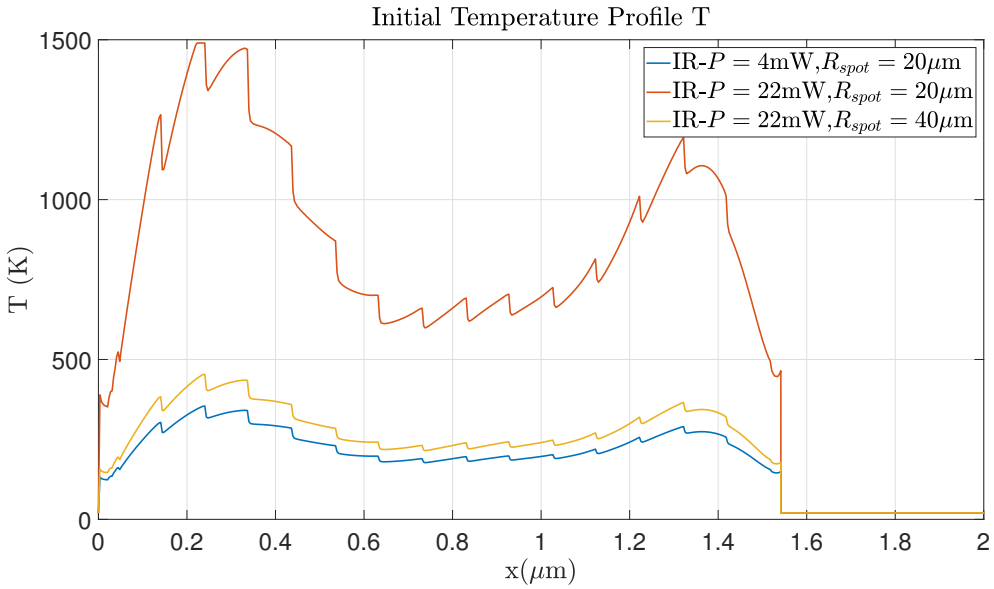

Figure 5.13: Initial temperature profile for IR illumination with different laser power conditions. $R_{apex} = 50$nm,$L = 4\mu$m and $\alpha = 2°$.

Another assumption that has been made in the initial temperature profile is the addition of a section of the tip that is not heated where no data are available from the ADDA simulation (due to computational ressources). We then drastically underestimate the real initial temperature profile. However, if we can have the real initial temperature profile, instead of the non heated region, we would have a heated region with a given initial temperature profile. The cooling time would then be larger, since thermal diffusion would first need to diffuse the "extra" heat. Thus, the apex would start to cool down later than the case where we neglect this heated region. Note that if it is not possible to have the internal electric field numerically, as it has been shown in chapter 4, the Mie solution can be used instead.

Even though changes in the initial temperature profile are possible due to uncertainties in the input parameters or due to a neglected contribution (carrier), the cooling will still be on the order of a few μs.

5.3.2 Carriers diffusion/recombination

If we consider the carriers, we must first compute the initial carriers distribution using eq. (5.10). The initial profile for $n_{init}(x)$ for the tip from 5.2.1 under green illumination is shown in Figure 5.14. As it can be seen, the carrier concentration is on the order of 10^{20}cm^{-3}. This number is extremely high considering the actual doping level ($\sim 10^{16}$cm^{-3}) and the density of states in the conduction band 2×10^{17}cm^{-3} (at 300K, see appendix A). Thus the physical meaning fullness of the estimation of the number of excess carrier is thus questionable.

Let us now discuss what influence the carriers can have on the temperature profile. For InGaAs, at at doping level of 10^{16}cm^{-3}, we have shown that radiative recombination was the

main recombination mechanism and that energy from the recombination was lost. Thus, in this model when considering the carriers , their effect is to reduce the maximal initial temperature. However, a smaller temperature cannot lead to a decrease in the cooling time of 2 orders of magnitude.

If we now considered the computed carrier concentration $n_{init}(x)$ (10^{20}cm^{-3}) realistic, we need to take into account Auger recombination and radiative recombination. To evaluate the recombination rate, we can look at the carrier lifetime inside the semiconductor

$$\tau = [Bn + C_A n^2]^{-1}, \tag{5.13}$$

where B ($1.43\times10^{-10}\text{cm}^{-3}\text{s}^{-1}$)is the radiative recombination coefficient and C_A ($7.5\times10^{-29}\text{cm}^6/\text{s}$) the Auger recombination coefficient.

At an excess carrier concentration of 10^{16}cm^{-3}, the carrier lifetime due to radiative recombination is $\tau_r \sim 1/(Bn) \sim 10^{-6}$s and $\tau_A \sim 1/(C_A n^2) \sim 10^{-4}$s for Auger recombination. As expected for a excess carrier concentration of 10^{16}cm^{-3}, radiative recombination dominate. For an excess carrier of 10^{20}cm^{-3}, $\tau_r \sim 1/(Bn) \sim 10^{-10}$s and $\tau_A \sim 1/(C_A n^2) \sim 10^{-10}$s and the 2 processes are dominant. Thus, energy from the recombination might be return to the lattice through Auger recombination at this excess carrier concentration.

However, the carrier lifetime or equivalently the recombination rate is on the order of 10^{-10}s. This occurs on a time scale much shorter than heat diffusion. Note also that the diffusivity coefficient of the carrier in InGaAs leads to characteristic diffusive times always 2 orders of magnitude smaller than characteristic cooling times as seen in Table 5.1.2.

The situation for an excess carrier concentration of 10^{20}cm^{-3} is then as follow : Carriers diffuse and recombine at time scales much shorter than the characteristic time of heat diffusion. Since carriers recombine one order of magnitude faster than they diffuse, energy from the recombination is returned to the lattice almost at the place where energy has initially been absorbed by the excess carriers. Consequently, even if we consider heat source term from the recombination, the dynamics of the carrier has only an effect of redistributing the energy, before heat diffusion starts. This cannot in any case help the cooling process to decrease by 2 orders of magnitude.

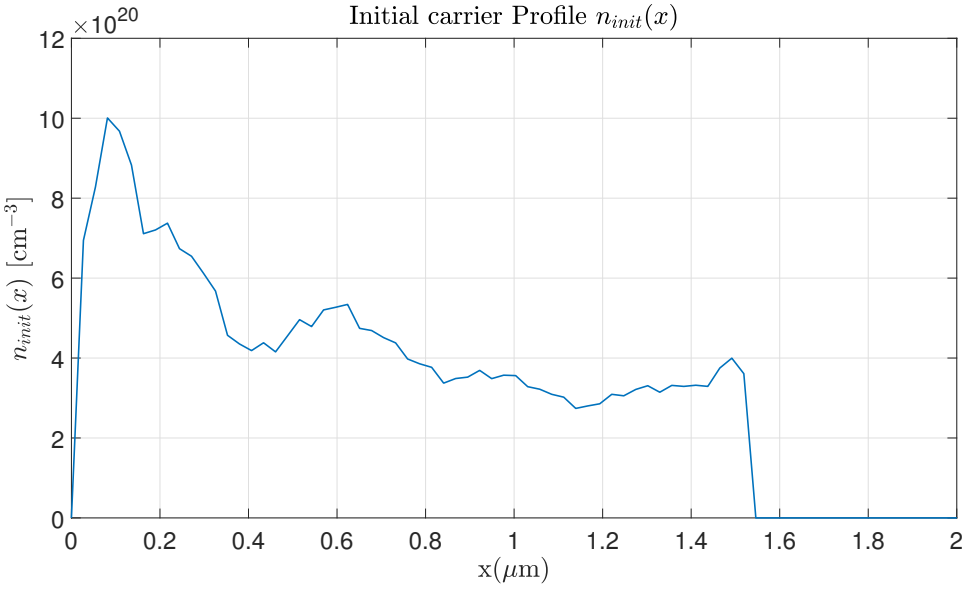

Figure 5.14: Initial carriers distribution for a tip with $R_{apex} = 50\text{nm}$,$L = 4\mu\text{m}$ and $\alpha = 2°$ under green illumination with laser power $P = 1\text{mW}$.

5.3.3 1D-hypothesis

Another hypothesis made is that the temperature evolution of the tip can be described using a 1D model. The 1D approximation is obtained by assuming that each cross section is a the same temperature, which is justified by the the smaller diffusion time in the cross section compare to the diffusion time along the tip axis as shown in table 5.1.2. Thus the model supposes that the temperature first gets uniform in each cross and then diffuses along the tip axis.

No 3D neither 2D thermal model have been tested to justify the validity of the 1D approximation. A 3D or even a 2D model could be useful to get information on the local variation of temperature on the surface of the apex. However, it is not expected that the cooling of the apex would be impacted by 2 orders of magnitude when using a 3D thermal model.

5.4 Conclusion

In this chapter, we have analysed and described the temperature evolution of the tip apex using a 1D simplified thermal model. We first described the model commonly used for silicon tips. In this model, the temperature evolution is described by a heat equation coupled to an ambipolar equation for the carriers, where recombination transfer their energy to the lattice. By analyzing the orders of magnitude, the characteristic cooling time of the apex for an InGaAs tip is found to be 2 orders of magnitude higher than expected from the TOF spectra (a few nanoseconds).

We then looked at the temperature evolution neglecting the contribution of the carriers. Using this simple model, it is not possible to recover the good order of magnitude. What causes the cooling to be on the order of a few microseconds is the low thermal conductivity of InGaAs. What is more, the cooling time is influenced by the parameters (laser power, wavelength, shank angle, tip length) of the problem, which is not seen in the TOF spectra.

Thus, in order to verified the validity of the models, we have reviewed the hypothesis made. Even though uncertainties are possible on the initial temperature distribution, the cooling time is still 2 orders of magnitude too large. The cooling process is still too slow even if we consider the carrier diffusion/recombination into the problem. In this chapter, we then face a problem: the simple thermal problem used for silicon tips doesn't predict the expected results for InGaAs tips.

Chapter 6

Conclusion

In this thesis, we have investigated the interaction between a femto-second pulse laser and nano-scale conical tips made of InGaAs under UV, green and IR illumination. The aim of this work was to give a better understanding on the interaction between the laser and InGaAS tips and on the cooling process of the apex of these InGaAs tips. It would then allow to better interpret the experimental results obtained with the laser assisted atom probe machine. Because of the recent use of this type of material in the transistor industry, few works have been done on Laser assisted atom probe.

As discussed in chapter 1, the down-scaling of the transistors imposes to replace silicon with new materials with higher electron mobility, such as InGaAs, a ternary alloy of indium arsenide (InAs) and gallium arsenide (GaAs) from the III-V semiconductors family. Parallelly the planar transistors are being progressively replaced by a 3D fin geometry (FinFET), and an information on the internal structure is important to ensure performance and reliability of the device. The laser atom probe tomography is an atomic-resolution microscopy technique based on the emission of ionized species from a needle shaped specimen by a process called field evaporation (Field evaporation is the field-induced removal of a surface atom) which can provide a 3D image of the position of the atom with almost atomic spatial resolution (∼0.2-0.3nm) and their chemical species.

In Chapter 3, the comparison between experimental results for silicon tips from the literature to the recent experimental results for InGaAs tip at *Imec* has been made. The time of flight spectra of silicon presented long tails after as sharp peak (slow decreasing in the number of counts) which were dependent on the wavelength used. As it has been explained in chapter 2, the field evaporation process can be described as a thermally activated process (Arrhenius law). This thermal dependence explains the difference in mass resolution observed between each wavelength for silicon. By using a coupled thermal-carrier diffusion model and the absorption energy maps at the different wavelength, the temperature evolution correlates quite well with the tails.

For InGaAs tips, the TOF spectra also presented long tails after a sharp peak, but no dependence on the wavelength used. The TOF spectra did also not depends on the power of the laser, which was not case for silicon. Concerning the hit maps, for silicon and InGaAs, a one-sided effect was visible.

First, in order to explain the hit maps of InGaAs and understand how light interacts with nano-scale elongated InGaAs tips, we analyse in chapter 4 the internal electric field inside the tips. We have used a numerical tool to simulate light scattering of 3D volume, ADDA. The

results showed that UV the electric field is entirely located near the surface. Thus, this could explain the one-sided effect seen on the hit maps with UV illumination. For IR, the electric field is mostly located inside the volume of the tip. For green, the situation is intermediate, depending on the radius size.

By using fundamental principles of light interference and coupling inside nano-scale volume, we have been able to explain qualitatively and quantitatively the numerical simulation. This study on the distribution of the internal electric field gives more understanding on where energy will be mostly absorbed and provides important information for the interpretation of the hit maps.

Then, we investigate the temperature evolution of the apex. To do so, we have first explained the coupled thermal diffusion and carrier diffusion/recombination models proposed for silicon and simplified it to only focused on the thermal diffusion. However, the simplified thermal model fails to give the correct orders of magnitude for the cooling time. The reason for this large cooling time is found in the poor conductivity of InGaAs. What is more, the model predicts a dependence of the cooling time on the power and on the wavelength used, in contradiction with the experimental data.

Several assumptions made in the model have been questioned, such as the influence of the carriers in the cooling process. However, their evolution cannot make the cooling time change by 2 orders of magnitude. The main issue is the poor thermal conductivity of InGaAs. It is simply not possible to obtain a decrease on the order of a few nano-seconds with the conductivity of InGaAs. Since only few data on the thermal properties of InGaAs can be found in the literature, more precise values could remove some uncertainties at low and high temperature.

In the thermal model used here, we have considered a continuum approach. For example, we consider that the thermal conductivity at the nano-scale of the tip used is the same as the bulk thermal conductivity. This hypothesis can be questioned. Indeed, in the case of nano-wire, it is often seen that thermal conductivity decreases when diameter decreases to nano-scale, results of a higher scattering of the phonons [32][31]. This would suggest that the diffusion of heat would be even slower. However, this shows that a more advanced model for the heat diffusion could potentially give different results than the simplified thermal model used here.

Appendix A

Properties of InGaAs and Si

In this appendix we present the properties of silicon (Si) and $Ga_{47}In_{53}As$.

A.1 Optical properties

A.1.1 Refractive Index

The value for the refractive index as a function of the wavelength for silicon [10] and InGaAs [22] are shown in Figure A.1 and Figure A.2 for the real and imaginary part respectively.

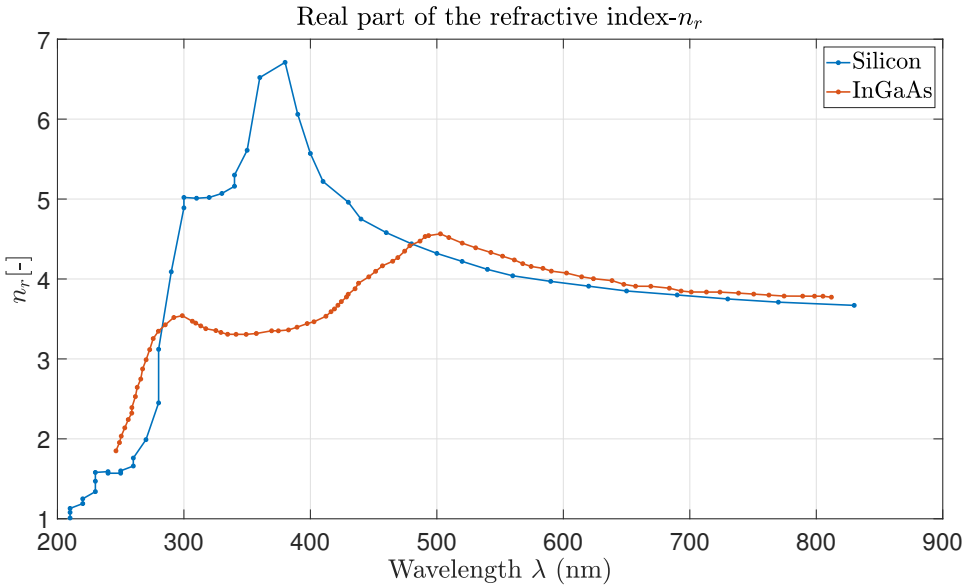

Figure A.1: Real part of the refractive index of silicon and InGaAs.

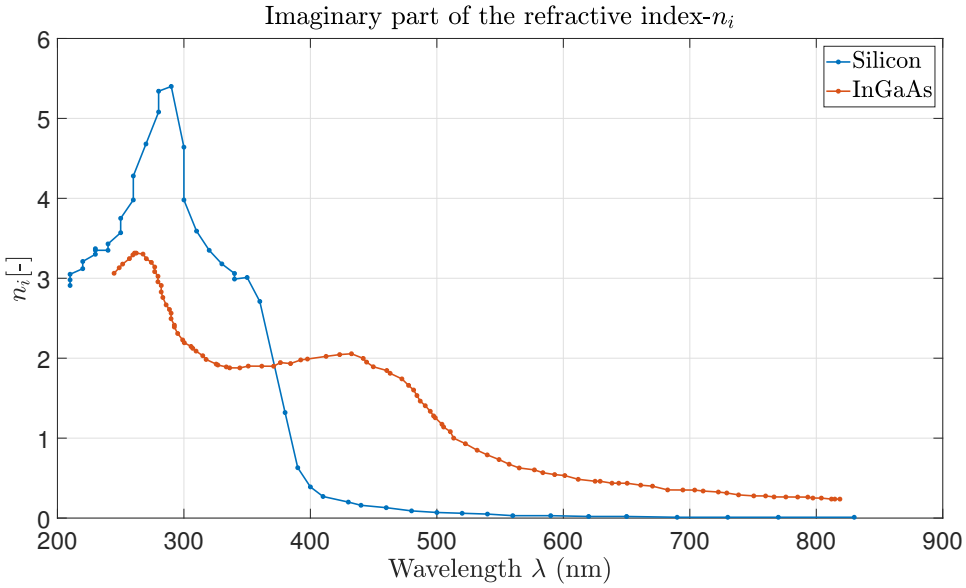

Figure A.2: Imaginary part of the refractive index of silicon and InGaAs.

The refractive index at the three wavelengths used in this thesis, infrared (IR) (1030 nm— 1.2 eV), green (515 nm — 2.4 eV) and ultraviolet (UV) (343 nm — 3.6 eV) for silicon [23] and InGaAs [22] are presented in Table A.1.1.

	UV(343nm)	Green(515nm)	IR(1030nm)
Si	5.275 +3i	4.215+0.039i	3.6+0.001i
InGaAs	3.3+1.92i	4.5+0.95i	3.65+0.26i

Table A.1.1: Complex refractive Index $\widetilde{n} = n_r + in_i$ for silicon and InGaAs at 3 different wavelength.

The relation between the the complex refractive index and the relative complex relative permittivity is

$$(n_r + in_i)^2 = (\varepsilon' + i\varepsilon'') = \varepsilon_r, \tag{A.1}$$

where we can derive

$$\varepsilon'_r = n_r^2 - n_i^2, \tag{A.2}$$
$$\varepsilon''_r = 2n_r n_i. \tag{A.3}$$

Note that $\varepsilon = \varepsilon_0 \varepsilon_r$.

A.1.2 Penetration depth

For an electromagnetic wave passes through a medium, the intensity of the wave will be attenuated. This is usually represented with a complex refractive index $\widetilde{n} = n_r + \mathrm{i}n_i$ (n_i is the extension coefficient). We can write for a plane wave propagating inside a medium of complex refractive index $\widetilde{n}$

$$\mathbf{E}(z,t) = \mathrm{Re}\left[\mathbf{E}_o e^{i(\widetilde{k}z-\omega t)}\right] = \mathrm{Re}\left[\mathbf{E}_o e^{i(2\pi\widetilde{n}/\lambda_0 z-\omega t)}\right] = e^{-2\pi n_i z/\lambda_0}\mathrm{Re}\left[\mathbf{E}_o e^{i(kz-\omega t)}\right]. \tag{A.4}$$

The intensity is proportional to the square of the electric field, which gives

$$\mathrm{I} = |\mathbf{E}|^2 \propto e^{-4\pi n_i z/\lambda_0} = e^{-z/\delta} \tag{A.5}$$

and the penetration depth is the distance after which the intensity is reduced by 1/e,

$$\delta_p = \frac{\lambda_0}{4\pi n_i}. \tag{A.6}$$

The penetration depth at the three wavelengths used in this thesis, infrared (IR) (1030 nm— 1.2 eV), green (515 nm — 2.4 eV) and ultraviolet (UV) (343 nm — 3.6 eV) for silicon and InGaAs are presented in Table A.1.2 based on the value of table A.1.1.

	UV(343nm)	Green(515nm)	IR(1030nm)
Si	82e3	1.05e3	9.1
InGaAs	315.2	43.1	14.2

Table A.1.2: Penetration depth (nm) for wave incident on a infinite volume of silicon or InGaAs for 3 different wavelengths.

A.2 Thermal properties

A.2.1 Specific heat capacity

The specific heat for silicon [30] and InGaAs [1] are shown in Figure A.3. A zoom at the heat capacity for small temperature is shown in Figure A.4. Note that no data were found for the specific heat of InGaAs after 285K. Thus, for simplicity, a constant heat capacity is assumed.

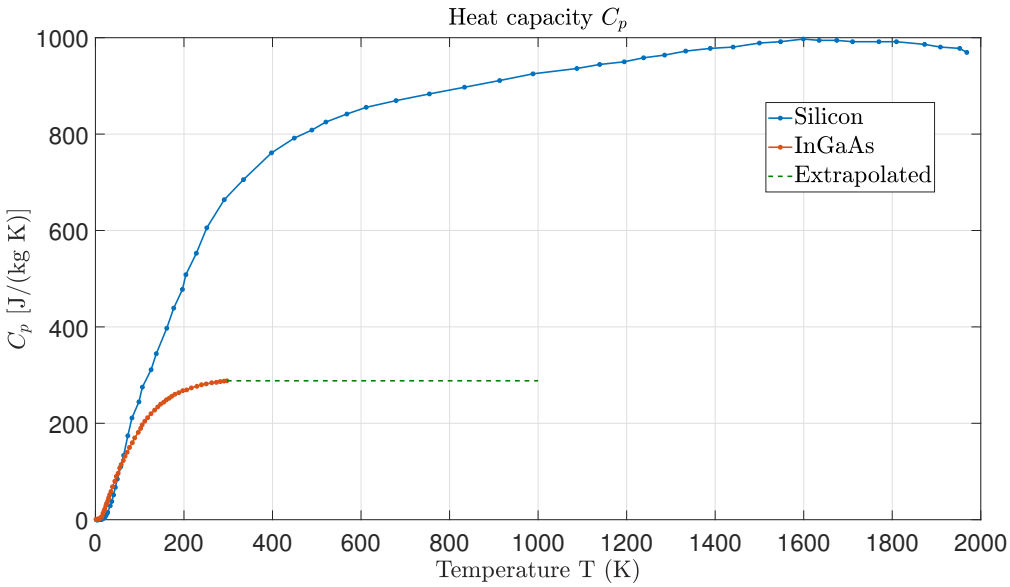

Figure A.3: Heat capacity as a function of the temperature for silicon and InGaAs.

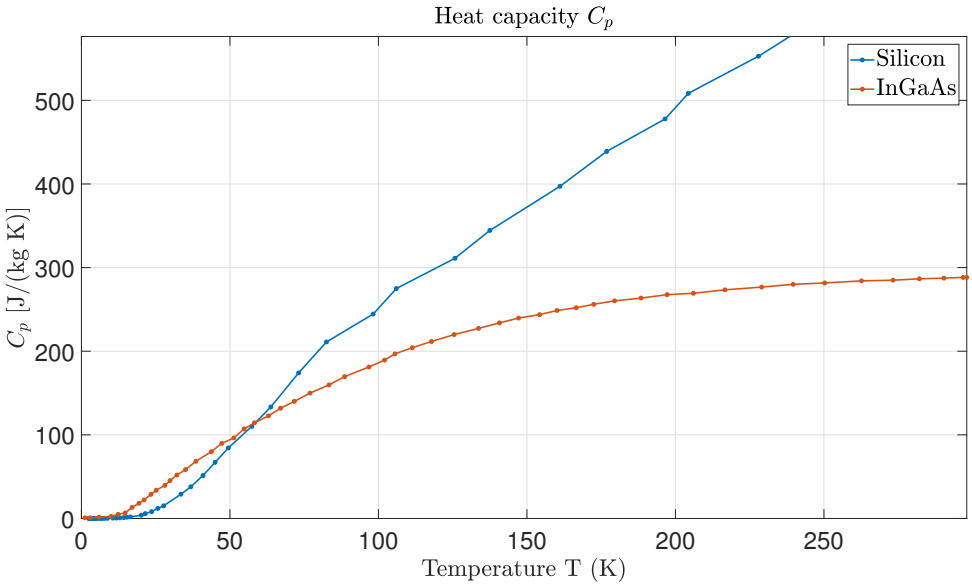

Figure A.4: Heat capacity as a function of cryogenic temperature for silicon and InGaAs.

A.2.2 Thermal conductivity

The thermal conductivity for silicon [30] and InGaAs [44] are shown in Figure A.5.

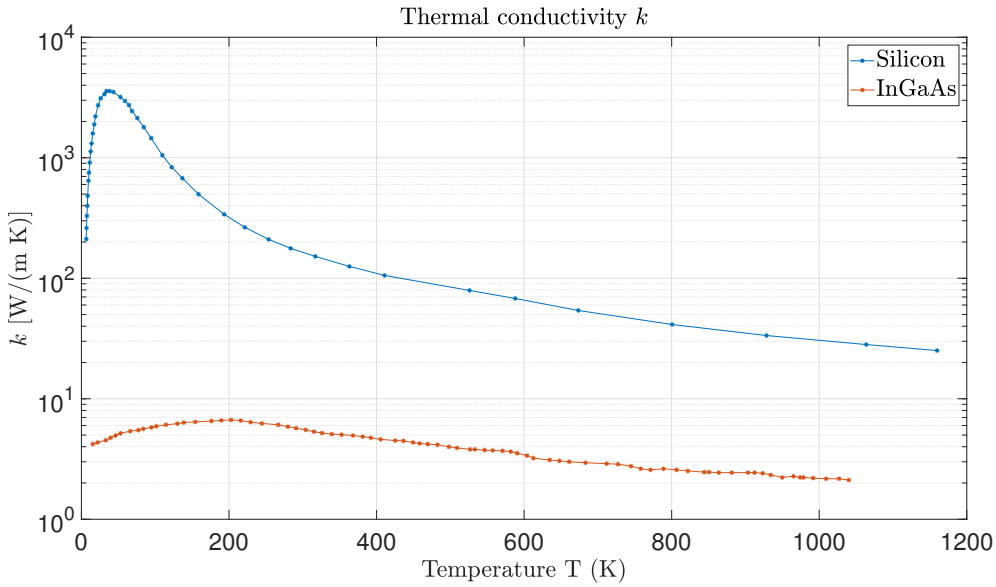

Figure A.5: Thermal conductivity as a function of the temperature for silicon and InGaAs.

A.2.3 Density

The density of silicon [30] and InGaAs [1] at 300K are given in Table A.2.1. Since no data are currently available for the density of InGaAs as a function of temperature, it is assumed constant, which is a good assumption as density of solid varies only weakly as temperature changes.

	Si	InGaAs
ρ	2.329e3	5.50e3

Table A.2.1: Density (kg /cm^3)of silicon and InGaAs at 300K.

A.2.4 Thermal diffusivity

Ther thermal diffusivity is defined as

$$D = \frac{k}{\rho C_p}. \tag{A.7}$$

The thermal diffusivity of InGaAs as a function of the temperature is shown in Figure A.6

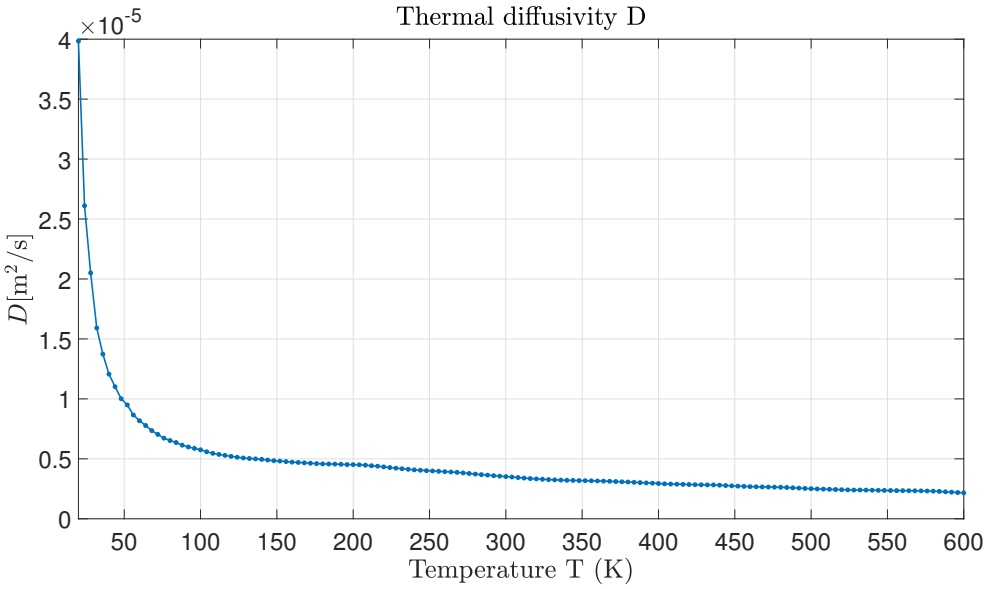

Figure A.6: Thermal diffusivity as a function of the temperature for InGaAs.

A.2.5 Melting point

The melting temperature for silicon and InGaAs [1] are given in Table A.2.2.

	Si	InGaAs
T_{melt}	1687	1373

Table A.2.2: Melting temperature(K) of silicon and InGaAs.

A.3 Electronic properties

A.3.1 Silicon

The band structure of silicon in the k-space [30] is shown in Figure A.7.

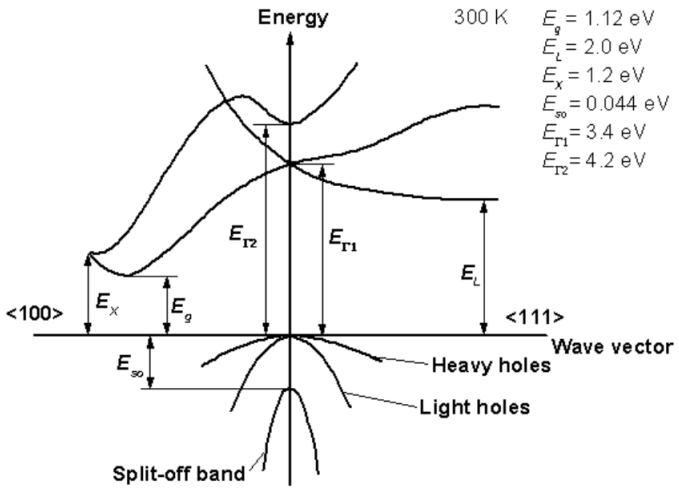

Figure A.7: Silicon band structure. Reproduced from [30].

The temperature dependence of the indirect band gap energy in eV of silicon [30] is

$$E_g = 1.17 - 4.73 \times 10^{-4} T^2/(T + 636). \tag{A.8}$$

A.3.2 InGaAs

The band structure of InGaAs in the k-space [1] is shown in Figure A.8.

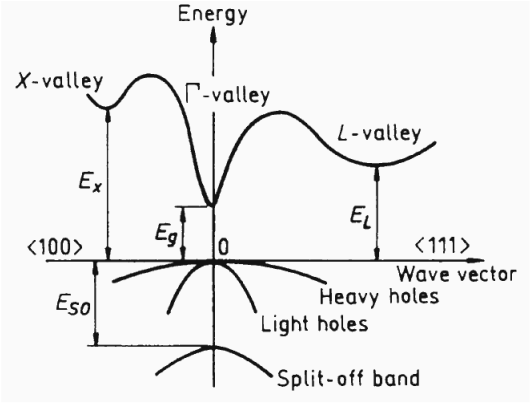

Figure A.8: InGaAs band structure. Reproduced from [1].

The temperature dependence of direct band gap energy in eV of $In_{1-x}Ga_xAs$ [1] is

$$E_g = 0.42{+}0.625x{-}(5.8/(300{+}T){-}4.19/(271{+}T)){\times}10^{-4}{\times}T^2x{-}4.19{\times}10^{-4}{\times}T^2/(T{+}271){+}0.475x^2. \tag{A.9}$$

For $x = 0.47$ at T=300K $E_g = 0.742$eV, which will be assumed constant in this thesis (we neglect the influence of the temperature). The temperature dependence of the effective density of states in the conduction band N_c in cm^{-3} at $x = 0.47$ is

$$N_c = 4.82 \times 10^{15} \times 0.0083 T^{3/2}, \tag{A.10}$$

which is equal to $2.08{\times}10^{17}$ cm^{-3} at 300K.

Appendix B

Laser pulses

In this appendix we make the link between and incident pulse laser and the energy deposit in a material.

B.1 Intensity of laser pulses

From the average laser power P_{avg}, we can calculate the pulse energy E_p expressed in Joule/pulse as

$$E_p = \frac{P_{avg}}{f_{rep}}, \tag{B.1}$$

where f_{rep} is the repetition rate of the laser. If we consider the laser spot to be circular in space, the energy per unit surface for one pulse, express in Joule/m^2 is

$$D = \frac{E_p}{\pi R_{spot}^2} = \frac{P_{avg}}{\pi R_{spot}^2 f_{rep}}, \tag{B.2}$$

where R_{spot} is the spot radius.

The average optical intensity I can be evaluated if we assume the shape of the pulse to be rectangular in time, which gives

$$\mathrm{I} = \frac{D}{T_{pulse}} = \frac{P_{avg}}{\pi R_{spot}^2 f_{rep} T_{pulse}}, \tag{B.3}$$

where T_{pulse} is the pulse duration.

B.2 Beam intrinsic electric field

We can also make the link between the intrinsic electric field of the laser and the intensity I per pulse. This is important to know the value of the electric field since the distribution maps computed by ADDA in chapter 4 are for a unitary beam electric field.

Using the Pointing vector definition $\hat{\mathbf{P}} = \mathbf{E} \times \mathbf{H}$ and the average intensity I of the beam

I= $\frac{1}{2}\hat{\mathbf{P}} \cdot \frac{\mathbf{k}}{\|\mathbf{k}\|}$ with $\mathbf{k}$ the vector along the beam propagation direction, one can compute

$$\begin{aligned} \mathrm{I} &= \frac{1}{2}\hat{\mathbf{P}} \cdot \frac{\mathbf{k}}{\|\mathbf{k}\|} \\ &= \frac{1}{2}\left(\mathbf{E} \times \mathbf{H}\right) \cdot \frac{\mathbf{k}}{\|\mathbf{k}\|} \\ &\text{Since } \mathbf{E} \text{ and } \mathbf{H} \text{ are both normal to the propagation direction, we get} \\ &= \frac{1}{2} E\ H = \frac{E^2}{2\sqrt{\mu/\varepsilon}} \\ &= \frac{n_r \varepsilon_0 c_0}{2} \|\mathbf{E}\|^2, \end{aligned} \tag{B.4}$$

where n_r is the refractive index of the medium ($\sim$ vacuum), ε_0 is the permittivity of free space and c_0 the speed of light in vacuum.

From B.4 and B.3, we deduce the amplitude intrinsic electric field of the pulse

$$|E| = \sqrt{\frac{2I}{n_r \varepsilon_0 c_0}} = \sqrt{\frac{2P_{avg}}{n_r \varepsilon_0 c_0 \pi R_{spot}^2 f_{rep} T_{pulse}}}. \tag{B.5}$$

In this thesis, we choose $R_{spot} = 20\mu$m, a pulse duration is $T_{pulse} = 500$fs and a repetition rate $f_{rep} = 100$kHz [2]. Values for the electric field at typical laser power are provided in Table B.2.1 for $n = 1$ (vacuum).

Laser Power	0.2mW	1mW	22mW
Optical intensity	0.32 GW/cm^2	1.6GW/cm^2	35GW/cm^2
Electric field	48V/μm	10V/nm	51V/μm

Table B.2.1: Optical intensity and electric field magnitude at typical laser power for $R_{spot} = 20\mu$n,$T_{pulse} = 500$fs and $f_{rep} = 100$kHz.

B.3 Absorbed energy

In this section we derive the relation between the absorbed power $\mathscr{P}$ density and the electric field of for the case of a monochromatic plane wave of angular frequency ω. This can be derived based on the Poynting's theorem [41]. The average absorbed power over one period, using phasor formalism, is given by

$$\mathscr{P} = \frac{1}{2}\mathrm{Re}\left\{\nabla \cdot \left(\hat{E} \times \hat{H}^*\right)\right\} = \frac{1}{2}\mathrm{Re}\left\{\hat{H}^* \cdot \nabla \times \hat{E} - \hat{E} \cdot \nabla \times \hat{H}^*\right\}, \tag{B.6}$$

where $\hat{A}$ denotes the phasor of the corresponding quantity A and A^* denotes the complex conjugate of A. We also have the following relations

$$\nabla \times \hat{E} = -i\omega\hat{B} = \frac{-i\omega}{\mu_0}\hat{H}, \tag{B.7}$$

$$\nabla \times \hat{H} = \hat{J} + i\omega(\varepsilon' + i\varepsilon'')\hat{E}, \tag{B.8}$$

and

$$\hat{J} = \sigma\hat{E}, \tag{B.9}$$

where $\mathbf{J}$ is the current density, σ the conductivity of the material and $(\varepsilon' + i\varepsilon'')$ its complex permittivity. We can define the effective complex permittivity $i\omega\widetilde{\varepsilon} = \sigma + i\omega(\varepsilon' + i\varepsilon'')$ to write

(B.8) in a more compact form. Using the previous equations and (A.3) and $\omega = 2\pi c/\lambda$, (B.6) becomes

$$\begin{aligned}
\mathscr{P} &= \frac{1}{2}\mathrm{Re}\left\{\hat{H}^*\left(-i\frac{\omega}{\mu_0}\right)\hat{H} - \hat{E}\left(i\omega\widetilde{\varepsilon}\hat{E}^*\right)\right\} \\
&= \frac{1}{2}\omega\mathrm{Im}\{\widetilde{\varepsilon}\}\left\|\hat{E}\right\|^2 \\
&= \frac{1}{2}\omega\varepsilon''\left\|\hat{E}\right\|^2 = \frac{1}{2}\omega\varepsilon_r''\varepsilon_0\left\|\hat{E}\right\|^2 \\
&= \frac{1}{2}\omega 2n_r n_i\varepsilon_0\left\|\hat{E}\right\|^2 = \frac{1}{2}4\pi\frac{c_o}{\lambda_0}n_r n_i\varepsilon_0\left\|\hat{E}\right\|^2 \\
&= \frac{1}{2}\delta_p c_0 n_r\varepsilon_0\left\|\hat{E}\right\|^2 \\
&= \delta_p I.
\end{aligned} \tag{B.10}$$

By integrating the average absorbed power density $\mathscr{P}$ over the pulse duration, we get the absorbed energy per unit volume. Because $\mathscr{P}$ is an average quantity, we get

$$u_{abs} = \mathscr{P} \times T_{pulse} = \delta_p I \times T_{pulse}, \tag{B.11}$$

where I can be computed from eq. (B.4), which in turn is known from the distribution of internal electric field computed in chapter 4.

Appendix C

Mathematical Complement

In this Appendix, we provide some complementary information on mathematical development

C.1 1D Heat approximation

The 3D heat diffusion equation on a conical tip can be integrated to get a 1D heat equation. We consider the heat equation

$$\rho C_p \partial_t T + \nabla \cdot (-k \nabla T) = Q, \tag{C.1}$$

where ρ is the density, C_p the heat capacity , k the thermal conductivity and Q a heat source term.

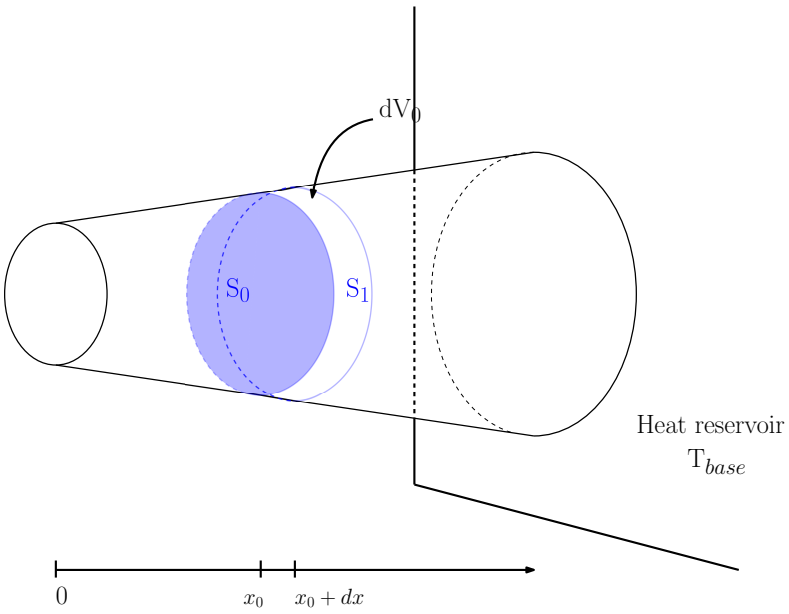

Figure C.1: Representation of the volume of integration for the 1D heat equation on a conical tip.

Equation C.1 is then integrated over the volume dV_0 as represented in Figure C.1, which

gives

$$\int_{\mathrm{dV}_0} \rho C_p \partial_t T \mathrm{dV} + \int_{\mathrm{dV}_0} \nabla \cdot (-k \nabla T) \mathrm{dV} = \int_{dV_0} Q \mathrm{dV}$$
$$\Longleftrightarrow$$
$$\int_{\mathrm{dV}_0} \rho C_p \partial_t T \mathrm{dV} + \sum_i \int_{\mathrm{S}_i} (-k \nabla T) \cdot \mathbf{n} \mathrm{dS} = \int_{dV_0} Q \mathrm{dV}$$
$$\Longleftrightarrow$$
$$\int_{\mathrm{dV}_0} \rho C_p \partial_t T \mathrm{dV} + \int_{\mathrm{S}_0} (-k \nabla T) \cdot (-\mathbf{ex}) \mathrm{dS} + \int_{\mathrm{S}_1} (-k \nabla T) \cdot (\mathbf{ex}) \mathrm{dS} = \int_{dV_0} Q \mathrm{dV}, \tag{C.2}$$

where dS=πR^2 ,dV= $\pi R^2 dx$ and $(\nabla) \cdot \mathbf{ex} = \partial_x$. Taking $\Delta x \to 0$ and considering each quantity depends only on x (uniform on the cross section), volume integral becomes

$$\int A \mathrm{dS} dx = \int_{x_0}^{x_0+\Delta x} \widetilde{A} dx \simeq \left(\widetilde{A}\Big|_{x_0} + \Delta x \frac{d\widetilde{A}}{dx}\Big|_{x_0} \right) (x_0 + \Delta x - x_0) \simeq \widetilde{A}\Big|_{x_0} \Delta x = \pi \left(A R^2 \right) \Big|_{x_0} \Delta x, \tag{C.3}$$

and surface integral becomes

$$\int_{S_i} B \mathrm{dS} = B\Big|_{x_i} S_i = \pi \left(B R^2 \right) \Big|_{x_i}. \tag{C.4}$$

Thus, (C.2) becomes

$$\pi \left(\rho C_p \partial_t T R^2 \right) \Big|_{x_0} \Delta x + \pi \left(-k \partial_x T R^2 \right) \Big|_{x_0+\Delta x} - \pi \left(-k \partial_x T R^2 \right) \Big|_{x_0} = \pi \left(Q R^2 \right) \Big|_{x_0} \Delta x, \tag{C.5}$$
$$\pi \left(\rho C_p \partial_t T R^2 \right) \Big|_{x_0} \Delta x + \pi \partial_x (-k \partial_x R^2) \Big|_{x_0} \Delta x = \pi \left(Q R^2 \right) \Big|_{x_0} \Delta x, \tag{C.6}$$
$$\rho C_p \partial_t T R^2 + \partial_x (-k \partial_x R^2) = Q R^2. \tag{C.7}$$

.

Bibliography

[1] . Electronic archive new semiconductor materials. characteristics and properties. `http://www.ioffe.ru/SVA/NSM/Semicond/index.html`. Accessed: 2018-08-15.

[2] . Imec. Private talk with Janusz Bogdanowicz.

[3] . Indium. `https://fr.wikipedia.org/wiki/Indium`. Accessed: 2018-08-15.

[4] . Silicium. `https://fr.wikipedia.org/wiki/Silicium`. Accessed: 2018-08-15.

[5] B. Gault A. Menand A. Vella, F. Vurpillot and B. Deconihout. Evidence of field evaporation assisted by nonlinear optical rectification induced by ultrafast laser. *PHYSICAL REVIEW*, 73:165416, 2005.

[6] J. Houard E. Silaeva L. Arnoldi I. Blum 1 L. Rigutti E. Pertreux P. Maioli A. Crut A. Vella, D. Shinde and N. Del Fatti. Optothermal response of a single silicon nanotip. *PHYSICAL REVIEW*, 97, 2018.

[7] Stegun IA AbramowitzM. *Handbook of mathematical functions*. Courier Dover Publications, 1965.

[8] Govind P. Agrawal. Optical waveguides (opt568), 2008.

[9] A. Vella H. Bernas B. Deconihoutai AM. Gilbert, F. Vurpillot. Some aspects of the silicon behaviour under femtosecond pulsed laser field evaporation. *Elsevier*, 107:767–772, 2007.

[10] D. E. Aspnes and A. A. Studna. Dielectric functions and optical parameters of si, ge, gap, gaas, gasb, inp, inas, and insb from 1.5 to 6.0 ev. *PHYSICAL REVIEW*, 27:985–1009, 1983.

[11] A. Vella M. Gilbert A. Menand D. Blavette B. Gault, F. Vurpillot and B. Deconihout. Design of a femtosecond laser assisted tomographic atom probe. *REVIEW OF SCIENTIFIC INSTRUMENTS*, 77:043705, 2006.

[12] Moody Julie M. Cairney Simon P. Ringer Baptiste Gault, Michael P. *Atom Probe Microscopy*. Springer, 2012.

[13] Hill SC Barber PW. *Light scattering by particles*. Word Scientific, 1990.

[14] A. Cerezoa and G. D. W. Smith. Measurement of temperature rises in the femtosecond laser pulsed three- dimensional atom probe. *APPLIED PHYSICS LETTERS*, 88:154103, 2006.

[15] Jean-Francois Remacle Christophe Geuzaine. Gmsh: a three-dimensional finite element mesh generator with built-in pre- and post-processing facilities. *INTERNATIONAL JOURNAL FOR NUMERICAL METHODS IN ENGINEERING*, 0:1–24, 2009.

[16] Jesús A. del Alamo. Nanometre-scale electronics with iii–v compound semiconductors. *NATURE*, 479:317–323, 2011.

[17] D.E. Perea K. Inoue D.J. Larson, T.J. Prosa and D. Mangelinck. Atom probe tomography of nanoscale electronic materials. *MRS BULLETIN*, 41:30–34, 2016.

[18] Fabian DORTU. Low frequency modulated optical reflectance for the one-dimensional characterization of ultra shallow junctions. Master's thesis, Katholieke Universiteit Leuven in cooperation with IMEC, 2009. `https://core.ac.uk/download/pdf/34436050.pdf`.

[19] A. Hideur G. Martel E. P. Silaeva, J. Houard and A. Vella. Field evaporation of semiconductors assisted by nonequilibrium phonon excitations. *PHYSICAL REVIEW*, 92:195307, 2015.

[20] Yasumitsu Suzuki Elena P. Silaeva, Kazuki Uchida and Kazuyuki Watanabe. Energetics and dynamics of laser-assisted field evaporation: Time-dependent density functional theory simulations. *PHYSICAL REVIEW*, 92:155401, 2015.

[21] ROBERT GOMER. Field desorption. *THE JOURNAL OF CHEMICAL PHYSICS*, 31:341–345, 1959.

[22] R. L&h H. Nickel H.W . Dinges, H. Burkhard and W . Schlapp. Refractive indices of inalas and ingaas/inp from 250 to 1900nm determined by spectroscopic ellipsometry. *Applied Surface Science*, 54:477–481, 1992.

[23] Nicolas Innocenti. Interaction of femtosecond laser pulses with nanoscale si-tips for atom probe tomography. Master's thesis, University of Liège, 2010.

[24] N. Innocenti S. Koelling B. Vanderheyden J. Bogdanowicz, M. Gilbert and W. Vandervorst. Light absorption in conical silicon particles. *OPTICS EXPRESS*, 3:3891, 2013.

[25] S. Koelling W. Vandervorst J. Bogdanowicz, M. Gilbert and W. Vandervorst. Impact of the apex of an elongated dielectric tip upon its light absorption properties. *Applied Surface Scienc*, 302:223–225, 2014.

[26] W. Vandervorst J. Bogdanowicz. On the understanding of local optical resonance in elongated dielectric particles. *Journal of Quantitative Spectroscopy & Radiative Transfer*, 146:175–180, 2014.

[27] F. Vurpillot J. Houard, A. Vella and B. Deconihout. Optical near-field absorption at a metal tip far from plasmonic resonance. *PHYSICAL REVIEW*, 81:1254115, 2010.

[28] F. Michael Kahner. Numerical methods in electromagnetic scattering theory. *Journal of Qauntitative & Radiative Transfer*, 79-80:775–824, 2002.

[29] G. L. Kellogg and T. T. Tsong. Pulsed laser atom probe field ion microscopy. *Journal of applied science*, 51:1184–1193, 1979.

[30] M Shur M Levinshtein, S Rumyantsev. *Semicondctors parameters*. World scientific, 2000.

[31] D S Oliveira A Cavalli I Zardo R W van der Heijden M Y Swinkels, M R van Delft and E P A M Bakkers. Diameter dependence of the thermal conductivity of inas nanowires. *Nanotechnology*, 26:385401, 2015.

[32] Martin Maldovan. Thermal conductivity of semiconductor nanowires from micro to nano length scales. *Journal of Applied Physics*, 11:024311, 2012.

[33] ERIN W. MULLER. Field desorption. *Physical Review*, 102:618–624, 1955.

[34] Edward M. Purcell and Carlton R. Pennypacker. Scattering and absorption of light by nonspherical dielectric grains. *The Astrophysical Journal*, 186:705–714, 1973.

[35] S. Johnston R. K. Ahrenkiel, R. Ellingson and M. Wanlas. Recombination lifetime of in0.53ga0.47as as a function of doping density. *APPLIED PHYSICS LETTERS VOLUME*, 72:3470, 1998.

[36] A. Schulze M. Gilbert A. K. Kambham S. Koelling, N. Innocenti and W. Vandervorst. In-situ observation of non-hemispherical tip shape formation during laser-assisted atom probe tomography. *JOURNAL OF APPLIED PHYSICS*, 109:104909, 2011.

[37] K.K. Law D. B. Young A. C. Gossard L. A. Coldren S. Y. Hu, S. W. Corzine and J. L. Merz. Lateral carrier diffusion and surface recombination in ingaas/algaas quantum well ridgewaveguide lasers. *Journal of Applied Physics*, 76:4479, 1994.

[38] P. J. Smith & D. A. Smith. Preliminary calculations of the electric field and the stress on a field-ion specimen. *Philosophical Magazine*, 21:907–912, 1970.

[39] S. K. SUNDARAM and E. MAZUR2. Inducing and probing non-thermal transitions in semiconductors using femtosecond laser pulses. *nature materials*, 1:217–224, 2002.

[40] Joseph H. Bunton Jonathan Houard Elena P. Silaeva Janusz Bogdanowicz Wilfried Vandervorst Thomas F. Kelly, Angela Vella. Laser pulsing of field evaporation in atom probe tomography. *Current Opinion in Solid State and Materials Science*, pages 1–9, 2013.

[41] B. Vanderheyden. Electromagnetism,cours, institut montefiore (elen0076), 20015.

[42] A. Vella. On the interaction of an ultra-fast laser with a nanometric tip by laser assisted atom probe tomography: A review. *Ultramicroscopy*, pages 1–14, 2013.

[43] R. J. Ellingson R. K. Ahrenkiel W. K. Metzger, M. W. Wanlass and J. J. Carapella. Auger recombination in low-band-gap n-type ingaas. *APPLIED PHYSICS LETTERS*, 79:1–4, 2001.

[44] Arthur Gossard Dmitri Klenov Susanne Stemmer Ali Shakouri Woochul Kim, Joshua Zide and Arun Majumdar. Thermal conductivity reduction and thermoelectric figure of merit increase by embedding nanoparticles in crystalline semiconductors. *PHYSICAL REVIEW*, 96:045901, 2006.

[45] M.A. Yurkin and A.G. Hoekstra. User manual for the discrete dipole approximation code ADDA 1.3b4. `https://github.com/adda-team/adda/blob/master/doc/manual.pdf`.

[46] M.A. Yurkin and A.G. Hoekstra. The discrete dipole approximation: an overview and recent developments. *Journal of Quantitative Spectroscopy & Radiative Transfer*, 106:558–589, 2007.